UNIVERSITY OF CALIFORNIA SAN DIEGO

Phonon Excitation in Cubic Crystal Targets via Dark Matter Scattering

A dissertation submitted in partial satisfaction of the
requirements for the degree Doctor of Philosophy

in

Physics

by

Brian Christopher Campbell-Deem

Committee in charge:

Professor Tongyan Lin, Chair
Professor Julio Barreiro
Professor Ertugrul Cubukcu
Professor Daniel Green
Professor Aneesh Manohar

2022

The Dissertation of Brian Christopher Campbell-Deem is approved, and it is acceptable in quality and form for publication on microfilm and electronically.

University of California San Diego

2022

DEDICATION

To every single one of my friends, family members, mentors, and colleagues who helped me get to where I am today, even if it was just by doing nothing else other than being there.

EPIGRAPH

Are you feeling nervous?

Are you having fun?

It's almost over

It's just begun

Robert Burnham

TABLE OF CONTENTS

LIST OF FIGURES

LIST OF TABLES

ACKNOWLEDGEMENTS

Anyone who has had more than a 20 second conversation with me during the past five years is already well aware that my PhD has been the most difficult thing I've ever had to face up until now. Worse than simply just pertaining to areas of physics which didn't come easily to me at all, I was engaged in a constant war with the mental onslaught grad school assaults you with. It struck at me incessantly, and percolated into how I felt about my intelligence, my capability, my goals, my identity, and my purpose. To top it all off, of course, nearly half of my degree happened during and after the COVID-19 pandemic and lockdown; as you can imagine, the isolation and air of despair seeped into essentially every facet of my life. There were many, many times when I thought of leaving. I often entertained ideas like withdrawing with my master's to pursue teaching, a feeling of purpose which was able to somehow weather the storm and persist through the ebbs and flows. Feeling trapped in a timeless, weatherless San Diego, the days blurred and I really never knew when it would all come to an end—and then suddenly, the conclusion to the story seemed to come all at once. I am standing here (or rather, sitting and writing this) at the finish line and reflecting back on everyone and everything that kept me moving along and got me there. I am filled with so much gratitude for everyone that I feel like I might explode if I don't let them all know how much I appreciate what they've done for me. To this end, I have an inordinate number of people to thank, as follows:

The person I have to thank the most, by far, is Claire. Her love and support throughout my entire program was a panacea, and it is no exaggeration to say she is the primary reason I was able to finish any of this at all. She consoled me, grounded me, inspired me, and kept me going. I owe her for so much of my personal growth and learning throughout grad school, and probably also for what modicum of sanity I have left now at the end. Whether she was near or far, Claire was unwavering in lending her presence of mind and incisiveness (i.e., her "clairevoyance") and got me through a seemingly uncountably infinite number of difficulties I faced, big and small. She is the source of many of my favorite San Diego memories, places to eat, and things to do, and I seriously don't know if I would have made it without her. She is truly a great and wonderful

friend, and probably deserves an honorary PhD of her own at this point.

Never one to let you down, I of course also have to thank Ethan, who is like a brother to me, for his support. Going against the grain of Claire, he is also the person whom I can largely blame for my *in*sanity. To brave the trial by fire of grad school with anyone else alongside me would have been impossible. "Give" is a core tenet Ethan lives by; he was always prepared to help me out at the drop of a hat, and his spontaneity and curiosity continue to both awe me and inspire me. You would probably think us crazy—our surreal conversations almost always seem to exist in some other plane, which has inadvertently warped my mind into some unstable, hyperdimensional object (I don't think I would have it any other way). Up his alley entirely, I am not convinced that my completion of my thesis and PhD are not just facades within the genjutsu he's trapped me under, but if he's doing it to make me happy, is he actually doing anything wrong?

I would be remiss if I didn't thank Hansen and Amanda, and Noah and Rebecca, for all of their love and support from afar, especially throughout the pandemic. They kept me connected in some of my most difficult times, and for as long as we had been friends prior to my PhD, so too do I know they will keep being bastions of love and support for me long afterward, through whatever difficulties I face next in life. We may be well out of our college days now, and yet I still find myself drawn to wanting to play games and have inane conversations with them endlessly until the sun rises. I couldn't ask for a better group of friends from whom I can learn and grow while enjoying every second of it.

I also want to thank Natalie, Akhil, Evgueni, and Ahmed for being awesome friends (on location!) throughout grad school. They were always sources of absurdly fun and interesting conversations and perspectives, and spending time with them was always guaranteed to be enjoyable. Whether it was early on and slogging through the homework, slogging through the pandemic, or slogging through my thesis, these great friends were there to slog through it with me. I am very lucky to have landed in such a relatively small program with such an apparently large pool of dope dudes. It's probably a sign that this is a simulation.

Naturally, I also want to thank my Mom and Dad, and my sisters Heather and Kindy for their bottomless supply of love and praise. They of course have supported me longer than pretty much anyone else I mention here, and their unconditional love has always helped to keep me going through any adversities I've faced, even before grad school. When I moved to San Diego, I was excited to venture away from Urbana on my own, but the pandemic made me feel the pangs of missing being near my family, so I am left feeling particularly appreciative of them lately. I am also quite confident that, despite having the PhD and title and all that jazz, they will still treat me like the baby of the family... That's okay, though, because if you've never been the baby of the family, it's actually pretty sweet.

I want to thank Leslie, too, for helping me tackle the difficulties of grad school and to better understand the operating system my brain runs on. I will always cherish our conversations and how quickly they could turn to the absurd, and I will always think of her whenever I see slugs or volcano snails... Perhaps even gastropods of any variety. Leslie was a source of intense support and unambiguous affirmation in the times when I needed it the most (read: always). I can only wish that every person in the world were able to have their own Leslie.

I want to thank Andrew and Brian for all of their mentorship, advice, and guidance when it comes to teaching, as well as fun discussions about PER and pedagogy. They were immensely helpful in my job searches and gave me lots of great and honest tales of their own experiences job hunting. They were also always super supportive in helping me be a better teacher for my students and provided me with tons of helpful feedback throughout the years. I am very fortunate to have had them as sources of guidance during these formative years in regards to my teaching. I have to thank Brian in particular for being my mentor for the summer course I designed and taught, which was an extremely stressful time—I owe him a ton for his help in getting the class up and running.

I also want to thank the support staff in the Physics department for all of their various help throughout my years at UCSD: Sharmila, Catherine, Saixious, Kevin, Toni, and Dawn. I invariably always had some issue, whether it was with something like paperwork, or with courses,

or simply forgetting to eat, and each of these awesome people were there during one weird issue or another to help me out, including with pizza. They are the unsung heroes (or maybe just sung—everyone I know loves them) of the department, and deserve to be appreciated!

I want to thank Julio, Ertugrul, Aneesh, and Dan for being on my committee, and for their help and feedback on work related to my thesis. I want to additionally thank Julio for always being so supportive of my teaching and helping me throughout my job search, on top of providing me some of my first opportunities to do some real hands-on teaching at UCSD.

And finally, I of course must thank Tongyan and Simon for all of their guidance, advice, support, and *especially* their patience. It is hard for me to imagine how I would have finished my PhD at all without mentors like them. Research was always very difficult for me; the progress can be nebulous, the rewards and feedback are delayed, and it didn't play nicely with the insecurities and doubts that grew like weeds in my brain. Tongyan and Simon were always willing to give me advice about their experiences and try to help me work past these issues, and worked to re-frame tasks and goals to help me accomplish them. I owe pretty much anything I know about dark matter, phenomenology, phonons, and everything in this sphere of knowledge to them. As my advisor, Tongyan deserves particular credit for helping me through all of my hardships and research blocks. It really is tough to imagine I could have finished without her pushing me along, so I will be eternally grateful now that it's finally done!!

Chapter 3, in part, is a reprint of the material as it appears in Brian Campbell-Deem, Peter Cox, Tom Melia, Simon Knapen, Tongyan Lin, Multiphonon excitations from dark matter scattering in crystals, Phys.Rev. D 101 (2020) no.3, 036006, the Erratum: Phys.Rev. D 102 (2020) no.1, 019904, and Brian Campbell-Deem, Simon Knapen, Tongyan Lin, and Ethan Villarama, Dark matter direct detection from the single phonon to the nuclear recoil regime, Phys.Rev. D **106** (2022) no.6, 036019. The dissertation author was one of the primary investigators and authors of these papers.

Chapter 4, in full, is a reprint of the material as it appears in Brian Campbell-Deem, Peter Cox, Tom Melia, Simon Knapen, Tongyan Lin, Multiphonon excitations from dark matter

scattering in crystals, Phys.Rev. D 101 (2020) no.3, 036006 and the Erratum: Phys.Rev. D 102 (2020) no.1, 019904. The dissertation author was one of the primary investigators and authors of this paper.

Chapter 5, in full, is a reprint of the material as it appears in Brian Campbell-Deem, Simon Knapen, Tongyan Lin, and Ethan Villarama, Dark matter direct detection from the single phonon to the nuclear recoil regime, Phys.Rev. D **106** (2022) no.6, 036019. The dissertation author was one of the primary investigators and authors of this paper.

VITA

2017	B.S. in Engineering Physics, University of Illinois Urbana-Champaign, Urbana, IL
2019	M.S. in Physics, University of California San Diego, La Jolla, CA
2022	Ph.D. in Physics, University of California San Diego, La Jolla, CA

PUBLICATIONS

Brian Campbell-Deem, Peter Cox, Tom Melia, Simon Knapen, Tongyan Lin, *Multiphonon excitations from dark matter scattering in crystals*, Phys.Rev. D **101** (2020) no.3, 036006, arXiv: 1911.03482 [hep-ph] (Erratum: Phys.Rev. D **102** (2020) no.1, 019904)

Brian Campbell-Deem, Simon Knapen, Tongyan Lin, Ethan Villarama, *Dark matter direct detection from the single phonon to the nuclear recoil regime*, Phys.Rev. D **106** (2022) no.6, 036019, arXiv: 2205.02250 [hep-ph]

ABSTRACT OF THE DISSERTATION

Phonon Excitation in Cubic Crystal Targets via Dark Matter Scattering

by

Brian Christopher Campbell-Deem

Doctor of Philosophy in Physics

University of California San Diego, 2022

Professor Tongyan Lin, Chair

The scattering of dark matter (DM) particles to excite collective vibrational modes known as *phonons* in crystal targets is a motivated method of observing DM with masses $m_\chi < 1$ MeV. This is due to the matching between the typical energy and momentum imparted into the target and those of the phonons. For heavier dark matter particles with masses $m_\chi \gtrsim 1$ GeV, the scattering is instead point-like off of the individual nuclei in the crystal, rather than collective scattering from many atoms. While the single phonon and nuclear recoil responses are understood, the transition between the two is not. An understanding of this intermediate regime requires a consideration of multiphonon processes, in particular as higher-order corrections that increasingly contribute to the total scattering rate as the typical energy depositions increase. We

utilize several simplifying approximations to arrive at analytic descriptions for multiphonon excitation, allowing us to fully characterize the crystal's phonon response across the relevant mass spectrum for incident DM. Our results allow us to identify the dominant signals to look for in experimental DM searches with cubic crystal targets as a function of the detector energy thresholds.

Chapter 1

Intro to Dark Matter

1.1 Background and Context

Historically, the first inklings of the existence of dark matter came from the observations of Fritz Zwicky in the early 1930s on the velocity dispersion of galaxies in the Coma Cluster [8]. From the observed velocity dispersion profile, by assuming the galaxies are virialized one can then infer the mass of the cluster. Another way to infer the mass of the galaxies (and thus the cluster) however is through measurements of their luminosities, since the mass should be almost entirely comprised of stars within the galaxies. Zwicky found a large discrepancy in these two calculations, however—the galaxies were rotating too quickly for the apparent observable mass to bind them gravitationally, and the velocity measurements implied much more mass was present than visible. Zwicky referred to this apparently non-luminous mass as „dunkle Materie“, i.e. “dark matter”.

Similar conclusions came later in the 1970s from Vera Rubin and her collaborators' measurements of the velocity profiles within the galaxies themselves [9, 10]. Again assuming the galaxies are comprised of virialized matter, mostly in the form of stars, one expects the velocity of stars further from the center to drop after reaching a maximum. Instead, measurements showed a flattening of the velocity profiles, in which they became relatively independent of distance from the galactic center, as shown in Fig. 1.1.

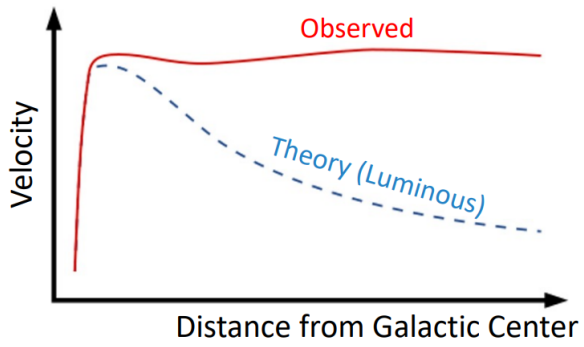

Figure 1.1. Cartoon depicting the type of observed velocity dispersion in galaxies (red) to the expected answer with only luminous matter (blue). Without the presence of extra mass or some other force, the outer stars shouldn't remain gravitationally bounded and would be flung away from the galaxy.

The problem is in analogue to Zwicky's measurements; there seemingly is more mass than is visible contributing to the gravitational binding of the galaxies. Rubin and company concluded that the extra matter (if present) would be in the form of a "halo" centered around the galactic center and would contain ~ 5 times the mass of the luminous ordinary matter.

These original hints into the existence of dark matter are similar in how they manifest, and one might be tempted to solve the problem through another route, e.g. by modifying gravity [11, 12]. We have since however amassed many otherwise unexplained signals and phenomena from independent probes, such as the imprints on the CMB [13, 14], gravitational lensing measurements [15], and the formation of large scale structure in the universe [16, 17]. One of the most compelling pieces of modern evidence (in the form of the aforementioned gravitational lensing) comes from observations of the Bullet Cluster, two colliding clusters of galaxies.

Superimposed images of the Bullet Cluster are shown in Fig. 1.2. We see that most of the mass of the clusters in the form of highly interacting hot gas (captured via x-rays, in magenta) has been disrupted from their collision. If this were to account for most of the mass of the clusters as one might originally expect, we would then expect most of the gravitational lensing to follow them, even in a theory of modified gravity. We instead observe, however, most of the mass

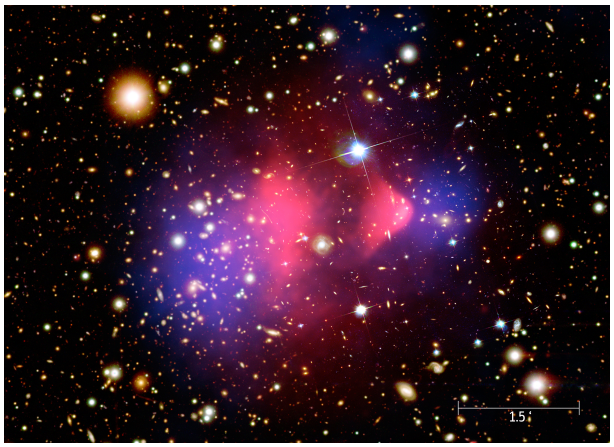

Figure 1.2. Superimposed image of the Bullet Cluster taken in x-rays (magenta) over a visible light photo. The areas highlighted in blue correspond to the matter distribution as sourced by gravitational lensing, which is notably unperturbed from the collision in comparison to the diffused visible matter. Credit: NASA/CXC/CfA/M. Markevitch et al.; NASA/STScI; Magellan/U.Arizona/D. Clowe et al.; NASA/STScI; ESO WFI.

causing the lensing (blue) to have not been strongly displaced from the collision. The presence of dark matter in the clusters, which would not interact strongly during such a collision and therefore pass through mostly unabated, provides a simple explanation as in previous examples.

Given the large amounts of independent indirect observational evidence we have, although we have not directly observed what comprises dark matter, it is consensus among modern physicists that dark matter exists. Our current working cosmological model, ΛCDM, includes the existence of dark matter to help drive the evolution of the universe and is extremely accurate on large scales. Having accepted the existence of dark matter as a concept, the issue at hand then is discovering what thing(s) it actually consists of, and so we must study potential avenues for its formation and properties to inform our experiments to detect it.

1.2 Dark Matter Candidates and Production Mechanisms

It may seem simple to posit e.g. a new particle beyond the standard model (BSM), or even ordinary large composite SM objects like rogue planets or black holes as an explanation for dark matter. One is heavily constrained however by observational evidence (such as those

mentioned in the previous section) that limit the exact masses, interactions, and abundance of a given potential DM candidate. These constraints take form in several properties we know our dark matter candidates must have:

i) Dark matter must be stable, with a lifetime larger than the age of the universe. CMB power spectrum measurements strongly constrain the amount of DM that could have decayed after matter-radiation equality due to the imprints extra e.g. dark radiation would leave.

ii) Dark matter must be cold (non-relativistic) over the history of most galaxy formation. The typical DM velocity around us today is $v \sim 10^{-3}$.

iii) Dark matter must not interact very strongly (either with itself or with SM particles) in order to limit its friend, and probably deserves an honorary PhD of her own at this point. Never one to let you down, I of course also have to thank Ethan, who is like a brother to me, for his support. Going against the grain of Claire, he is also the person whom I can largely blame for my insanity. To brave the trial by fire of grad school with anyone else alongside me would have been impossible. “Give” is a core tenet Ethan lives by; he was always prepared to help me out at the drop of a hat, and his spontaneity and curiosity continue to both awe me and inspire me. You would probably think us crazy—our surreal conversations almost always seem to exist in some other plane, which has inadvertently warped my mind into some unstable, hyperdimensional object (I don’t think I would have it any other way). Up his alley entirely, I am not convinced that my completion of my thesis and PhD are not just facades within the genjutsu he’s trapped me under, but if he’s doing it to make me happy, is he actually doing anything wrong? I would be remiss if I didn’t thank Hansen and Amanda, and Noah and Rebecca, for all of their love and support from afar, especially throughout the pandemic. They kept me connected in some of my most difficult times, and for as long as we had been friends prior to my PhD, so too do I know they will keep being bastions of love and support for me long afterward, through whatever difficulties I face next in life. We may be well out of our college days now, and

yet I still find myself drawn to wanting to play games and have inane conversations with them endlessly until the sun rises. I couldn't ask for a better group of friends from whom I can learn and grow while enjoying every second of it. I also want to thank Natalie, Akhil, Evgueni, and Ahmed for being awesome friends (on location!) throughout grad school. They were always sources of absurdly fun and interesting conversations and perspectives, and spending time with them was always guaranteed to be enjoyable. Whether it was early on and slogging through the homework, slogging through the pandemic, or slogging through my thesis, these great friends were there to slog through it with me. I am very lucky to have landed in such a relatively small program with such an apparently large pool of dope dudes. It's probably a sign that this is a simulation. xiv Naturally, I also want to thank my Mom and Dad, and my sisters Heather and Kindy for their bottomless supply of love and praise. They of course have supported me longer than pretty much anyone else I mention here, and their unconditional love has always helped to keep me going through any adversities I've faced, even before grad school. When I moved to San Diego, I was excited to venture away from Urbana on my own, but the pandemic made me feel the pangs of missing being near my family, so I am left feeling particularly appreciative of them lately. I am also quite confident that, despite having the PhD and title and all that jazz, they will still treat me like the baby of the family... That's okay, though, because if you've never been the baby of the family, it's actually pretty sweet. I want to thank Leslie, too, for helping me tackle the difficulties of grad school and to better understand the operating system my brain runs on. I will always cherish our conversations and how quickly they could turn to the absurd, and I will always think of her whenever I see slugs or volcano snails... Perhaps even gastropods of any variety. Leslie was a source of intense support and unambiguous affirmation in the times when I needed it the most (read: always). I can only wish that every person in the world were able to have their own Leslie. I want to thank Andrew and Brian for all of their mentorship, advice, and guidance when it comes to teaching, as well as fun discussions about PER and pedagogy. They

were immensely helpful in my job searches and gave me lots of great and honest tales of their own experiences job hunting. They were also always super supportive in helping me be a better teacher for my students and provided me with tons of helpful feedback throughout the years. I am very fortunate to have had them as sources of guidance during these formative years in regards to my teaching. I have to thank Brian in particular for being my mentor for the summer course I designed and taught, which was an extremely stressful time—I owe him a ton for his help in getting the class up and running. I also want to thank the support staff in the Physics department for all of their various help throughout my years at UCSD: Sharmila, Catherine, Saixious, Kevin, Toni, and Dawn. I invariably always had some issue, whether it was with something like paperwork, or with courses, xv or simply forgetting to eat, and each of these awesome people were there during one weird issue or another to help me out, including with pizza. They are the unsung heroes (or maybe just sung—everyone I know loves them) of the department, and deserve to be appreciated! I want to thank Julio, Ertugrul, Aneesh, and Dan for being on my committee, and for their help and feedback on work related to my thesis. I want to additionally thank Julio for always being so supportive of my teaching and helping me throughout my job search, on top of providing me some of my first opportunities to do some real hands-on teaching at UCSD. And finally, I of course must thank Tongyan and Simon for all of their guidance, advice, support, and especially their patience. It is hard for me to imagine how I would have finished my PhD at all without mentors like them. Research was always very difficult for me; the progress can be nebulous, the rewards and feedback are delayed, and it didn't play nicely with the insecurities and doubts that grew like weeds in my brain. Tongyan and Simon were always willing to give me advice about their experiences and try to help me work past these issues, and worked to re-frame tasks and goals to help me accomplish them. I owe pretty much anything I know about dark matter, phenomenology, phonons, and everything in this sphere of knowledge to them. As my advisor, Tongyan deserves particular credit for helping me through all of my hardships and research blocks.

It really is tough to imagine I could have finished without her pushing me along, so I will be eternally grateful now that it's finally done!! Chapter 3, in part, is a reprint of the material as it appears in Brian Campbell-Deem, Peter Cox, Tom Melia, Simon Knapen, Tongyan Lin, Multiphonon excitations from dark matter scattering in crystals, Phys.Rev. D 101 (2020) no.3, 036006, the Erratum: Phys.Rev. D 102 (2020) no.1, 019904, and Brian Campbell-Deem, Simon Knapen, Tongyan Lin, and Ethan Villarama, Dark matter direct detection from the single phonon to the nuclear recoil regime, Phys.Rev. D 106 (2022) no.6, 036019. The dissertation author was one of the primary investigators and authors of these papers. Chapter 4, in full, is a reprint of the material as it appears in Brian Campbell-Deem, Peter Cox, Tom Melia, Simon Knapen, Tongyan Lin, Multiphonon excitations from dark matter xvi scattering in crystals, Phys.Rev. D 101 (2020) no.3, 036006 and the Erratum: Phys.Rev. D 102 (2020) no.1, 019904. The dissertation author was one of the primary investigators and authors of this paper. Chapter 5, in full, is a reprint of the material as it appears in Brian Campbell-Deem, Simon Knapen, Tongyan Lin, and Ethan Villarama, Dark matter direct detection from the single phonon to the nuclear recoil regime, Phys.Rev. D 106 (2022) no.6, 036019. The dissertation author was one of the primary investigators and authors of this paper. xvii VITA 2017 B.S. in Engineering Physics, University of Illinois Urbana-Champaign, Urbana, IL 2019 M.S. in Physics, University of California San Diego, La Jolla, CA 2022 Ph.D. in Physics, University of California San Diego, La Jolla, CA PUBLICATIONS Brian Campbell-Deem, Peter Cox, Tom Melia, Simon Knapen, Tongyan Lin, Multiphonon excitations from dark matter scattering in crystals, Phys.Rev. D 101 (2020) no.3, 036006, arXiv: 1911.03482 [hep-ph] (Erratum: Phys.Rev. D 102 (2020) no.1, 019904) Brian Campbell-Deem, Simon Knapen, Tongyan Lin, Ethan Villarama, Dark matter direct detection from the single phonon to the nuclear recoil regime, Phys.Rev. D 106 (2022) no.6, 036019, arXiv: 2205.02250 [hep-ph] xviii ABSTRACT OF THE DISSERTATION Phonon Excitation in Cubic Crystal Targets via Dark Matter Scattering by Brian Christopher Campbell-Deem Doctor of Philosophy

in Physics University of California San Diego, 2022 Professor Tongyan Lin, Chair The scattering of dark matter (DM) particles to excite collective vibrational modes known as phonons in crystal targets is a motivated method of observing DM with masses m ¡ 1 MeV. This is due to the matching between the typical energy and momentum imparted into the target and those of the phonons. For heavier dark matter particles with masses m 1 GeV, the scattering is instead point-like off of the individual nuclei in the crystal, rather than collective scattering from many atoms. While the single phonon and nuclear recoil responses are understood, the transition between the two is not. An understanding of this intermediate regime requires a consideration of multiphonon processes, in particular as higher-order corrections that increasingly contribute to the total scattering rate as the typical energy depositions increase. We xix utilize several simplifying approximations to arrive at analytic descriptions for multiphonon excitation, allowing us to fully characterize the crystal's phonon response across the relevant mass spectrum for incident DM. Our results allow us to identify the dominant signals to look for in experimental DM searches with cubic crystal targets as a function of the detector energy thresholds. xx Chapter 1 Intro to Dark Matter 1.1 Background and Context Historically, the first inklings of the existence of dark matter came from the observations of Fritz Zwicky in the early 1930s on the velocity dispersion of galaxies in the Coma Cluster [8]. From the observed velocity dispersion profile, by assuming the galaxies are virialized one can then infer the mass of the cluster. Another way to infer the mass of the galaxies (and thus the cluster) however is through measurements of their luminosities, since the mass should be almost entirely comprised of stars within the galaxies. Zwicky found a large discrepancy in these two calculations, however—the galaxies were rotating too quickly for the apparent observable mass to bind them gravitationally, and the velocity measurements implied much more mass was present than visible. Zwicky referred to this apparently non-luminous mass as „dunkle Materie“, i.e. “dark matter”. Similar conclusions came later in the 1970s from Vera Rubin and her collaborators' measurements of the velocity profiles within the

galaxies themselves [9 , 10]. Again assuming the galaxies are comprised of virialized matter, mostly in the form of stars, one expects the velocity of stars further from the center to drop after reaching a maximum. Instead, measurements showed a flattening of the velocity profiles, in which they became relatively independent of distance from the galactic center, as shown in Fig. 1.1. 1 Figure 1.1. Cartoon depicting the type of observed velocity dispersion in galaxies (red) to the expected answer with only luminous matter (blue). Without the presence of extra mass or some other force, the outer stars shouldn't remain gravitationally bounded and would be flung away from the galaxy. The problem is in analogue to Zwicky's measurements; there seemingly is more mass than is visible contributing to the gravitational binding of the galaxies. Rubin and company concluded that the extra matter (if present) would be in the form of a "halo" centered around the galactic center and would contain 5 times the mass of the luminous ordinary matter. These original hints into the existence of dark matter are similar in how they manifest, and one might be tempted to solve the problem through another route, e.g. by modifying gravity [11, 12]. We have since however amassed many otherwise unexplained signals and phenomena from independent probes, such as the imprints on the CMB [13, 14], gravitational lensing measurements [15], and the formation of large scale structure in the universe [16, 17]. One of the most compelling pieces of modern evidence (in the form of the aforementioned gravitational lensing) comes from observations of the Bullet Cluster, two colliding clusters of galaxies. Superimposed images of the Bullet Cluster are shown in Fig. 1.2. We see that most of the mass of the clusters in the form of highly interacting hot gas (captured via x-rays, in magenta) has been disrupted from their collision. If this were to account for most of the mass of the clusters as one might originally expect, we would then expect most of the gravitational lensing to follow them, even in a theory of modified gravity. We instead observe, however, most of the mass 2 Figure 1.2. Superimposed image of the Bullet Cluster taken in x-rays (magenta) over a visible light photo. The areas highlighted in blue correspond to the matter distribution

as sourced by gravitational lensing, which is notably unperturbed from the collision in comparison to the diffused visible matter. Credit: NASA/CXC/CfA/M. Markevitch et al.; NASA/STScI; Magellan/U.Arizona/D. Clowe et al.; NASA/STScI; ESO WFI. causing the lensing (blue) to have not been strongly displaced from the collision. The presence of dark matter in the clusters, which would not interact strongly during such a collision and therefore pass through mostly unabated, provides a simple explanation as in previous examples. Given the large amounts of independent indirect observational evidence we have, although we have not directly observed what comprises dark matter, it is consensus among modern physicists that dark matter exists. Our current working cosmological model, CDM , includes the existence of dark matter to help drive the evolution of the universe and is extremely accurate on large scales. Having accepted the existence of dark matter as a concept, the issue at hand then is discovering what thing(s) it actually consists of, and so we must study potential avenues for its formation and properties to inform our experiments to detect it. 1.2 Dark Matter Candidates and Production Mechanisms It may seem simple to posit e.g. a new particle beyond the standard model (BSM), or even ordinary large composite SM objects like rogue planets or black holes as an explanation for dark matter. One is heavily constrained however by observational evidence (such as those 3 effects on early-universe evolution and maintain the distribution and structure we observe today.

These constraints nevertheless leave an enormous range of possible masses—around 80 orders of magnitude, as shown in Fig. 1.3—of different dark matter candidates corresponding to various production mechanisms and detection signatures. The mass bounds are not extremely hard-and-fast numbers, but each come roughly from arguments about structure formation. As the low end, the DM has an astrophysical-scale de Broglie wavelength, around the size of dwarf galaxies. At smaller masses, such light DM could not saturate the total abundance as DM-dominated dwarf galaxies would not be able to form [18, 19]. More recent astrophysical data bounds on the density profiles of dwarf galaxies are in accordance with this bound, and

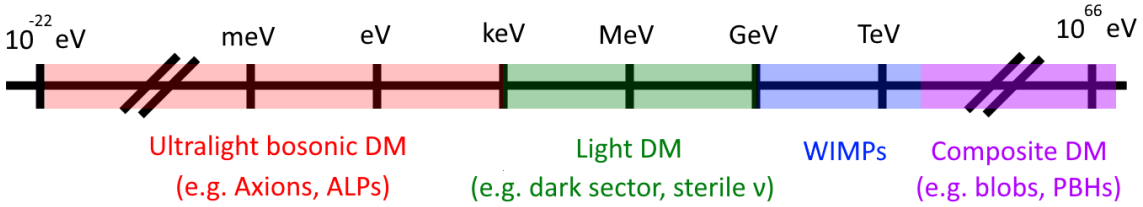

Figure 1.3. An illustrative picture of the wide mass range of possible dark matter particles, corresponding to different categories of dark matter and relevant production mechanisms.

possibly even an order of magnitude more strict [20]. On the high end, beyond 10^3 solar masses ($M_\odot = 10^{66}$ eV) or more, the DM becomes too coarsely grained and the time-dependence of the gravitational potential disrupts e.g. globular cluster formation [21].

One may be tempted to try and simultaneously solve other open problems in the SM with a dark matter candidate; the QCD axion, for example, arose as a potential solution to the strong-CP problem, and was thereafter found to be a viable dark matter candidate [22]. Similar ultralight axion-like particles (ALPs) can also fall out as more generic predictions of string theories [23] and in turn address other problems, e.g. small scale structure via fuzzy DM [18]. Another example comes from the hierarchy problem, which concerns the apparent largely "fine-tuned" cancellations needed to achieve such a large discrepancy between the Higgs mass and a natural mass scale like $M_{\rm Pl}$. The problem can be addressed if new weak-scale physics exists around 10 GeV-Tev; this motivates WIMP candidates [24] (blue in Fig. 1.3), which will be discussed in more detail shortly.

Being momentarily more agnostic to whether another problem may be simultaneously solved, the simplest type of origin for dark matter one might consider could be DM thermally produced in the early universe in analogy to ordinary matter. We observe ordinary matter relics—photons, neutrinos, baryons, etc.—which were at one point all in thermal equilibrium. If we assume dark matter was also in thermal equilibrium with the SM at this time, then when precisely it leaves equilibrium will influence the amount of dark matter left that we observe today. Once it has left thermal equilibrium, the amount or DM in the universe will be primarily driven by how often it is annihilating back into SM particles, but this will quickly become inefficient. When

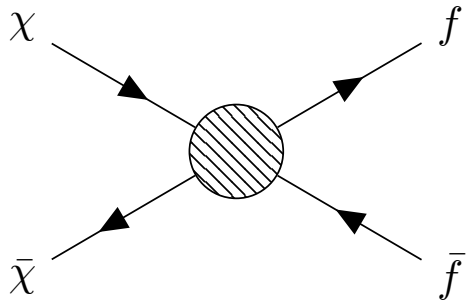

Figure 1.4. Illustration of generic annihilation of dark matter particles $\chi, \bar{\chi}$ into SM particles $f, \bar{f}$. After the DM has cooled sufficiently to leave thermal equilibrium with the SM, the evolution of the amount of DM in the universe is primarily driven by annihilation into SM particles, which depletes the density until freezeout occurs. The blob in the middle represents some interaction(s), whose identities (as well as those of the precise particles involved) is left unspecified.

the DM can no longer efficiently annihilate with itself, the amount will essentially stay fixed, with the number density simply scaling with expansion; this process of leaving equilibrium and becoming "stuck" in number is known as *thermal freezeout*. By using the observed local dark matter density today, we could then use this to inform when freezeout occurred. Additionally, the original assumption of thermal equilibrium necessitates some type of interaction(s) between the DM and SM we could potentially probe today, such as signatures in the other SM relics, e.g. the CMB power spectrum.

Following this motivation, one can do simple estimates for a general picture of what thermal freezeout to produce the observed relic abundance would look like [25]. As discussed earlier, freezeout occurs quickly once dark matter leaves thermal equilibirum with the SM and can no longer annihilate into SM particles. This condition is realized then when the DM annihilation rate Γ drops below the Hubble rate H

$$\Gamma = n_{\chi}^{\mathrm{eq}} \langle \sigma v \rangle = H \tag{1.1}$$

as the DM can no longer efficiently find partners to annihilate with. Here, $\langle \sigma v \rangle$ is the thermally averaged annihilation cross-section times velocity.

A helpful quantity to consider now is the *abundance* $Y_{\chi} = n_{\chi}/s_{\gamma}$, where n_{χ} is the dark

matter number density and s_γ is the entropy density of relic (CMB) photons. In the absence of sufficient number-changing processes in comparison to the expansion of the universe, as we have once freezeout occurs, this number remains essentially constant from freezeout onward. Matching the dark matter energy density observed today ρ_χ gives a simple benchmark requirement for the abundance at freezeout: $Y_{\chi,\mathrm{fo}} \sim \mathrm{eV}/m_\chi$.

Combining this condition with the abundance benchmark $Y_\chi = n_\chi/s_\gamma$ allows one to estimate n_χ at freezeout; we may in turn finally from (1.1) arrive at a benchmark annihilation cross-section [24]:

$$\langle \sigma v \rangle \approx 2 \times 10^{-26} \mathrm{cm}^3/\mathrm{s} \approx \frac{\alpha_w^2}{1\,\mathrm{TeV}^2} \tag{1.2}$$

This is of particular historical significance, as the cross-section arrived at through this calculation appears to match onto the the annihilation cross-section one would expect for a new weak-scale weakly-interacting particle, as shown in the right-hand side of (1.2) for a coupling strength $\alpha_w \sim \mathcal{O}(10^{-2})$. Such particles of masses few GeV $\lesssim m_\chi \lesssim$ few TeV came to be referred to as Weakly Interacting Massive Particles, or WIMPs, and the apparent coincidence between the cross-sections came to be known as the "WIMP miracle".

1.3 Toward the WIMP Paradigm...

We began agnostic to whether a thermal DM candidate had other motivations, but have arrived at the potential for WIMPs as viable DM candidates amidst this WIMP miracle. Moreover, WIMPS are readily produced from e.g. SM extensions [26, 27], adding to the apparent miracle. This has motivated many searches for WIMP DM around this mass range—although there were (and are) many experiments and analyses searching for DM of other types, the prevailing candidate of choice in the community became WIMPs.

This brings our discussion to the channels for how one might actually go about observing dark matter in an experiment, which are depicted succinctly in Fig. 1.5 by following the Feynman diagram in different directions. For example, left-to-right involves direct *production* of DM

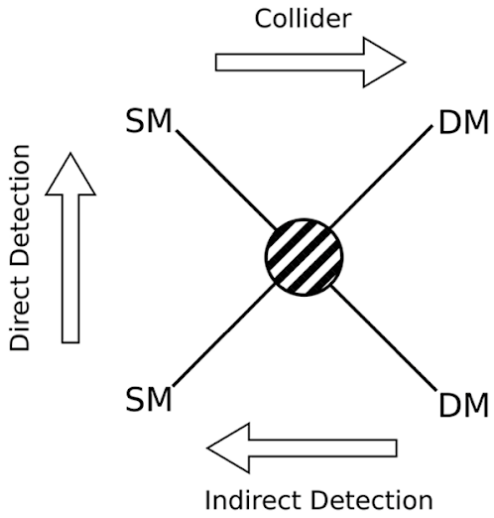

Figure 1.5. Cartoon depicting the three channels of observing dark matter, as determined by which way you follow the interaction.

by SM particles in a collider experiment, i.e. making new DM particles to study rather than observing those that already exist today. Running the figure in reverse instead involves looking for the SM signatures (e.g. excesses in gamma rays) from the annihilation of dark matter into SM particles, known as *indirect detection* as we observe only the byproducts of the DM. It is the remaining channel, running the figure from bottom-to-top, that we are interested in for the remaining discussion of this Thesis. This channel is known as *direct detection*, in which dark matter enters our lab and interacts directly with our experiment and detectors (which are made of SM particles) leaving behind signatures of its presence. From the type of interaction, energy and momentum deposited, etc., we can reconstruct properties of the dark matter particle(s) involved, if observed, or instead place constraints on those types of particles and properties if not observed.

More explicit aspects and an example of WIMP searches are discussed in Chapter 2, but from considering these types of interactions we can already imagine what WIMP searches might look like. For example, the LHC runs at TeV scale energies looking to produce new particles, and so it is already naturally looking in the window where one might expect a WIMP to appear. In direct detection experiments would could instead build targets (e.g. crystals or heavier liquids) for the WIMPs to scatter off of, depositing their energy and momentum that we

collect. In these experiments, heavy nuclei are chosen for their similar mass scale to the WIMP candidates so that there is kinematic matching, with typical energy depositions $\sim m_\chi v^2$ around the keV scale–energies that are (were) already very realistic to meet. There is an additional enhancement from coherent scattering leading to the cross section scaling with the square of the nucleon number, further favoring heavier target nuclei.

1.4 ...And away from the WIMP Paradigm

Only in somewhat recent years has this interest begun to shift, as the phase space for potential WIMP DM has been continually and increasingly squeezed through observational constraints [28, 29]. The motivation behind WIMPs and limits of the detectors used are discussed in more detail in Chapter 2, however the operating energies of the LHC and keV thresholds in direct detection experiments mean that these exclusions are primarily for DM with $m_\chi > 1$ GeV. It is worth considering what the overall mass range for thermal candidates are, however, as WIMPs are not the sole candidate of this type. At the high end, thermal candidates are limited to masses of around ~ 100 TeV due to the unitarity limit [30], beyond which thermal candidates would overclose the amount of DM present in the universe today. The lower bound is well below WIMP masses, however, at around $\sim$ few keV. Here the limit is placed by "warm DM" bounds—thermal candidates below keV masses that were in thermal equilibrium do not satisfy the cold requirement of Sec. 1.2. They are instead produced too relativistic, and would dampen the matter power spectrum beyond what is observed. The warm DM bound means a viable thermal candidate with $m_\chi \gtrsim 1$ keV must be able to have $Y_{\rm fo} \ll 1$ according to the abundance benchmark in Sec. 1.2. This is readily obtained however for a non-relativistic species (in a self-consistent way) as the equilibrium number density $n_\chi^{\rm eq} \propto e^{-m_\chi/T}$ is Boltzmann suppressed. This leaves a region keV $\lesssim m_\chi \lesssim$ GeV of viable thermal DM candidates which has not been historically probed to nearly the extent as that of WIMPs. These candidates of masses keV $\lesssim m_\chi \lesssim$ GeV are known as *light dark matter* (LDM).

Light dark matter will generically invoke e.g. new light mediators (as opposed to weak mediators for WIMPs) in order to have a sufficiently large annihilation cross section to reduce the DM population to the correct amount at freezeout [31]. These new mediators present the possibility for new physics, and in particular could act as "portals" to a new "dark sector" potentially populated by multiple species [32, 33]. Such new mediators and the possibility dark sectors including thermal LDM present interesting new experimental signatures in a regime that was previously unexplored in favor of WIMP searches. For example, the mediators could be bosons presenting a different type of interaction than a weak mediator; the lower mass of LDM also enforces different kinematic constraints than that of WIMP nuclear recoils, as those nuclei would be much heavier than the DM and mediators. Rather than $\sim$keV recoil energies, they instead would be as low as $\sim$meV, and the interactions would instead be with multiple atoms as the wavelength of the deposited momentum begins exceeding the typical atomic spacing. These lower energy scales and collective interactions would necessarily present themselves with different signatures in the experiments.

So, rather than necessarily being motivated by solving another outstanding problem in physics or exploring models out of intellectual interest, we can be driven by searches and data that are achievable within the next decade but may not have been addressed yet. It is toward these appeals that we will begin discussing potential mechanisms and signatures that may be used to detect LDM experimentally. With our interest in LDM suitably piqued, and knowing that the experimental signatures will differ from those already sought by WIMP experiments, our goal now is to investigate the interaction mechanisms and experiments that would be able to probe the direct detection of LDM.

Chapter 2

Intro to Direct Detection

In this Chapter, we now move toward a description of the actual direct detection frontier and experiments in more detail. We begin with a short discussion of the direct detection background and experimental side of the WIMP paradigm as an illustrative example. We will then work toward uncovering phonon excitation as a motivated method of directly detecting sub-GeV DM, following our motivation to look for non-WIMP thermal candidates. We finally conclude with an example of a proposed sub-GeV phonon experiment to contextualize the discussion of phonons.

2.1 Direct Detection with WIMP Example

In considering a weakly-interacting GeV-TeV scale particle (typically also a fermion) the natural target to consider are atomic nuclei, which are of a somewhat similar mass and whose nucleons interact via the weak force. It is sufficient to discuss the scattering at a macroscopic level, characterizing the cross section generally in terms of spin-dependent and spin-independent *form factors* that encode the more precise structure of the nucleus and the interaction itself. We begin by writing down the differential cross section for the scattering with respect to the nuclear recoil energy E_{NR} [34] :

$$\frac{d\sigma}{dE_{\mathrm{NR}}} = \frac{m_N}{2v^2{\mu_n}^2}\left(\sigma_{\mathrm{SI}}{F_{\mathrm{SI}}}^2(E_{\mathrm{NR}}) + \sigma_{\mathrm{SD}}{F_{\mathrm{SD}}}^2(E_{\mathrm{NR}})\right) \tag{2.1}$$

Here, m_N is the mass of the nucleus, μ_n is the DM-*nucleon* reduced mass, and the F_i functions are the aforementioned form factors for the **S**pin **I**ndependent and **S**pin **D**ependent interactions, respectively. As an example, a typical SI form factor taken is the classic nuclear-scattering Helm form factor, meant to model the substructure of the nucleus for WIMPs heavy enough to probe those length scales.

From the differential cross section, we could construct the total scattering event rate R by considering the DM velocity distribution $f(v)$ and integrating over allowed velocities and energy transfers in the volume of the target. For most NR analyses, the discussion is usually instead about the differential scattering rate, also called the (recoil) spectrum:

$$\frac{dR}{dE_{\mathrm{NR}}} = \frac{\rho_\chi}{m_\chi}\frac{1}{m_N}\int d^3\mathbf{v}\, v f(\mathbf{v})\,\frac{d\sigma}{dE_{\mathrm{NR}}}\Theta\left(v - v_{\mathrm{min}}(E_{\mathrm{NR}})\right) \tag{2.2}$$

Specifically, this is the differential scattering rate per unit exposure, and can be converted to the total differential scattering rate by multiplying by the total mass of the target and time elapsed (i.e. the total exposure). The bounds of the velocity integral are determined below by the minimum velocity v_{min} that can induce a recoil of energy E_{NR} and above by the escape velocity v_{esc} of the dark matter in the lab frame, which typically truncates the velocity distribution.

Conservation of energy between an incident DM particle of velocity $\mathbf{v}$ on a free nucleus of mass m_N requires

$$\frac{\mathbf{q^2}}{2m_N} = \frac{1}{2}m_\chi v^2 - \frac{\left(m_\chi \mathbf{v} - \mathbf{q}\right)^2}{2m_\chi} \tag{2.3}$$

$$\longrightarrow \qquad \frac{\mathbf{q^2}}{2\mu_N} = \mathbf{q}\cdot\mathbf{v} \tag{2.4}$$

with $\mathbf{q}$ the momentum transfer to the nucleus and $\mu_N \equiv \frac{m_\chi m_N}{m_\chi + m_N}$ the DM-*nucleus* reduced mass. The righthand side of (2.4) is maximized when $\mathbf{q}$ and $\mathbf{v}$ are aligned, i.e. $\mathbf{q}\cdot\mathbf{v} = qv$, and thus the maximum momentum transfer is given by $\mathbf{q}_{\mathrm{max}} = 2\mu_N v$. With some example masses m_χ, m_N in the neighborhood of $10 - 100$ GeV and a typical DM velocity of $v \sim 10^{-3}$, we see the

typical recoil energy is around 10-100 keV given that $E_{\rm NR} \equiv q^2/2m_N$. It is for this reason NR detectors push for energy thresholds down to $\sim$few keV. We may also derive the form of $v_{\rm min}(E_R)$ from (2.4) and the definition of E_R:

$$E_R = \frac{q^2}{2m_N} = \frac{(2\mu_N v_{\rm min})^2}{2m_N} \tag{2.5}$$

$$\longrightarrow \quad v_{\rm min} = \sqrt{\frac{m_N E_R}{2\mu_N^2}} \tag{2.6}$$

For WIMP direct detection searches, there are a few leading types of general experimental setups, however the dominant type (currently pressing the highest exclusion sensitivity, at least for SI nuclear recoils) are *noble liquid detectors*. These detectors involve large tanks of liquid noble gases (usually Xenon or Argon) cooled to cryogenic temperatures acting as a sizable, dense target for the DM to interact with. Examples of leading noble liquid detectors are (were) LZ and XENON1T (now running as XENONnT). In these experiments, many steps are taken to reduce backgrounds, such as operating deep underground, being shielded, repeatedly filtering the liquids, and special care taken to build the setup out of materials that are not cosmogenic or (too) radioactive. When a dark matter particle scatters inside of these detectors, scintillation light is produced, which is captured by PMTs; in *single-phase detectors*, this is the only signal measured. If a strong electric field is applied, ionization electrons may be prevented from recombining and instead measured as secondary, separate signal (S2) in addition to the scintillation light (S1), as is performed in *time-projection chambers*.

Having discussed the squeeze on WIMP parameter space several times by now, we may finally see example limits placed by WIMP experiments on the spin-independent nucleon cross section in Fig. 2.1. Through lack of observation, the size of the nucleon cross sections may be bounded with some statistical confidence (90% C.L. in Fig. 2.1), eliminating those cross sections and above[1] to that degree of certainty. In this figure, we observe the difficulty in exclusions

[1]Eventually, for very large cross sections above the bounds, they may not actually be ruled out since they would scatter in the Earth before reaching the detector.

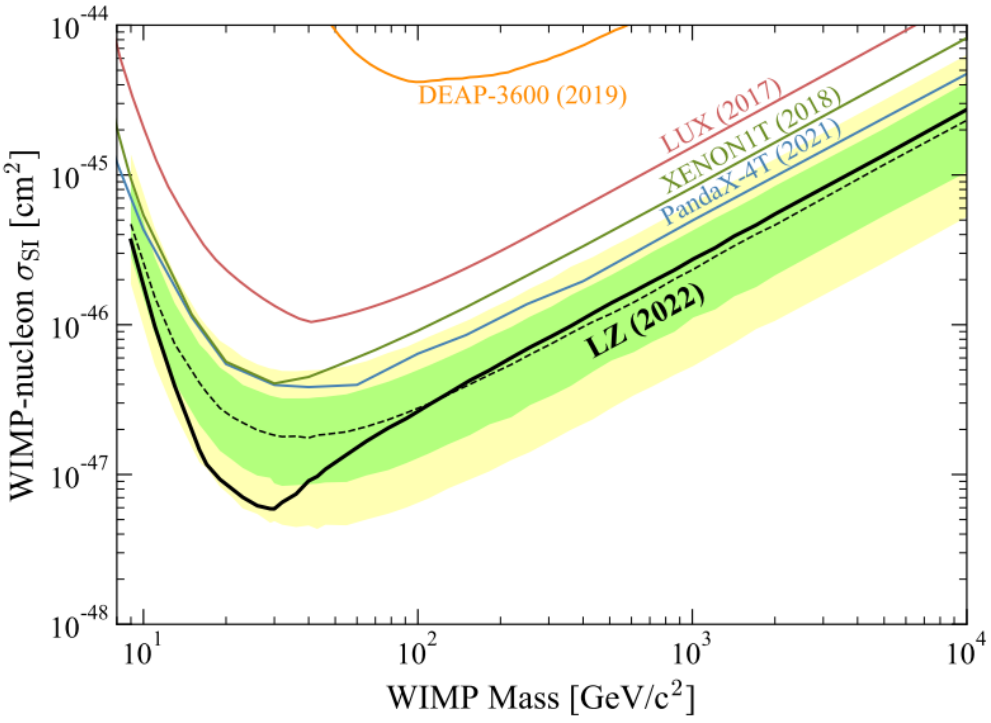

Figure 2.1. A comparison of current limits on the spin-independent WIMP-nucleon cross section from WIMP searches, reproduced from [1]. The solid black line represents the 90% confidence limit, while the green and yellow areas represent 1σ and 2σ sensitivity bands, respectively.

beginning below 10 GeV masses; as the typical WIMP energy depositions drop below $\sim$10 keV, the experimental energy thresholds begin limiting the sensitivity and the curves sharply rise. The frontier of observed bounds is now edging very near the neutrino floor (not pictured in Fig. 2.1) and to date no WIMPs have been detected[2]. These bounds have pushed e.g. Z mediated scattering with expected coupling strengths off of the precipice, requiring instead smaller couplings or new other new mediators [25]. Reducing the coupling strengths cannot be done arbitrarily however, as this also reduces the annihilation cross-section and causes freezeout to occur earlier meaning we run into problems obtaining the relic abundance. This gradual reduction in the types of masses, mediators, and/or coupling strengths the witnesses of the WIMP miracle may have been previously expecting to comprise DM has thus begun to drive the consensus away from the WIMP paradigm in favor of other possibilities.

[2]DAMA observed annual signal modulation that would be expected from the Earth's revolution around the sun relative to the DM wind; the results are however widely disputed and have not been reproduced elsewhere.

2.2 Introducing: Phonons

We now move on toward a description of an alternative process from nuclear recoil that is relevant for LDM: excitation of *phonons*. A precise mathematical description and derivation of the nature of phonons is contained in the next Chapter; we instead begin here to first understand what phonons are more qualitatively. One is most likely familiar with vibrations in a medium that propagate as waves, e.g. sound in air; phonons are the quantized excitations of these vibrations, particularly in our case in a crystal. That is to say, the collective effect of the motion of the atoms in the lattice may be understood in more familiar particle language (mode expansion in terms of operators, carrying energy and momentum, etc.) where the "particles" are the phonons.

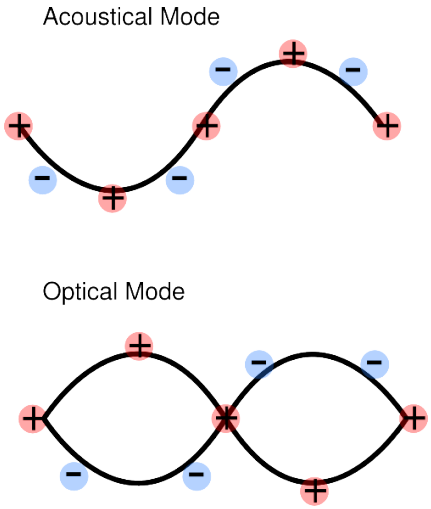

Figure 2.2. Visualization of the two types of phonons in a 1D crystal with two types of atoms. For the acoustic phonon, the neighboring atoms move in phase; for the optical, they move oppositely to one another. Credit: University of Warwick Department of Physics.

To visualize the phonons, let us consider a simple 1D crystal (a chain of atoms) with two distinct alternating types of atoms, as shown in Fig. 2.2. The distinction allows us to characterize the two types of phonons that emerge; the acoustic phonons are those shown in the top of the figure, in which neighboring atoms move together in the same direction. The optical phonons are instead those in which the differing atoms move oppositely to one another. The "optical"

nomenclature comes historically from the ease of exciting these phonons in certain crystals optically, in particular those in which the two atoms have opposite charges. Had we considered a crystal of only one type of atom, we would then lose the distinction, and instead have only acoustic phonons. Generalizing this picture to a 3D crystal, we gain the further distinction of polarizations for the phonons; the atoms may oscillate in the direction of the phonon's momentum (*longitudinal* polarization) or perpendicular to it (*transverse* polarization, of which there are two distinct possibilities).

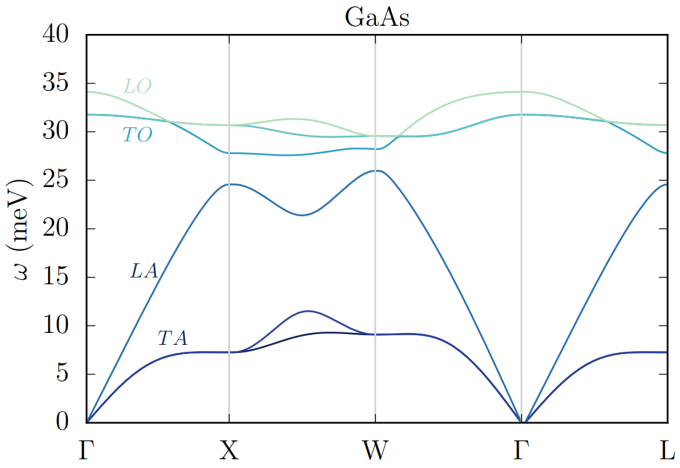

Figure 2.3. An example of the phonon band structure in a crystal with two distinct atoms, gallium arsenide (GaAs) [2]. The origin of the Brillouin zone (BZ) is the point Γ, where $\mathbf{q} = \mathbf{0}$, with the other points on the axes being various directions in the first BZ. The labels indicate first the polarization (longitudinal or transverse) followed by the type (acoustic or optical).

We typically denote the spacing between atoms (or between unit cells, if multiple different atoms are present) with the lattice constant a. The spatial structure of the crystal lattice has a corresponding reciprocal lattice in momentum space. The primitive cell centered at the origin of this reciprocal lattice space is known as the *first Brillouin zone* and in the isotropic case would have a size $q_{\mathrm{BZ}} = 2\pi/a$. The origin of the first BZ is denoted by the symbol Γ, with different directions toward the edges of the first BZ denoted by various other symbols depending on the precise symmetry structure of the lattice.

We may now consider what the actual dispersion relations in an example crystal look

like; Fig. 2.3 features the band structure in GaAs. Here, we may see the low-momentum features of the phonons, in which the dispersion relation for acoustic phonons is approximately linear

$$\omega_\nu = c_\nu |\mathbf{k}| \tag{2.7}$$

with c_ν being the speed of sound of that particular acoustic phonon ν carrying a momentum $\mathbf{k}$. Physically, because the acoustic phonons involve the atoms moving together in the same direction, the acoustic phonons with no momentum also carry no energy (i.e. there is no motion). This can also be understood as representative of the fact that the acoustic phonons are the Goldstone bosons generated by the broken continuous translational symmetry of the crystal, and so the linear dispersion tending to zero energy at zero momentum is expected. The optical phonons however are gapped and have $\gtrsim 10$ meV of energy at arbitrarily low momentum transfer; their dispersions are also generally less momentum dependent, allowing us to usually treat them as being effectively flat.

2.3 Direct Detection with Phonons

For kinematic reasons, the sub-GeV regime is especially challenging for DM which primarily couples to hadronic matter. For a DM mass m_χ below 1 GeV with a typical nucleus mass $m_N \gtrsim$ few GeV, we have $\mu_N \approx m_\chi$, and we therefore see from (2.4) that the energy sub-GeV DM can deposit in an elastic collision with a nucleus is bounded by

$$E_N \leq \frac{{\mathbf{q}_{\max}}^2}{2m_N} = \frac{2v^2 m_\chi^2}{m_N}. \tag{2.8}$$

For $m_\chi \ll m_N$ this is only a small fraction of the total available DM kinetic energy, which can make it very difficult to detect. This problem can be mitigated to some extent by choosing light element targets such as H [35], He [36, 37, 38], or diamond [39] and by pushing for lower thresholds.

For masses below 1 MeV, however, DM-nucleus scattering is no longer subject to (2.8); the reason is that its de Broglie wavelength exceeds the interparticle spacing in typical materials, and it becomes necessary to transition to a different effective theory by integrating out the nuclei and electron clouds and instead treat it as a collective mode of many atoms rather than a single nucleus. The collective modes of interest are the aforementioned phonons. We saw previously in Fig. 2.3 some typical phonon energies for GaAs; we can see that these indeed match onto the kinematics of sub-MeV DM, as shown in the phase space plot of Fig. 2.4.

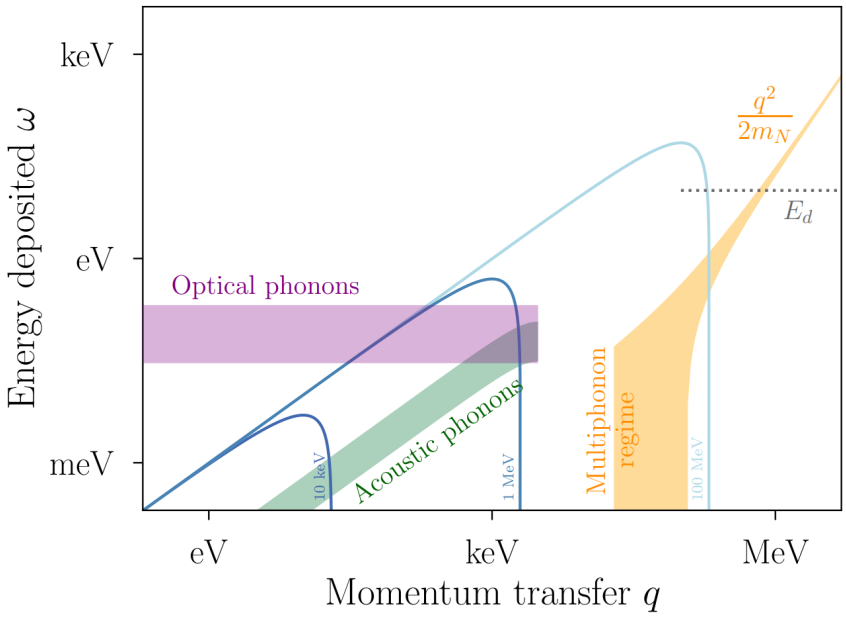

Figure 2.4. Phase space plot in (q, ω) with sample DM masses of $m_\chi = 10$ keV, 1 MeV, and 100 MeV with $v = 10^{-3}$ reproduced from [3]. The lines represent the allowed curve in phase space along which that DM mass satisfies its kinematic conditions. The superimposed regions denote regimes of typical response signals. Below $q \sim$ keV, the matching signals are those of single optical and acoustic phonons (described more explicitly in Chapter 3). Above the typical displacement energy E_d the response is the standard nuclear recoil dicussed for WIMPs. In between these two regions, the nuclear recoil response broadens and is more aptly described as excitation of multiple phonons, displaying physically how the two extremes are connected.

In this figure, we precisely see this aforementioned breakdown of the nuclear recoil description into a regime where phonons are relevant. Our nuclear recoil cross sections are no longer the relevant description in the case of LDM; we must instead obtain the DM-nucleon

cross section involving phonon excitation. This differential cross section instead looks like

$$\frac{d\sigma}{d^3\mathbf{q}\,d\omega} = \frac{b_p^2}{{\mu_p}^2}\frac{1}{v}|\tilde{F}(\mathbf{q})|^2 S(\mathbf{q},\omega)\,\delta\left(\omega-\omega_{\mathbf{q}}\right) \tag{2.9}$$

where b_p is the DM-proton scattering length (connected to the DM-proton cross section via $\sigma_p = 4\pi {b_p}^2$), $|\tilde{F}(\mathbf{q})|^2$ is a form factor that depends on the mass limit of the mediator, and $S(\mathbf{q},\omega)$ is the *structure factor*. We leave a derivation and discussion of the full form of the identity of the structure factor until Chapter 3, so now we may treat it in a similar way as the previous nuclear form factors in that it encodes the DM-crystal interaction and phonon response. The final delta function in this form is merely there to enforce kinematic matching of the energy deposited ω matching onto $\omega_{\mathbf{q}} = \mathbf{q}\cdot\mathbf{v} - q^2/2m_\chi$.

As before, this naturally connects to the total event rate by integrating over the DM velocity distribution and allowed momentum and energy transfers in the target. The result in this case is instead

$$R = \frac{\sigma_p}{\sum_d A_d m_p}\frac{\rho_\chi}{m_\chi}\int d^3\mathbf{v}_i\, f(\mathbf{v}_i)\int_{\omega_-}^{\omega_+} d\omega \int_{q_-}^{q_+} dq\,\frac{q}{2p_i m_\chi}|\tilde{F}(q)|^2 S(q,\omega) \tag{2.10}$$

where $p_i = m_\chi v$ is the incident DM momentum and $\rho_\chi \sim 0.3\,\mathrm{GeV/cm^3}$ is the local DM energy density. Whereas the WIMP limits were bounds placed by experimental observation, we here instead take zero background to place expected confidence limits through assumed lack of observation. The standard rate in the field used is 3 events/kg-yr to allow for comparison of results, which corresponds to a 95% confidence level for 1 kg-yr of exposure with 0 events observed. This leaves the theoretical work of understanding the phonon response one can expect in a crystal target as being able to compute the rest of the righthand side of (2.10), in particular the structure factor.

2.4 What's Next?

The dynamics of single phonon excitation via scattering of dark matter below masses of 1 MeV has been investigated thoroughly, and is included in Chapter 3 as an example for cubic crystal targets. The nuclear recoil description has also long since been understood, and as previously mentioned has already been probed extensively by WIMP searches. In the intermediate mass regime between the two (MeV $\lesssim m_\chi \lesssim$ GeV) however neither description is correct. There must reasonably be some transition between the two, however, and it is here where the multiphonons shown in Fig. 2.4 enter. If we understand single phonon excitation as the lowest order term in the DM-nucleus interaction at low energies, the multiphonons are the higher-order terms which become more relevant at increasing energy depositions en route to the full nuclear recoil description at high energies. In order to connect the single phonon and nuclear recoil responses to fully flesh out our understanding of the DM interaction with our crystal target, these multiphonon processes must be understood. Moreover, if our detectors do not have the resolution to probe single phonon excitations, then multiphonons will necessarily be the leading signal, even in low-mass ranges where single phonons would otherwise be the dominant scattering process. These reasons motivate the work of this Thesis: we must understand the multiphonon response in order to have a full description of DM scattering in a crystal target. The rest of the Thesis is organized accordingly. Chapter 3 derives the specific mathematical nature of the phonons and structure factor and gives the (known) single phonon results as an example. Chapter 4 then bridges into an analytic description of two-phonon excitation as the next step away from the single phonon. Chapter 5 finally works towards explicitly evaluating the structure factor for n phonons under the incoherent approximation to finish describing the entire multiphonon regime.

2.5 A Phonon Experiment

We conclude this Chapter with a brief discussion of what a planned phonon experiment to directly detect sub-GeV DM would look like as an illustrative example for the theory discussed previously.

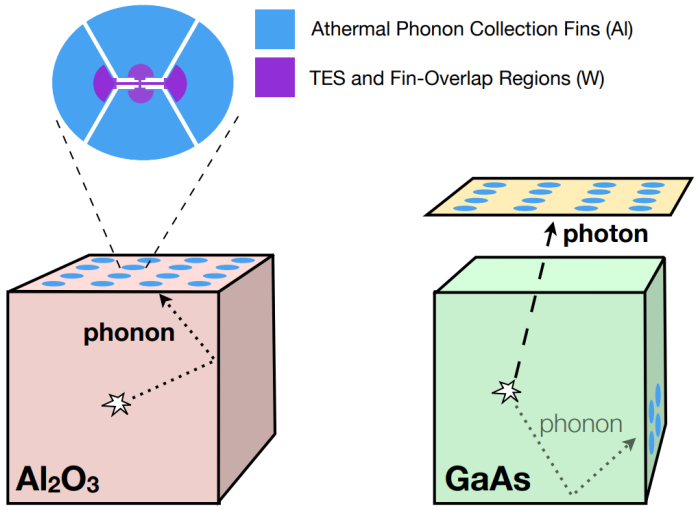

Figure 2.5. Cartoon of two of the relevant detector schemes of the planned SPICE experiment of the TESSERACT project [4]. The experiment will feature many identical copies of these $\sim$few gram size sapphire and GaAs crystals, each totalling around $0.1 - 1$ kg total target mass. The phonons will be measured through athermal phonon detectors. Not shown is the setup for HeRALD, TESSERACT's liquid He phonon experiment.

TESSERACT is a proposed project to push the frontier of the sub-GeV DM search [4]. This project is comprised of two experiments utilizing phonon signals to observe sub-GeV DM; one is HeRALD, a liquid helium experiment, but the other more relevant experiment is SPICE, involving two types of solid crystal targets. These experiments are planned in tandem for their complementarity, but we will focus on SPICE here as it relates to the crystal lattice phonons discussed in this Thesis rather than the phonons and rotons found in liquid Helium.

A schematic of the experimental setup for SPICE is shown in Fig. 2.5. The experiment will feature many identical cm^3-sized crystal targets of sapphire (Al2O3) and gallium arsenide

(GaAs), respectively, each totalling between $0.1 - 1$ kg. Each crystal target will be fitted with an individual cm^2-sized athermal phonon sensor array, either on a silicon substrate (GaAs) or directly on the crystal (sapphire).

The athermal phonon detectors will operate through a two-step process. The superconducting aluminum fins (blue in Fig. 2.5) will first collect the phonons, where their energy will break Cooper pairs and be converted into quasiparticle energy. These quasiparticles will then diffuse into the Transition Edge Sensors (TES, purple in the figure) where their energy will be measured after thermalization. Unlike the TPCs discussed in Sec. 2.1, these will feature no applied electric field as that introduces extra "dark count" backgrounds. The silicon substrate (above the GaAs in the figure) serves as the photodetector for scintillation light, a separate signal from phonons.

The SPICE experiment has a planned 0.1-1 kg-yr exposure for nuclear recoil and electron recoils, respectively; the projected reaches are sensitive to DM masses of 1-10 MeV across the interaction types, and potentially even lower for more optimistic energy resolutions. This will be an exciting foray into the sub-GeV frontier, and is motivated at least in part by the reasons discussed in the prior sections. Knowing that these types of phonon experiments are not only possible, but planned, in turn further motivates us to study the phonon response in these types of crystal targets. We will proceed to do so in more rigorous detail, beginning with a mathematical derivation of phonons in Chapter 3.

Chapter 3

Phonon Phormalism

In this Chapter, we introduce the origin of the structure factor $S(\mathbf{q},\omega)$, which appeared in (2.9) and (2.10), and its connection to the phonon response of the crystal target. We then discuss understanding the structure factor in terms of a *coherent* piece and *incoherent* piece in preparation for deriving our multiphonon expressions in Chapters 4 and 5. We conclude the Chapter by evaluating the structure factor explicitly for single phonon excitation, as discussed previously, with example reach curves for sub-MeV dark matter.

3.1 Dynamic structure factor

Our starting point will be a general potential for spin-independent DM-nucleus interactions, although the formalism below could also be applied to spin-dependent interactions. For a DM particle of mass m_χ incident on a crystal with N unit cells and $\mathfrak{n}$ ions per unit cell, the potential in Fourier space is given by

$$\tilde{\mathscr{V}}(\mathbf{q}) = \frac{2\pi b_p}{\mu_\chi}\tilde{F}(\mathbf{q})\sum_{\ell}^{N}\sum_{d=1}^{\mathfrak{n}} f_{\ell d}\, e^{i\mathbf{q}\cdot\mathbf{r}_{\ell d}}. \tag{3.1}$$

Here, we sum over the N unit cells, labeled by lattice vectors ℓ, and inequivalent atoms within the unit cell, labeled with the index d, such that all atoms in the crystal with positions $\mathbf{r}_{\ell d}$ are summed over. The DM-proton scattering length b_p is defined by the DM-proton scattering cross section $\sigma_p \equiv 4\pi b_p^2$ at some reference momentum, and μ_χ is the DM-proton reduced mass. We

first consider a general coupling strength $f_{\ell d}$ of the nucleus labeled by ℓ, d relative to that of a single proton. $f_{\ell d}$ is specified for various interactions in Section 5.4, such as nucleon number for scalar mediators and the effective electric charge for scattering via a dark photon mediator. In the latter case $f_{\ell d}$ is $\mathbf{q}$ dependent when accounting for screening effects.

We consider two form factors in (3.1) representing limiting cases of interactions: scattering via a heavy mediator, where $\tilde{F}(\mathbf{q}) = 1$; and scattering via a massless mediator, where $\tilde{F}(\mathbf{q}) = q_0^2/q^2$ with a model-dependent reference momentum q_0.

Collecting the overall factor $2\pi b_p \tilde{F}(\mathbf{q})/\mu_\chi$ out front, we arrive at the form shown in (2.9) by inputting this potential into Fermi's golden rule to relate the transition rate of exciting some number of phonons to the scattering cross section. We then *define* the structure factor so that the differential cross section is, as before,

$$\frac{d\sigma}{d^3\mathbf{q}\, d\omega} = \frac{b_p^2}{\mu_\chi^2}\frac{1}{v}|\tilde{F}(\mathbf{q})|^2 S(\mathbf{q},\omega)\,\delta\left(\omega - \omega_{\mathbf{q}}\right) \tag{3.2}$$

where v is the initial velocity of the dark matter (incident on a target at rest), and $\omega_{\mathbf{q}} = \mathbf{q}\cdot\mathbf{v} - q^2/2m_\chi$ is the kinematic constraint on the momentum and energy transfers to the crystal $\mathbf{q}$ and ω. We therefore defined the dynamic structure factor as

$$S(\mathbf{q},\omega) \equiv \frac{1}{N}\sum_f \left| \sum_\ell^N \sum_{d=1}^{\mathrm{n}} \left\langle \Phi_f \middle| f_{\ell d} e^{i\mathbf{q}\cdot\mathbf{r}_{\ell d}} \middle| 0 \right\rangle \right|^2 \delta\left(E_f - \omega\right). \tag{3.3}$$

We assume the system is initially in its ground state $|0\rangle$ prior to the collision, corresponding to a zero temperature system. We sum over final states with energies E_f, such that each term represents the probability to excite the final state $\left|\Phi_f\right\rangle$. Note that this form makes the structure factor's encoding of the material's phonon response manifest.

3.1.1 Coherent and incoherent structure factors

For a given crystal there are many possible configurations of interaction strengths $f_{\ell d}$ which may vary even for different samples of the same material, e.g. the exact distribution of spins or isotopes in the material for spin-dependent[1] or mass-dependent interactions, respectively. This can be accounted for by averaging over a large collection of target samples. With a large number of nuclei in the crystal, we expect the exact distribution of interaction strengths in a given sample to be inconsequential relative to the result averaged over many samples. We can keep track of fluctuations away from the average configuration by splitting the scattering rate into a coherent and incoherent contribution, as explained below.

We follow the procedure of Refs. [40, 41] and first re-express (3.3) by expanding the square and Fourier transforming the δ-function, giving

$$S(\mathbf{q},\omega) = \frac{\Omega_c}{2\pi} \sum_{\ell,\ell'}^{N} \sum_{d,d'}^{\mathrm{n}} f_{\ell d} f^*_{\ell' d'} \mathscr{C}_{\ell' d' \ell d} \tag{3.4}$$

where $\Omega_c = V/N$ is the volume of a unit cell and $\mathscr{C}_{\ell' d' \ell d}$ is the time-dependent two-point function:

$$\begin{aligned} \mathscr{C}_{\ell' d' \ell d} &\equiv \frac{1}{V} \int_{-\infty}^{\infty} dt \sum_f \left\langle 0 \middle| e^{-i\mathbf{q}\cdot\mathbf{r}_{\ell' d'}(0)} \middle| \Phi_f \right\rangle \left\langle \Phi_f \middle| e^{i\mathbf{q}\cdot\mathbf{r}_{\ell d}(t)} \middle| 0 \right\rangle e^{-i\omega t} \\ &\equiv \frac{1}{V} \int_{-\infty}^{\infty} dt \left\langle e^{-i\mathbf{q}\cdot\mathbf{r}_{\ell' d'}(0)} e^{i\mathbf{q}\cdot\mathbf{r}_{\ell d}(t)} \right\rangle e^{-i\omega t}. \end{aligned} \tag{3.5}$$

In the second line we used the completeness of the basis of states. The appearance of the $\Omega_c/2\pi$ prefactor is due differences in normalization conventions, described in more detail in Chapter 5. It will also be advantageous to define a shorthand notation for the *auto-correlation function* for

[1] For spin-dependent interactions, $f_{\ell d}$ is an operator rather than a parameter, but otherwise the analysis proceeds analogously.

an atom with itself as

$$\begin{aligned}\mathscr{C}_{\ell d} &\equiv \mathscr{C}_{\ell d \ell d} \\ &\equiv \frac{1}{V}\int_{-\infty}^{\infty} dt\, \langle e^{-i\mathbf{q}\cdot\mathbf{r}_{\ell d}(0)} e^{i\mathbf{q}\cdot\mathbf{r}_{\ell d}(t)}\rangle e^{-i\omega t}. \end{aligned} \tag{3.6}$$

We assume that the $f_{\ell d}$ are random throughout the crystal, implying that there are no long-range correlations in spin alignment or isotope distribution for example. Under these assumptions, the average of $f_{\ell d} f^*_{\ell' d'}$ over target configurations, $\overline{f_d f^*_{d'}}$, must be independent of the lattice sites ℓ, ℓ'. Making this replacement in (3.4) gives

$$S(\mathbf{q},\omega) = \frac{\Omega_c}{2\pi}\sum_{\ell,\ell'}^{N}\sum_{d,d'}^{\mathfrak{n}} \overline{f_d f^*_{d'}}\,\mathscr{C}_{\ell' d' \ell d} \tag{3.7}$$

where the averages may be written as

$$\begin{aligned} d \neq d' &: \qquad \overline{f_d f^*_{d'}} = \overline{f_d}\,\overline{f^*_{d'}}, \\ d = d' &: \qquad \overline{f_d f^*_{d'}} = \overline{f_d^2}. \end{aligned}$$

For the $d \neq d'$ case we assumed that the expectation values of the f_d for different atoms in the unit cell are uncorrelated. This allows one to split the structure factor into two contributions:

$$S(\mathbf{q},\omega) = \frac{\Omega_c}{2\pi}\sum_{\ell\neq\ell'}^{N}\sum_{d\neq d'}^{\mathfrak{n}} \overline{f_d}\,\overline{f^*_{d'}}\,\mathscr{C}_{\ell' d' \ell d} + \frac{\Omega_c}{2\pi}\sum_{\ell}^{N}\sum_{d}^{\mathfrak{n}} \overline{f_d^2}\,\mathscr{C}_{\ell d} \tag{3.8}$$

$$= \frac{\Omega_c}{2\pi}\sum_{\ell,\ell'}^{N}\sum_{d,d'}^{\mathfrak{n}} \overline{f_d}\,\overline{f^*_{d'}}\,\mathscr{C}_{\ell' d' \ell d} + \frac{\Omega_c}{2\pi}\sum_{\ell}^{N}\sum_{d}^{\mathfrak{n}} \left(\overline{f_d^2} - (\overline{f_d})^2\right)\mathscr{C}_{\ell d} \tag{3.9}$$

$$\equiv S^{(\mathrm{coh})}(\mathbf{q},\omega) + S^{(\mathrm{inc})}(\mathbf{q},\omega) \tag{3.10}$$

where the second line is obtained by adding and subtracting the term proportional to $(\overline{f_d})^2$ and regrouping. The first and second term in (3.10) are usually referred to as the *coherent* and

incoherent structure factors in the neutron scattering literature.

The coherent structure factor relays the scattering rate if the interaction strengths of all atoms in equivalent lattice sites are equal to a common value $\overline{f_d}$. For example, one can consider low energy, spin-independent neutron scattering in a very pure crystal with only a single isotope. This implies $\overline{f_d} = \overline{f_{\ell d}} = A_d$, with A_d the atomic mass number, such that the incoherent contribution in (3.10) vanishes exactly. The sum in (3.9) then crucially includes position correlators between differing nuclei, which capture the interference between different lattice sites. In practice, this interference leads to a coherence condition, which demands that the momentum in the scattering process must be conserved up to a reciprocal lattice vector. In particular, the 0th order term in a low $\mathbf{q}$ expansion of (3.5) corresponds to Bragg diffraction.

The incoherent structure factor on the other hand accounts for the statistical variations in interaction strengths between different scattering centers in the lattice. The second sum in (3.9) contains no cross terms and thus does not include interference between different lattice sites. There is therefore no corresponding coherence condition and the incoherent structure does not enforce momentum conservation.[2] For most earlier DM direct detection calculations the focus has been on spin-independent scattering in high purity crystals where $\overline{f_d^2} - (\overline{f_d})^2 = 0$, implying that only the coherent scattering contributes. This is the scenario we first focus on in Chapter 3. The coherent structure factors are however more difficult to evaluate, due to the conservation of crystal momentum that is built into (3.5). This results in increasingly complicated phase space integrals for multiphonon processes [42]. We address this in Chapter 5, wherein the utility of studying the incoherent structure factor will be that the auto-correlation function can be used to obtain a reasonable and more manageable approximation of the coherent structure factor at sufficiently high momenta.

Before venturing further into this approximation and its validity, we must first develop

[2] An alternative but equivalent point of view is that for coherent scattering, translation symmetry is broken up to a shift symmetry, since all unit cells are identical. For incoherent scattering the scattering centers are treated as independent and translation invariance is therefore fully broken, resulting in the complete loss of momentum conservation.

the structure factors into a form which lends itself to a direct calculation. In order to evaluate the structure factors in (3.3)–(3.7), the position vector of each atom may be decomposed in terms of the equilibrium lattice positions and displacement vectors, $\mathbf{r}_{\ell d} = \ell + \mathbf{r}_d^0 + \mathbf{u}_{\ell d}$. Here $\mathbf{r}_d^0$ is the equilibrium location of atom d relative to the origin of the primitive cell and $\mathbf{u}_{\ell d}$ is the displacement relative to that equilibrium. Following this decomposition, we quantize the displacement vector in the harmonic approximation with a phonon mode expansion

$$\mathbf{u}_{\ell d}(t) = \sum_{\nu}^{3\mathfrak{n}} \sum_{\mathbf{k}} \frac{1}{\sqrt{2Nm_d\omega_{\nu,\mathbf{k}}}} \Big(\mathbf{e}_{\nu,d,\mathbf{k}} \hat{a}_{\nu,\mathbf{k}} e^{i\mathbf{k}\cdot(\ell+\mathbf{r}_d^0) - i\omega_{\nu,\mathbf{k}}t} + \mathbf{e}^*_{\nu,d,\mathbf{k}} \hat{a}^\dagger_{\nu,\mathbf{k}} e^{-i\mathbf{k}\cdot(\ell+\mathbf{r}_d^0) + i\omega_{\nu,\mathbf{k}}t} \Big) \tag{3.11}$$

The index ν denotes the phonon branches, of which there are $3\mathfrak{n}$, and $\mathbf{k}$ labels the phonon momentum in the first Brillouin Zone (BZ). The $\hat{a}^\dagger_{\nu,\mathbf{k}}$ and $\hat{a}_{\nu,\mathbf{k}}$ are the creation and annihilation operators for the phonons, $\omega_{\nu,\mathbf{k}}$ is the energy of the phonon, $\mathbf{e}_{\nu,d,\mathbf{k}}$ is the phonon eigenvector for atom d normalized within a unit cell, $\sum_d \mathbf{e}^*_{\nu,d,\mathbf{k}} \cdot \mathbf{e}_{\mu,d,\mathbf{k}'} = \delta_{\mu\nu}\delta_{\mathbf{k},\mathbf{k}'}$, and m_d is the mass of atom d.

The structure factor in (3.7) can then be explicitly evaluated by applying (3.11) to (3.5). For a pure crystal with $\overline{f_d^2} = (\overline{f_d})^2$, this is given by [42]

$$S^{(\mathrm{coh})}(\mathbf{q},\omega) = \frac{1}{N} \sum_f \left| \sum_{\ell}^{N} \sum_{d}^{\mathfrak{n}} \overline{f_d}\, e^{-W_d(\mathbf{q})} \mathscr{M}_{\ell d} \right|^2 \delta\left(E_f - \omega\right) \tag{3.12}$$

where

$$\mathscr{M}_{\ell d} \equiv e^{i\mathbf{q}\cdot(\ell+\mathbf{r}_d^0)} \left\langle \Phi_f \right| \exp\left[i \sum_{\mathbf{k},\nu} \frac{\mathbf{q}\cdot\mathbf{e}^*_{\nu,\mathbf{k},d}}{\sqrt{2Nm_d\omega_{\nu,\mathbf{k}}}} \hat{a}^\dagger_{\nu,\mathbf{k}} e^{-i\mathbf{k}\cdot(\ell+\mathbf{r}_d^0)} \right] |0\rangle \tag{3.13}$$

is the matrix element for scattering into the final state of the crystal denoted by f. The Debye-Waller factor $e^{-W_d(\mathbf{q})}$ is given in terms of the function $W_d(\mathbf{q}) \equiv \frac{1}{2}\langle (\mathbf{q}\cdot\mathbf{u}_{\ell d}(0))^2 \rangle$. We may Taylor expand the inner exponential in powers of $\mathbf{q}$ where the nth term can excite a final state consisting of n phonons. The phonon eigenvectors and energies may be obtained numerically using Density Functional Theory (DFT) (see e.g. [43]); using these, the leading single phonon structure factor

has been calculated [44, 45, 46]. These DFT-based calculations quickly become cumbersome, however, and have not yet been performed for generic n-phonon terms. Analytic calculations may be performed more easily, and have been carried out for the single- and two-phonon terms [42], but are only tractable when assuming an isotropic crystal and that $|\mathbf{q}|$ is small relative to the size of the first Brillouin zone. Such analytic calculations likewise lack scalability for higher order phonon terms.

3.2 Illustrative Example: Analytic Single Phonon

For the final state consisting of a single phonon with polarization ν and momentum $\mathbf{k}$, the leading result for the matrix element is

$$\mathscr{M}_{f,\mathbf{q},d}^{(1-ph)} = \sum_{\mathbf{G}} \delta_{\mathbf{G},\mathbf{q}-\mathbf{k}} \frac{i\sqrt{N}\mathbf{q}\cdot\mathbf{e}_{\nu,d,\mathbf{q}}^{*}}{\sqrt{2m_d\omega_{\nu,\mathbf{q}}}} e^{i(\mathbf{q}-\mathbf{k})\cdot\mathbf{r}_d^0} , \tag{3.14}$$

where $\mathbf{G}$ are the reciprocal lattice vectors, which satisfy $\sum_\ell e^{i\ell\cdot(\mathbf{q}-\mathbf{k})} = N\sum_{\mathbf{G}}\delta_{\mathbf{G},\mathbf{q}-\mathbf{k}}$, with the Kronecker-$\delta$ enforcing momentum conservation in the crystal. Here we also used that phonon observables such as $\omega_{\nu,\mathbf{q}}$ are invariant under $\mathbf{q}\to\mathbf{q}+\mathbf{G}$. While there can be anharmonic corrections to the above matrix element, they are negligible in the low q limit.

Summing over all possible single-phonon final states, this gives a structure factor identical to the result in Ref. [44]. For sub-MeV DM scattering, where q is typically well within the first Brillouin zone, it is a good approximation to neglect the sum over $\mathbf{G}$ as well as the Debye-Waller factors. Then the result simplifies to

$$S^{(1-ph)}(\mathbf{q},\omega) = \sum_{\nu}\frac{1}{2\omega_{\nu,\mathbf{q}}}\left|\sum_{d}^{\mathfrak{n}}\frac{A_d}{\sqrt{m_d}}\mathbf{q}\cdot\mathbf{e}_{\nu,d,\mathbf{q}}^{*}\right|^2\delta(\omega-\omega_{\nu,\mathbf{q}})\,. \tag{3.15}$$

In the long wavelength (low q) limit, we can moreover approximate the acoustic modes as having real eigenvectors with magnitudes

$$\mathbf{e}_{\mathrm{LA},\mathbf{k},d} \approx \frac{\sqrt{A_d}}{\sqrt{\sum_{d'} A_{d'}}} \hat{\mathbf{k}}; \tag{3.16}$$

note that this form is valid for generic crystal targets and not limited to GaAs. For the LO phonon, we use the following eigenvectors, which are only valid for diatomic lattices [42]

$$\mathbf{e}_{\mathrm{LO},\mathbf{k},1} \approx \frac{\sqrt{A_2}}{\sqrt{A_1 + A_2}} \hat{\mathbf{k}}, \tag{3.17}$$

$$\mathbf{e}_{\mathrm{LO},\mathbf{k},2} \approx -\frac{\sqrt{A_1}}{\sqrt{A_1 + A_2}} e^{-i\mathbf{k}\cdot\mathbf{r}_2^0} \hat{\mathbf{k}} \tag{3.18}$$

where the first atom is taken to be at the origin of the primitive cell, and the second atom is taken to be at the coordinate $\mathbf{r}_2^0 = (a/4, a/4, a/4)$ for GaAs. The acoustic and optical transverse eigenvectors are orthogonal to these, but do not contribute to the scattering into a single phonon.

As can be seen from (3.14), transverse polarizations cannot contribute to the single phonon rate. With these approximations, the analytic expressions for the single phonon contributions to the structure factor are [42]

$$S_{n=1,\mathrm{LA}}(q,\omega) \approx \frac{\left(\sum_{d'} A_{d'}\right) q^2}{2 m_p \omega_{\mathrm{LA},q}} \delta(\omega - \omega_{\mathrm{LA},q}) \Theta(\omega_{\mathrm{LO}} - \omega) \tag{3.19}$$

$$S_{n=1,\mathrm{LO}}(q,\omega) \approx \frac{q^4 a^2}{32 \omega_{\mathrm{LO}}} \frac{A_1 A_2}{m_p (A_1 + A_2)} \delta(\omega - \omega_{\mathrm{LO}}) \tag{3.20}$$

Here we have introduced a cut-off of $\omega = \omega_{\mathrm{LO}}$ to the longitudinal acoustic branch to avoid overestimating the scattering rate with the LA mode near the edge of the Brillouin zone. The q^4 scaling and appearance of the lattice constant a in the optical structure factor comes from averaging over angles with the eigenvectors, giving $(\mathbf{q}\cdot\mathbf{r}_2^0)^2 \approx q^2 a^2/16$ [47]. As an example, projected reaches using these analytic single phonon structure factors in GaAs are shown in Fig. 3.1.

In this figure, we assume 3 events with 1 kg-yr of exposure. The massless mediator limit is taken (as discussed previously, letting $F(q) = (m_\chi v_0/q)^4$ in (2.9)). The massless mediator's

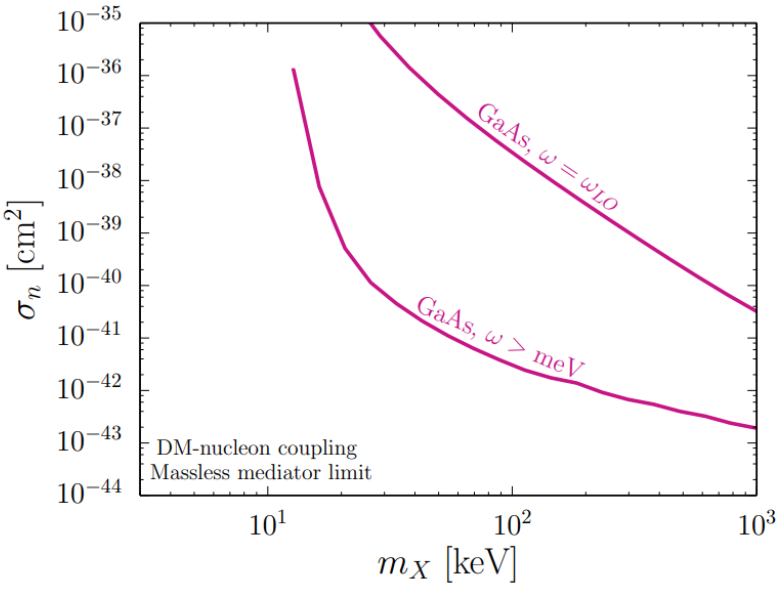

Figure 3.1. Example cross section limits for an exposure of 1 kg-year in a GaAs crystal target in the massless mediator limit [5]. The (lower) acoustic phonon line assumes a threshold of 1 meV, while the (upper) optical phonon line assumes only a threshold sufficient to see the optical phonon, $\omega_{\rm LO} \approx 33$ meV.

scaling in q implies favoring smaller momenta transfer, however nevertheless around $m_\chi \sim 1$ MeV sufficiently large momenta outside of the first BZ are kinematically available and the single phonon approximations begin breaking down. In order to investigate what happens at larger energy and momentum transfers, we must now move beyond this example toward deriving the full multiphonon response of the crystal.

Acknowledgements

This chapter, in part, is a reprint of the material as it appears in Brian Campbell-Deem, Peter Cox, Tom Melia, Simon Knapen, Tongyan Lin, Multiphonon excitations from dark matter scattering in crystals, Phys.Rev. D 101 (2020) no.3, 036006, the Erratum: Phys.Rev. D 102 (2020) no.1, 019904, and Brian Campbell-Deem, Simon Knapen, Tongyan Lin, and Ethan Villarama, Dark matter direct detection from the single phonon to the nuclear recoil regime, Phys.Rev. D **106** (2022) no.6, 036019. The dissertation author was one of the primary investigators and authors of these papers.

Chapter 4

Toward Two Phonons

4.1 Introduction

In this Chapter, we begin our pursuit of understanding multiphonon excitations by computing analytic results for processes involving two phonons in the final state, also referred to as diphonon excitations. We perform these calculations of the structure factors and rates for cubic crystals such as Ge, Si, GaAs and diamond in the isotropic approximation. We also make use of the long-wavelength (low q) approximation, which allows us to characterize the anharmonicity of the crystal through an interaction Hamiltonian. There are therefore two processes which contribute to the total scattering into two phonons, which are depicted in Fig. 4.1: the *contact* interaction, in which two phonons are directly excited; and the *anharmonic interaction*, which involves an off-shell phonon mediator. We focus primarily on two acoustic phonons in the final state, for which there is a well-known effective theory, and briefly comment on diphonon

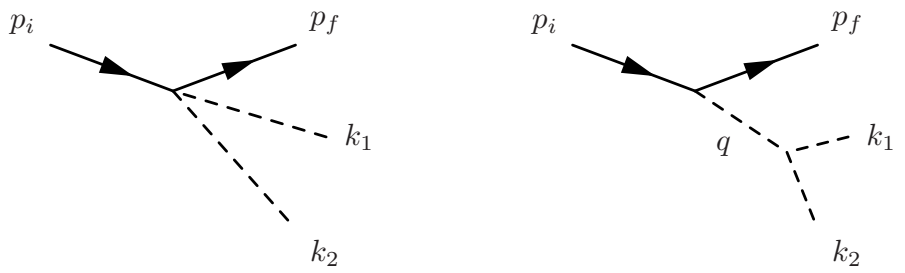

Figure 4.1. Diagrams representing the contact (left) and anharmonic (right) contributions to the DM scattering rate into two phonons (dashed lines).

excitations involving optical phonons. Due to the breakdown of the anharmonic interaction Hamiltonian beyond the first BZ, as well as our use of a linear extrapolation of the acoustic dispersions, we limit the results to sub-MeV dark matter masses. A discussion of phonon excitation for 3 or more phonons, as well as phonon excitation beyond $m_\chi > 1$ MeV, is instead discussed in the following Chapter.

The main object we are computing is the structure factor $S(q,\omega)$, which receives contributions from each of the processes depicted in Fig. 4.1. The contact term more precisely arises from expanding the exponential in (3.13) to second order, while the anharmonic phonon interactions in the material give rise to the anharmonic term. We define δH as the leading order anharmonic phonon interaction Hamiltonian; its precise definition we defer to Sec. 4.2.1. At leading order, the 2-phonon matrix element is then

$$\mathscr{M}^{(2\text{-}ph)}_{f,\mathbf{q},d} = \mathscr{M}^{(cont)}_{f,\mathbf{q},d} + \mathscr{M}^{(anh)}_{f,\mathbf{q},d}\,, \tag{4.1}$$

with

$$\begin{aligned}
\mathscr{M}^{(cont)}_{f,\mathbf{q},d} &= \sum_\ell -\frac{1}{2}\Big\langle \nu_1,\mathbf{k}_1;\nu_2,\mathbf{k}_2\Big|\left[\sum_{\nu,\mathbf{k}}\frac{\mathbf{q}\cdot\mathbf{e}^*_{\nu,d,\mathbf{k}}}{\sqrt{2Nm_d\omega_{\nu,\mathbf{k}}}}\hat{a}^\dagger_{\nu,\mathbf{k}}e^{-i\mathbf{k}\cdot(\ell+\mathbf{r}^0_d)}\right]^2\Big|0\Big\rangle\, e^{i\mathbf{q}\cdot(\ell+\mathbf{r}^0_d)} \\
&= s_{1,2}\sum_{\mathbf{G}} -\frac{(\mathbf{q}\cdot\mathbf{e}^*_{\nu_1,d,\mathbf{k}_1})(\mathbf{q}\cdot\mathbf{e}^*_{\nu_2,d,\mathbf{k}_2})}{2m_d\sqrt{\omega_{\nu_1,\mathbf{k}_1}\omega_{\nu_2,\mathbf{k}_2}}}e^{i(\mathbf{q}-\mathbf{k}_1-\mathbf{k}_2)\cdot\mathbf{r}^0_d}\,\delta_{\mathbf{G},\mathbf{q}-\mathbf{k}_1-\mathbf{k}_2}\,, \qquad (4.2)\\
\mathscr{M}^{(anh)}_{f,\mathbf{q},d} &= i\sum_{\mathbf{G},\mathbf{k},\nu}\sqrt{\frac{N}{2m_d\omega_{\nu,\mathbf{k}}}}\left(\frac{\mathbf{q}\cdot\mathbf{e}^*_{\nu,d,\mathbf{k}}\langle\nu_1,\mathbf{k}_1;\nu_2,\mathbf{k}_2|\delta H|\nu,\mathbf{k}\rangle}{\omega_{\nu_1,\mathbf{k}_1}+\omega_{\nu_2,\mathbf{k}_2}-\omega_{\nu,\mathbf{k}}+i\Gamma_{\nu,\mathbf{k}}/2}\,e^{i(\mathbf{q}-\mathbf{k})\cdot\mathbf{r}^0_d}\,\delta_{\mathbf{G},\mathbf{q}-\mathbf{k}}\right. \\
&\quad\left.+\frac{\mathbf{q}\cdot\mathbf{e}_{\nu,d,\mathbf{k}}\langle\nu,\mathbf{k};\nu_1,\mathbf{k}_1;\nu_2,\mathbf{k}_2|\delta H|0\rangle}{-(\omega_{\nu_1,\mathbf{k}_1}+\omega_{\nu_2,\mathbf{k}_2})-\omega_{\nu,\mathbf{k}}+i\Gamma_{\nu,\mathbf{k}}/2}\,e^{i(\mathbf{q}+\mathbf{k})\cdot\mathbf{r}^0_d}\,\delta_{\mathbf{G},\mathbf{q}+\mathbf{k}}\right), \qquad (4.3)
\end{aligned}$$

where the factor $s_{1,2}\equiv(\delta_{\nu_1,\nu_2}\delta_{\mathbf{k}_1,\mathbf{k}_2}+1)^{-1/2}$ accounts for Bose statistics. We refer to the contributions in (4.2) and (4.3) as the *contact term* and the *anharmonic term*, respectively. Anharmonic phonon interactions also lead to a non-zero phonon width, $\Gamma_{\nu,\mathbf{k}}$. This has been resummed in the phonon propagator in (4.3) and becomes relevant when the intermediate

phonon goes on-shell. Details regarding the derivation of the above matrix elements are given in Appendix 4.A.

In the long wavelength limit, we can again consider only the $\mathbf{G} = 0$ contribution to the matrix elements and drop the Debye-Waller factors. It will then be convenient to express the three-phonon matrix element as

$$\langle \nu_1, \mathbf{k}_1; \nu_2, \mathbf{k}_2 | \delta H | \nu, \mathbf{q} \rangle = \frac{V}{(2(\sum_d m_d)N)^{3/2}} \frac{\widetilde{\mathscr{M}}(\mathbf{q}, \mathbf{k}_i, \nu_i)}{\sqrt{\omega_{\nu,\mathbf{q}} \omega_{\nu_1,\mathbf{k}_1} \omega_{\nu_2,\mathbf{k}_2}}} \delta_{\mathbf{q},\mathbf{k}_1+\mathbf{k}_2} \,, \tag{4.4}$$

As we show in Sec. 4.2.1, in the long wavelength limit $\widetilde{\mathscr{M}}(\mathbf{q}, \mathbf{k}_i, \nu_i)$ is a function only of the momenta, long-wavelength polarization tensors and elastic constants of the material. In addition, eigenvectors are real in this limit, such that the matrix element $\widetilde{\mathscr{M}}(\mathbf{q}, \mathbf{k}_i, \nu_i)$ is real as well. The two terms in (4.1) therefore do not interfere to leading order in the small q expansion, when neglecting terms higher order in $\Gamma_{\nu,\mathbf{k}}$. Using the long-wavelength polarization vectors defined in (3.16), the two-phonon structure factor can be simplified to

$$S(\mathbf{q}, \omega) = S^{(cont)}(\mathbf{q}, \omega) + S^{(anh)}(\mathbf{q}, \omega) \,, \tag{4.5}$$

$$\begin{aligned} S^{(cont)}(\mathbf{q}, \omega) = \frac{1}{8} \frac{\sum_d A_d}{m_p \rho} \sum_{\nu_1,\nu_2} \int \frac{d^3\mathbf{k}_1}{(2\pi)^3} \frac{\left| (\mathbf{q} \cdot \mathbf{e}_{\nu_1,\mathbf{k}_1})(\mathbf{q} \cdot \mathbf{e}_{\nu_2,\mathbf{q}-\mathbf{k}_1}) \right|^2}{\omega_{\nu_1,\mathbf{k}_1} \omega_{\nu_2,\mathbf{q}-\mathbf{k}_1}} \\ \times \delta(\omega - \omega_{\nu_1,\mathbf{k}_1} - \omega_{\nu_2,\mathbf{q}-\mathbf{k}_1}) \,, \end{aligned} \tag{4.6}$$

$$\begin{aligned} S^{(anh)}(\mathbf{q}, \omega) = \frac{1}{16} \frac{\sum_d A_d}{m_p \rho^3} \sum_{\nu_1,\nu_2} \int \frac{d^3\mathbf{k}_1}{(2\pi)^3} \left| \frac{q \widetilde{\mathscr{M}}(\mathbf{q}, \mathbf{k}_i, \nu_i)}{\omega_{LA,\mathbf{q}} \sqrt{\omega_{\nu_1,\mathbf{k}_1} \omega_{\nu_2,\mathbf{q}-\mathbf{k}_1}}} \left(\frac{1}{\omega - \omega_{LA,\mathbf{q}} + i\Gamma_{LA,\mathbf{q}}/2} \right. \right. \\ \left. \left. + \frac{1}{-\omega - \omega_{LA,\mathbf{q}} + i\Gamma_{LA,\mathbf{q}}/2} \right) \right|^2 \delta(\omega - \omega_{\nu_1,\mathbf{k}_1} - \omega_{\nu_2,\mathbf{q}-\mathbf{k}_1}) \,, \end{aligned} \tag{4.7}$$

where we took the continuum limit by substituting $\sum_{\mathbf{k}_1} \to V \int \frac{d^3\mathbf{k}_1}{(2\pi)^3}$. $\rho = N m_p \sum_d A_d / V$ is the mass density of the material. Similar to the single-phonon structure factor, the overall factor of $\sum_d A_d$ will drop out in the expression of the rate per unit target mass, so that the rate to excite two phonons depends only on bulk properties such as sound speeds, density, and elastic constants.

While the anharmonic interaction only relies on the DM coupling to a single phonon, and therefore appears to be lower order in the expansion parameter $q/\sqrt{m_N\omega}$, there is an additional suppression in q from the insertion of the phonon self-interaction. We will see in Sec. 4.2 that in the low-momentum regime, the self-interactions of acoustic phonons are governed by multiple dimensionful parameters that are related to the elastic constants of the crystal. The sense in which the self-interactions are "small" can be most easily seen from the fact that the typical width of the longitudinal acoustic phonon, Γ, is very small compared to its energy,[1] in other words $\Gamma/\omega \ll 1$.

Following this observation, it is instructive to consider the leading order scaling in q for each of these processes. This allows for a qualitative comparison between different channels and materials before getting into the precise details of evaluating the structure factors. The resulting scaling is represented schematically in Table 4.1. For a single acoustic mode in the final state, $S(q,\omega)$ scales linearly with q but requires a very low threshold. For the single optical mode[3] and the two-phonon processes, $S(q,\omega)$ scales as $\sim q^4$. Finally, it is interesting to compare crystals with superfluid helium, where the diphonon rate also scales as $\sim q^4$ (as discussed further in Sec. 4.4.2).

[1]Note this is different from superfluid He, where the phonon-roton self-interactions are much larger, but where the phonon decay is kinematically forbidden for part of the dispersion curve.

[3]The single optical mode scales as q^4 for dark matter that couples proportional to mass [47], which is the situation considered here; otherwise, it scales as q^2.

Table 4.1. Leading scaling of the structure factor $S(q,\omega)$ in the low q (low m_{DM}) limit for different channels, and required approximate thresholds to observe them. It is assumed that the DM couples proportional to the mass of the atoms. The # indicates that this channel vanishes in the limit where the (material dependent) phonon self-couplings are taken to zero.

channel	low-q scaling	typical threshold needed	Ref.
single acoustic phonon	q	1 meV	[48, 44, 49]
single optical phonon	q^4	25 meV	[48, 44, 49, 47]
two-phonon (contact)	q^4	5-10 meV	this work
two-phonon (anharmonic)	$\#q^4$	5-10 meV	this work
two-phonon (helium)	$\#q^4$	1 meV[2]	[50, 51, 52, 53]

4.2 Evaluation of the structure factor

In this section we provide explicit results and analytic formulae for the two contributions to the two-phonon structure factor, Eqs. (4.6)-(4.7). Even in the long-wavelength limit, the dispersions and anharmonic couplings are in general direction-dependent, substantially complicating the calculations. For cubic crystals, the isotropic limit is however known to be in excellent agreement with the general result for scattering to single phonons [44]. In this Chapter we will therefore restrict ourselves to cubic crystals such as GaAs, Ge, Si and diamond, and approximate them as isotropic. We leave a fully general calculation of the multiphonon rate with Density Functional Theory (DFT) for future work, but we do not expect that accounting for anisotropy would qualitatively change our conclusions.

For the diphonon contribution, a description of the phonon self-interactions is needed, and this is where the isotropic approximation is most advantageous: as we will see in Sec. 4.2.1, the effective Hamiltonian is relatively simple in the isotropic and long-wavelength limit, containing 5 independent operators (this number grows to 9 if instead cubic symmetry is assumed). The coefficients of these operators can moreover be extracted from the elastic properties of the material. Each coefficient maps directly to a linear combination of the second order elastic constants (related to the bulk modulus and Young's modulus) and third order elastic constants; these quantities can either be measured or computed with *ab initio* methods.

4.2.1 Anharmonic term

To compute the anharmonic contribution, we use a low-momentum effective description of the phonon self-interactions. As for any effective theory, we first constrain the form of the Hamiltonian using the symmetries of the theory and subsequently fix the Wilson coefficients from measured observables, or by matching on to the full UV theory. It is hereby convenient to introduce a "long-wavelength displacement operator", in analogy to the long wavelength polarization tensors defined in (3.16). Replacing the polarization tensors with their long-wavelength

versions and averaging over the atoms in a unit cell, we can define

$$\mathbf{u}(\mathbf{r}) \equiv \sum_{\nu}^{3} \sum_{\mathbf{k}} \sqrt{\frac{1}{2N(\sum_d m_d)\omega_{\nu,\mathbf{k}}}} \left(\mathbf{e}_{\nu,\mathbf{k}} \hat{a}_{\nu,\mathbf{k}} e^{i\mathbf{k}\cdot\mathbf{r}} + \mathbf{e}^{*}_{\nu,\mathbf{k}} \hat{a}^{\dagger}_{\nu,\mathbf{k}} e^{-i\mathbf{k}\cdot\mathbf{r}} \right) , \tag{4.8}$$

where now we only sum over acoustic polarizations ν and we have replaced the individual atomic position vectors $\ell + \mathbf{r}^0_d$ with the continuous position vector $\mathbf{r}$. Once again, the long-wavelength displacement operators $\mathbf{u}$ can be distinguished from their more general counterparts $\mathbf{u}_{\ell,d}$ by the index labels.

Assuming isotropy, there are only 5 independent operators to third order in the effective Hamiltonian [54, 55]:

$$\delta H = \int d^3\mathbf{r} \, \frac{1}{2}(\beta+\lambda) u_{ii} u_{jk} u_{jk} + (\gamma+\mu) u_{ij} u_{ki} u_{kj} + \frac{\alpha}{3!} u_{ii} u_{jj} u_{kk} + \frac{\beta}{2} u_{ii} u_{jk} u_{kj} + \frac{\gamma}{3} u_{ij} u_{jk} u_{ki} \, , \tag{4.9}$$

with $u_{ij} \equiv \partial_i u_j$ and the i, j running over the three spatial coordinates. Repeated indices are summed over. The coefficients $\alpha, \beta, \gamma, \lambda$ and μ can be determined from the measured or calculated elastic constants of the crystal. In particular, the parameters μ and λ are the Lamé parameters of the crystal and related to the bulk and Young's moduli. The parameters α, β and γ can be calculated from the third order elastic constants, as described in Appendix 4.B. All five parameters have units of pressure and are reported in units of Giga-Pascal (GPa) in Tab. 4.2 for the crystals we consider.

Using (4.8)-(4.9), the anharmonic three-phonon matrix element can be written in the

form of (4.4), where the function $\widetilde{\mathscr{M}}$ is given by:

$$\begin{aligned}
\widetilde{\mathscr{M}} &= (\beta+\lambda)\Big[(\mathbf{q}\cdot\mathbf{e})(\mathbf{k}_1\cdot\mathbf{k}_2)(\mathbf{e}_1\cdot\mathbf{e}_2)+(\mathbf{k}_1\cdot\mathbf{e}_1)(\mathbf{q}\cdot\mathbf{k}_2)(\mathbf{e}\cdot\mathbf{e}_2)+(\mathbf{k}_2\cdot\mathbf{e}_2)(\mathbf{k}_1\cdot\mathbf{q})(\mathbf{e}_1\cdot\mathbf{e})\Big] \\
&\quad+(\gamma+\mu)\Big[(\mathbf{q}\cdot\mathbf{k}_1)\big[(\mathbf{k}_2\cdot\mathbf{e}_1)(\mathbf{e}_2\cdot\mathbf{e})+(\mathbf{k}_2\cdot\mathbf{e})(\mathbf{e}_2\cdot\mathbf{e}_1)\big] \\
&\qquad+(\mathbf{k}_2\cdot\mathbf{k}_1)\big[(\mathbf{q}\cdot\mathbf{e}_1)(\mathbf{e}_2\cdot\mathbf{e})+(\mathbf{q}\cdot\mathbf{e}_2)(\mathbf{e}\cdot\mathbf{e}_1)\big] \\
&\qquad+(\mathbf{q}\cdot\mathbf{k}_2)\big[(\mathbf{k}_1\cdot\mathbf{e}_2)(\mathbf{e}_1\cdot\mathbf{e})+(\mathbf{k}_1\cdot\mathbf{e})(\mathbf{e}_1\cdot\mathbf{e}_2)\big]\Big] \\
&\quad+\alpha(\mathbf{q}\cdot\mathbf{e})(\mathbf{k}_1\cdot\mathbf{e}_1)(\mathbf{k}_2\cdot\mathbf{e}_2) \\
&\quad+\beta\Big[(\mathbf{k}_1\cdot\mathbf{e}_1)(\mathbf{q}\cdot\mathbf{e}_2)(\mathbf{k}_2\cdot\mathbf{e})+(\mathbf{q}\cdot\mathbf{e})(\mathbf{k}_1\cdot\mathbf{e}_2)(\mathbf{k}_2\cdot\mathbf{e}_1)+(\mathbf{k}_2\cdot\mathbf{e}_2)(\mathbf{q}\cdot\mathbf{e}_1)(\mathbf{k}_1\cdot\mathbf{e})\Big] \\
&\quad+\gamma\Big[(\mathbf{q}\cdot\mathbf{e}_1)(\mathbf{k}_1\cdot\mathbf{e}_2)(\mathbf{k}_2\cdot\mathbf{e})+(\mathbf{q}\cdot\mathbf{e}_2)(\mathbf{k}_1\cdot\mathbf{e})(\mathbf{k}_2\cdot\mathbf{e}_1)\Big], \qquad (4.10)
\end{aligned}$$

and we introduced the shorthand notation $\mathbf{e}=\mathbf{e}_{\nu,\mathbf{q}}$, $\mathbf{e}_1=\mathbf{e}_{\nu_1,\mathbf{k}_1}$ etc. From (4.3) it follows that only the longitudinal polarization of the off-shell, intermediate phonon contributes. Depending on the polarizations of the outgoing phonons, different terms in (4.10) contribute. Concretely, there are four distinct combinations for which the matrix element is non-zero:

- LA-LA
- TA-TA with both phonons polarized in the plane spanned by the momenta
- TA-TA with both phonons polarized orthogonal to the plane spanned by the momenta
- LA-TA with the TA phonon polarized in the plane spanned by the momenta.

In the isotropic limit, the structure factor in (4.7) reduces to

$$\begin{aligned}
S^{(anh)}(q,\omega) &= \frac{1}{4}\frac{\sum_d A_d\, q^2}{\rho^3 m_p[(\omega^2-(c_{LA}q)^2)^2+(c_{LA}q)^2\Gamma^2_{LA,q}]} \\
&\quad\times\sum_{\nu_1,\nu_2}\int\frac{d^3\mathbf{k}_1}{(2\pi)^3}\,\frac{|\widetilde{\mathscr{M}}|^2}{c_{\nu_1}c_{\nu_2}k_1|\mathbf{q}-\mathbf{k}_1|}\,\delta(\omega-k_1c_{\nu_1}-|\mathbf{q}-\mathbf{k}_1|c_{\nu_2})\,. \qquad (4.11)
\end{aligned}$$

The anharmonic matrix element given in (4.10) can also be used to compute $\Gamma_{LA,q}$, which we provide explicitly in Appendix 4.C.1.

The phase space integrals above can be evaluated analytically. Given that the different polarizations in the final states do not interfere, we can separately evaluate all four channels:

$$S^{(anh)}_{LALA}(q,\omega) = \frac{\left(\sum_d A_d\, q^4\, \omega^4\right)\left(g^{(anh)}_{LALA}\left(\frac{qc_{LA}}{\omega}\right)\right)}{16\pi^2 c_{LA}^7 m_p \rho^3 [(\omega^2-(c_{LA}q)^2)^2+(c_{LA}q)^2\Gamma^2_{LA,q}]}\,\theta(\omega-c_{LA}q)\,, \tag{4.12}$$

$$S^{(anh)}_{TATAout}(q,\omega) = \frac{\left(\sum_d A_d\, q^4\, \omega^4\right)\left(g^{(anh)}_{TATAout}\left(\frac{qc_{TA}}{\omega}\right)\right)}{16\pi^2 c_{TA}^7 m_p \rho^3 [(\omega^2-(c_{LA}q)^2)^2+(c_{LA}q)^2\Gamma^2_{LA,q}]}\,\theta(\omega-c_{TA}q)\,, \tag{4.13}$$

$$S^{(anh)}_{TATAin}(q,\omega) = \frac{\left(\sum_d A_d\, q^4\, \omega^4\right)\left(g^{(anh)}_{TATAin}\left(\frac{qc_{TA}}{\omega}\right)\right)}{16\pi^2 c_{TA}^7 m_p \rho^3 [(\omega^2-(c_{LA}q)^2)^2+(c_{LA}q)^2\Gamma^2_{LA,q}]}\,\theta(\omega-c_{TA}q)\,, \tag{4.14}$$

$$S^{(anh)}_{LATA}(q,\omega) = \frac{\left(\sum_d A_d\, q^4\, \omega^4\right)\left(g^{(anh)}_{LATA}\left(\frac{qc_{TA}}{\omega}\right)\right)}{16\pi^2 c_{TA}^7 m_p \rho^3 [(\omega^2-(c_{LA}q)^2)^2+(c_{LA}q)^2\Gamma^2_{LA,q}]}\,\theta(\omega-c_{TA}q)\,, \tag{4.15}$$

where "TATAin" and "TATAout" subscripts refer to TA-TA channels with polarizations in and orthogonal to the plane spanned by the phonon momenta. $\theta(x)$ is the Heaviside function. The $g^{(anh)}(x)$ functions all approach a constant in the $x\to 0$ limit, specifically

$$\begin{aligned} g^{(anh)}_{LALA}(x) \approx \frac{1}{240}\big(&15\alpha^2+10\alpha(10\beta+8\gamma+5\lambda+6\mu)+188\beta^2+4\beta(88\gamma+47\lambda+66\mu)\\ &+192\gamma^2+176\gamma\lambda+288\gamma\mu+47\lambda^2+132\lambda\mu+108\mu^2\big)+\mathscr{O}\left(x^2\right), \end{aligned} \tag{4.16}$$

$$\begin{aligned} g^{(anh)}_{TATAout}(x) \approx \frac{1}{240}\big(&15\beta^2+10\beta(2\gamma+3\lambda+2\mu)+12\gamma^2+4\gamma(5\lambda+6\mu)\\ &+15\lambda^2+20\lambda\mu+12\mu^2\big)+\mathscr{O}\left(x^2\right), \end{aligned} \tag{4.17}$$

$$g^{(anh)}_{TATAin}(x) \approx \frac{1}{16}\left(\beta+2\gamma+\lambda+2\mu\right)^2+\mathscr{O}\left(x^2\right), \tag{4.18}$$

$$g^{(anh)}_{LATA}(x) \approx \frac{8}{15\delta(\delta+1)^5}(2\beta+4\gamma+\lambda+3\mu)^2+\mathscr{O}\left(x^2\right), \tag{4.19}$$

where we defined $\delta \equiv c_{LA}/c_{TA}$. The $\mathscr{O}(q^4)$ scaling of this contribution, as advertised in the Introduction, is therefore manifest in (4.12), (4.13), (4.14) and (4.15). For our numerical results,

we use the full, unexpanded expressions, as given in Appendix 4.C.1.

4.2.2 Contact term

With the definition of the long-wavelength polarization tensors in (3.16), the structure factor for the contact term in (4.6) reduces to

$$S^{(cont)}(q,\omega) = \frac{1}{4}\frac{\sum_d A_d}{m_p\rho}\sum_{\nu_1,\nu_2}\int\frac{d^3\mathbf{k}_1}{(2\pi)^3}\frac{\left|(\mathbf{q}\cdot\mathbf{e}_{\nu_1,\mathbf{k}_1})(\mathbf{q}\cdot\mathbf{e}_{\nu_2,\mathbf{q}-\mathbf{k}_1})\right|^2}{c_{\nu_1}c_{\nu_2}k_1|\mathbf{q}-\mathbf{k}_1|}\delta(\omega-k_1c_{\nu_1}-|\mathbf{q}-\mathbf{k}_1|c_{\nu_2}), \tag{4.20}$$

which can also be evaluated analytically. Concretely, there are three final-state polarization configurations (LA-LA, TA-TA and LA-TA) which can contribute, where the TA modes must be polarized in the plane spanned by the momenta:

$$S^{(cont)}_{LALA}(q,\omega) = \frac{(\sum_d A_d)}{64\pi^2c_{LA}^3m_p\rho}\,q^4\,g^{(cont)}_{LALA}\left(\frac{c_{LA}q}{\omega}\right)\,\theta(\omega-c_{LA}q), \tag{4.21}$$

$$S^{(cont)}_{TATA}(q,\omega) = \frac{(\sum_d A_d)}{64\pi^2c_{TA}^3m_p\rho}\,q^4\,g^{(cont)}_{TATA}\left(\frac{c_{TA}q}{\omega}\right)\,\theta(\omega-c_{TA}q), \tag{4.22}$$

$$S^{(cont)}_{LATA}(q,\omega) = \frac{(\sum_d A_d)}{64\pi^2c_{LA}c_{TA}(c_{LA}+c_{TA})m_p\rho}q^4\,g^{(cont)}_{LATA}\left(\frac{c_{TA}q}{\omega}\right)\theta(\omega-c_{TA}q), \tag{4.23}$$

with

$$g^{(cont)}_{LALA}(x) \approx \frac{2}{5}-\frac{16}{21}x^2+\frac{16}{15}x^4+\mathcal{O}(x^6), \tag{4.24}$$

$$g^{(cont)}_{TATA}(x) \approx \frac{16}{15}-\frac{64}{35}x^2+\frac{64}{105}x^4+\mathcal{O}(x^6), \tag{4.25}$$

$$g^{(cont)}_{LATA}(x) \approx \frac{16}{15}+\frac{16}{105}\left(12\delta^2+17\delta+5\right)x^2-\frac{16}{105}\left(7\delta^3+11\delta^2+4\delta\right)x^4+\mathcal{O}(x^6), \tag{4.26}$$

where we again used $\delta=\frac{c_{LA}}{c_{TA}}$. Note that the expansion in (4.26) assumes $x\ll\frac{1}{\delta}$. The exact expressions for $g^{(cont)}_{LALA}$, $g^{(cont)}_{TATA}$ and $g^{(cont)}_{LATA}$ were used for all our numerical results (see Appendix 4.C.2). Note that the $\mathcal{O}(q^4)$ scaling discussed in the Introduction is manifest in (4.21), (4.22) and (4.23).

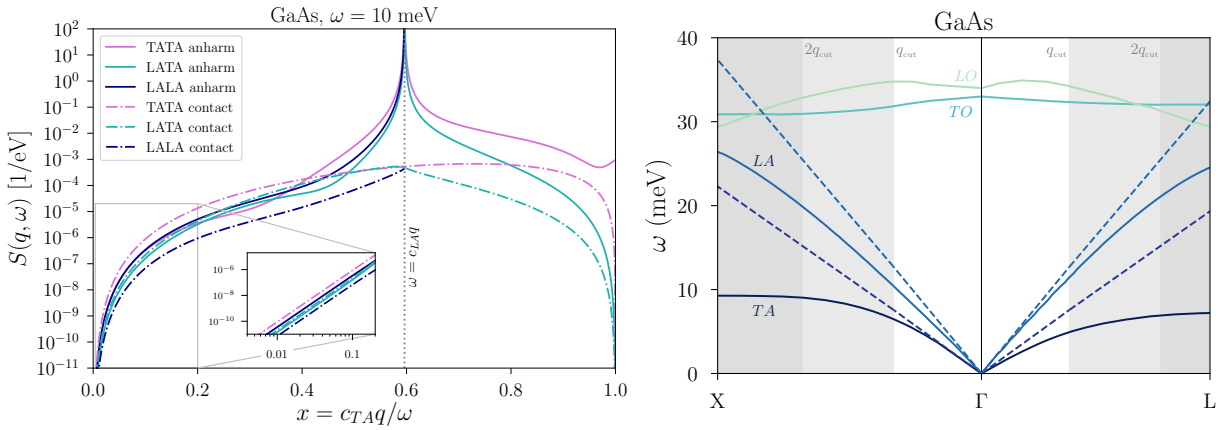

Figure 4.2. Left: Structure factors at $\omega = 10$ meV for each of the anharmonic and contact channels, evaluated numerically for GaAs with the parameters listed in Tab. 4.2. The inset shows the low-momentum regime on a log-log scale. Right: Dispersion relations for GaAs obtained with DFT methods [6], in two example directions around the origin of the Brillouin zone, indicated by "Γ". (Γ in this context is not to be confused with the phonon width.) The dashed lines indicate the long wavelength, isotropic approximation, and the light and dark gray regions show $q > q_{\text{cut}}$ and $q > 2q_{\text{cut}}$ respectively.

4.2.3 Numerical comparison

The left-hand panel of Fig. 4.2 shows the different contributions to $S(q,\omega)$ for the example of GaAs, where we summed the different TATA contributions. We show the full kinematic range, where the most striking feature is the resonance at $x = 1/\delta$ for the anharmonic contributions, indicating that the intermediate LA phonon goes on-shell. Whenever the resonance is kinematically accessible, it dominates the rate to the extent that the off-shell diphonon contribution is completely negligible. The LALA channel also cuts off for $x > 1/\delta$, since in this regime it is not possible to simultaneously conserve energy and momentum. Except for the region near the resonance, all contributions scale as ω^4 with respect to our 10 meV reference value. The inset zooms in on the low momentum region and shows the $\sim q^4$ scaling of both diphonon contributions.

The long wavelength approximation necessarily breaks down at momenta approaching the edge of the Brillouin zone for two reasons: the dispersion relations of the acoustic phonons cease to be linear, and the description of the phonon self-couplings in terms of the elasticity

parameters (Sec. 4.2.1) starts to break down. We show the dispersions in the right-hand panel of Fig. 4.2 for the example of GaAs, where the full dispersion relations [6] are compared with those in the long wavelength, isotropic approximation. To ensure that the calculation is not extrapolated beyond its regime of validity, we impose a maximum momentum cutoff of $q_{\rm cut} = 0.7$ keV for GaAs and Ge, $q_{\rm cut} = 0.8$ keV for Si, and $q_{\rm cut} = 1.2$ keV for diamond. This corresponds roughly to $q_{\rm cut} \approx q_{\rm BZ}/3$, where $q_{\rm BZ} \equiv 2\pi/a$ is the approximate boundary of the first Brillouin zone and a is the lattice spacing. The cut is indicated by the light gray shading in Fig. 4.2, and below this value the dispersions of the acoustic phonons in all four materials is close to linear. We also enforce this momentum cut on the final state phonons by imposing an upper bound on the total deposited energy of $\omega_{\rm cut} = (c_1 + c_2)q_{\rm cut}$ where $c_{1,2}$ stand for the sound speeds of the final state phonons under consideration, e.g. for the LATA channel $c_1 = c_{LA}$ and $c_2 = c_{TA}$ etc. The resulting values are summarized in Tab. 4.3.

Due to the relatively low sound speeds in GaAs and Ge, the phase space is substantially restricted by these consistency conditions. In this sense, our calculations should be viewed as a conservative estimate. The choice of $q_{\rm cut}$ is to some degree arbitrary, and therefore we also compute all rates with a $q_{\rm cut}$ that is twice the values reported in Tab. 4.3. This provides a measure of the sensitivity of our results to $q_{\rm cut}$. We expect that the long wavelength formulas overestimate the structure factor when extrapolated beyond their regime of validity because of the strong growth in q and ω, and because the isotropic linear dispersions overestimate the mode energies at large momenta. In this sense we anticipate that the true answer is bracketed by the two cutoff choices. Numerically, we find that integrating fully out to the edge of the Brillouin zone does not change the rates appreciably in comparison to our upper choice of $2q_{\rm cut} \sim 2q_{\rm BZ}/3$.

4.3 Results

Folding in the DM velocity distribution, the total rate per unit exposure is given by

$$R = \frac{\sigma_n}{\sum_d A_d m_p} \frac{\rho_\chi}{m_{DM}} \int d^3\mathbf{v}_i \, f(\mathbf{v}_i) \int_{\omega_-}^{\omega_+} d\omega \int_{q_-}^{q_+} dq \, \frac{q}{2 p_i m_{DM}} |\tilde{F}(q)|^2 S(q,\omega) \,, \tag{4.27}$$

where $\tilde{F}(q)$ indicates a form factor whose functional form is determined by the properties of the particle mediating the DM-nucleon scattering process. The most common, limiting cases are $\tilde{F}(q) = 1$ if the mediator is heavier than the DM, and $\tilde{F}(q) = v_0^2 m_{DM}^2 / q^2$ for a mediator which can be treated as massless in the scattering process. In addition, ω_- is the energy threshold of the experiment, and

$$q_- \equiv |p_i - p_f|, \quad q_+ \equiv \text{Min}\left[p_i + p_f, q_{\text{cut}}\right], \text{ and } \omega_+ \equiv \text{Min}\left[\frac{v_i^2 m_{DM}}{2}, \omega_{\text{cut}}\right], \tag{4.28}$$

where $p_i \equiv m_{DM} v_i$ and $p_f \equiv m_{DM}\sqrt{v_i^2 - 2\omega/m_{DM}}$ are the magnitudes of the initial and final DM momenta respectively. The cuts involving q_{cut} and ω_{cut} ensure that the integral is not evaluated in a regime where the long wavelength approximation is invalid, as discussed in Sec. 4.2.3. For the DM velocity distribution $f(\mathbf{v}_i)$ we use the standard truncated Maxwellian distribution in the Earth's frame:

$$f(\mathbf{v}) = \frac{1}{N_0} \exp\left[-\frac{(\mathbf{v}+\mathbf{v}_e)^2}{v_0^2}\right] \Theta\left(v_{esc} - |\mathbf{v}+\mathbf{v}_e|\right), \tag{4.29}$$

$$N_0 = \pi^{3/2} v_0^3 \left[\text{erf}\left(\frac{v_{esc}}{v_0}\right) - 2\frac{v_{esc}}{v_0} \exp\left(-\frac{v_{esc}^2}{v_0^2}\right)\right], \tag{4.30}$$

and we take $v_0 = 220$ km/s, $v_{\text{esc}} = 500$ km/s, and the Earth's average velocity to be $v_e = 240$ km/s.

Fig. 4.3 shows the differential scattering rate as a function of the deposited energy, assuming a massless mediator. All curves are cut off when the momenta of the final state

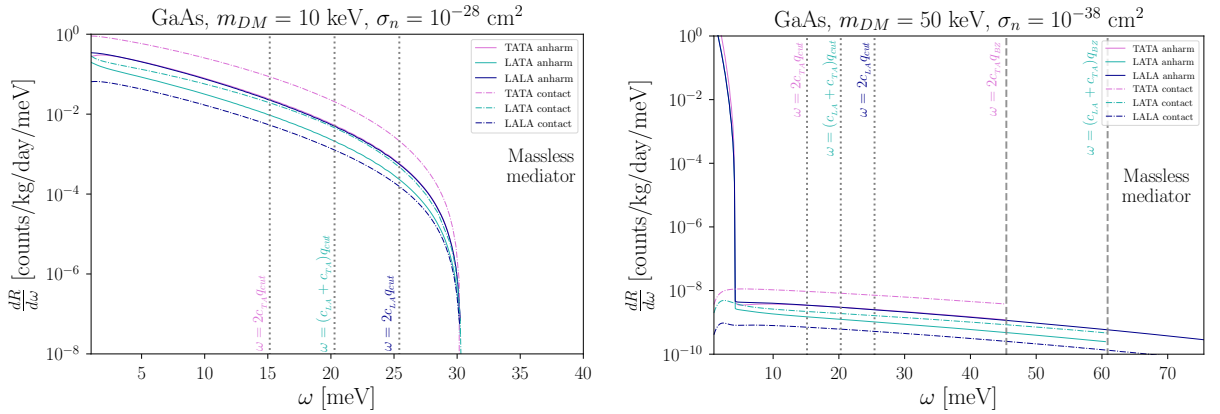

Figure 4.3. The differential rate for the different channels in GaAs. The dotted lines indicate the ω cuts for each respective channel from Tab. 4.3; the dashed lines show the cuts if we extrapolate the long wavelength approximation all the way to the edge of the Brillouin zone, and the spectra in this case should be understood as upper bounds on the true rate. The right-hand panel demonstrates the single-phonon resonance at small values of ω.

phonons are outside the first Brillouin zone. The dotted vertical lines indicate values of ω_{cut}, above which we expect that the long wavelength approximation starts to break down. Integrating the rate beyond ω_{cut} to the edge of the Brillouin zone is likely to overshoot the true answer. For the $m_{DM} = 10\,\text{keV}$ benchmark (left-hand panel), the single phonon resonance occurs for $\omega < 1$ meV, while its enormous contribution to the scattering rate is visible for $\omega < 5$ meV for the 50 keV benchmark (right-hand panel).

Fig. 4.4 shows the cross sections needed to obtain 3 events with a kg-year exposure, again assuming a massless mediator.[4] The most striking feature in Fig. 4.4 is the enormous enhancement of the reach once the single acoustic phonon becomes accessible. In this regime, integrating the diphonon structure factor matches onto the single phonon scattering rate (see Appendix 4.A) and we can simply use the single phonon structure factor. For a given experimental threshold ω_-, the mass m^*_{DM} at which the single-phonon resonance appears may be analytically derived by requiring that the maximum momentum transfer supplied by the DM suffices to create

[4]The massive mediator scenario is disfavored by BBN bounds, while the massless mediator case is in tension with stellar cooling constraints and DM self-interactions [56, 57, 58]. The latter are relaxed if the particle in question is a subcomponent of the full DM abundance.

an on-shell LA phonon above the threshold, or in other words: $2m^*_{DM}(v_{\rm esc}+v_e) \approx \omega_-/c_{LA}$ or

$$m^*_{DM} \approx \frac{1}{2}\frac{\omega_-}{c_{LA}}\frac{1}{(v_{\rm esc}+v_e)}\,. \tag{4.31}$$

Using the sound speed for GaAs and a 1 meV threshold as an example, the single-phonon resonance will appear at $m^*_{DM} \approx 12$ keV, as can be seen in Fig. 4.4. The very high sound speed of diamond then explains why this material maintains sensitivity to the single acoustic mode for most of the mass range, even for a threshold as high as ~ 10 meV. (See [39] for a detailed study of diamond as a dark matter detector.)

No backgrounds or experimental efficiencies have been included in Fig. 4.4, which is meant to both illustrate the most optimistic reach possible, as well as the *relative* importance of the various channels, rather than provide an accurate projection of the absolute reach. The single optical phonon channel is computed using an analytic approximation given in Sec. 4.4.1, with the (dispersionless) optical mode energy given in the figure labels. We see that the two-phonon channel is always subleading to the single optical, except at low m_{DM} for Si and diamond. The reason is that the longitudinal optical mode in both these materials is relatively high energy, 60 meV and 140 meV respectively, and is not kinematically accessible in the low m_{DM} region. For comparison, multiphonon production in superfluid helium is also shown in Fig. 4.4; in an idealized setting where all experimental effects aside from the threshold are neglected, it always outperforms both the single optical and two-phonon modes in crystals.

The shaded bands in Fig. 4.4 indicate the estimated uncertainty from taking the long wavelength approximation, by displaying the calculated rates using two choices for the momentum cutoff, as explained in Sec. 4.2.3. Concretely, the upper edge of the band corresponds to the values reported in Tab. 4.3, whereas the lower curves assume twice these values. This source of uncertainty is negligible once the single LA channel is accessible, as this contribution is peaked at low ω (see right-hand panel of Fig. 4.3), and moreover it does not rely on the validity of Eq. (4.9). The size of the band is larger in GaAs and Ge because of the lower sound speeds and

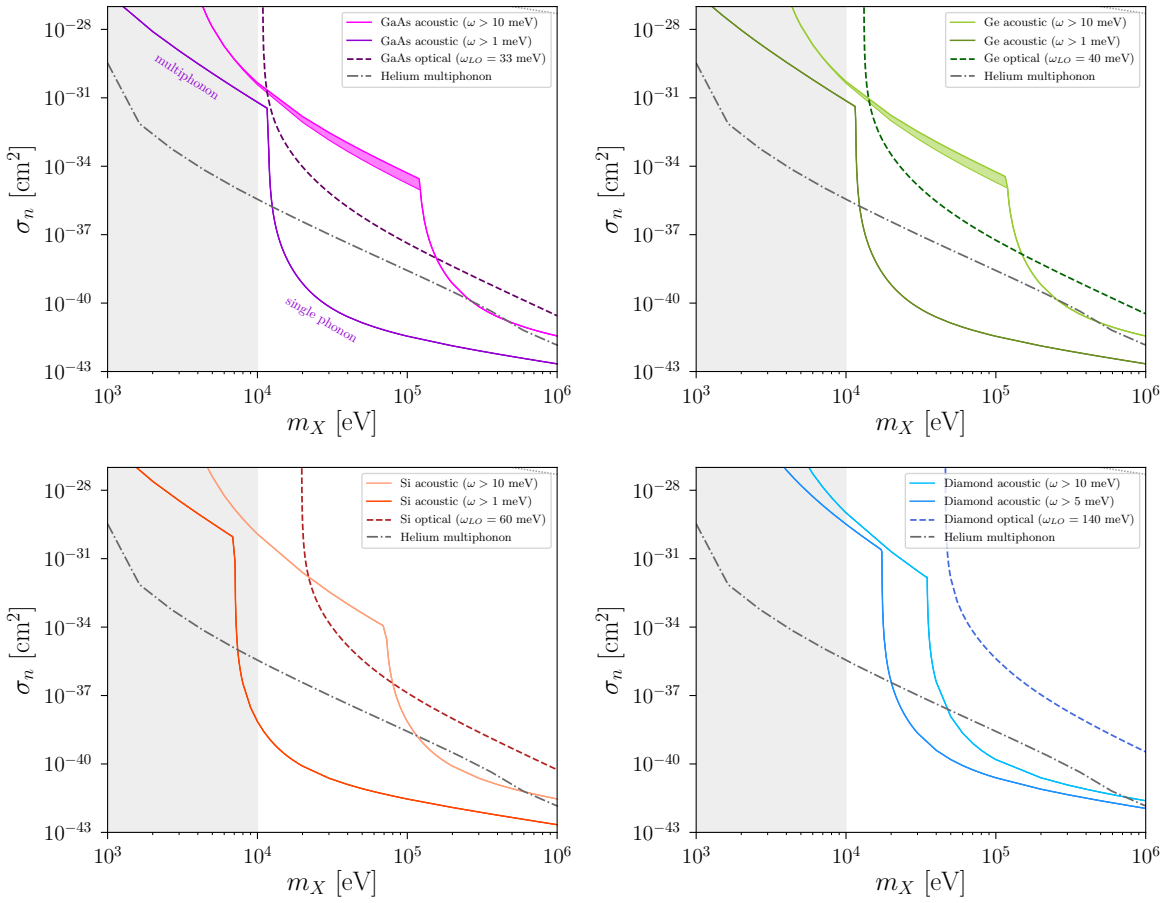

Figure 4.4. Minimum accessible cross sections for different crystals, channels and thresholds, assuming 3 events with a kg-year exposure. All curves are computed in the isotropic and long-wavelength approximations. The shaded bands indicate diphonon rates computed with the cuts in Tab. 4.3 (upper edge) and twice those values (lower edge). The curves for the single optical channel are computed with the approximation in Sec. 4.4.1. For comparison, we show the multiphonon reach in superfluid helium with the same exposure and a threshold of 1 meV [51]. The dotted line in the upper right corner indicates roughly where the DM would lose a significant fraction of its initial kinetic energy within 1 km in the Earth's crust. The gray shading for $m_{DM} < 10$ keV indicates the region where stellar cooling and warm dark matter limits likely apply.

$\omega_{\rm cut}$ (Tab. 4.3). This source of uncertainty is also more severe as the experimental threshold is increased, since this reduces the available phase space in Fig. 4.3, which leads to greater dependence on $\omega_{\rm cut}$. For a 10 meV threshold, the lower value of $\omega_{\rm cut}$ severely restricts the phase space for the TATA channel, especially for GaAs and Ge. Meanwhile, for diamond $\omega_{\rm cut}$ has no effect on the rate, since it is always larger than the initial DM kinetic energy when $m_{DM} < m^*_{DM}$.

We therefore expect the long wavelength limit be an excellent approximation in this case.

Other sources of uncertainty are the values for the elasticity parameters, as to the best of our knowledge they have not yet all been measured at ultra low temperatures. As explained in Appendix 4.B, we instead rely on *ab initio* calculations of these parameters, which in some cases carry $\mathcal{O}(1)$ uncertainties. This propagates to a small uncertainty on the overall diphonon rate, regardless of the DM mass. In addition, we expect corrections to the isotropic approximation once the detailed crystal structure is accounted for. These uncertainties are not included in the band in Fig. 4.4. Given the current experimental unknowns, we consider the uncertainties acceptable at this stage, especially given that diphonon processes typically have a much lower rate than the single optical mode.

To conclude, we briefly comment on stellar cooling constraints, warm dark matter bounds and the material overburden. For millicharged particles with mass $\lesssim 10$ keV, there are strong constraints from the cooling of white dwarfs, red giants and horizontal branch stars [59, 60]. To our knowledge, the analogous computation has not yet been performed for light DM with a coupling to nuclei, but we expect that similar constraints should apply for $m_{DM} \lesssim 10$ keV. In this mass range, the DM is also generally considered as warm and there are constraints from structure formation, although these are alleviated if this candidate doesn't provide the entire DM abundance. The likely existence of both bounds is suggested by the gray shading in Fig. 4.4. Finally, for sufficiently large σ_n, the DM is likely to scatter in the Earth's crust before reaching an underground detector. To determine roughly where this occurs, we estimated the mean free path for DM scattering off phonons in a crystalline silicon crust where the DM loses at least 1% of its typical initial kinetic energy. (While this is an idealized model, a similar result is obtained if we model DM interactions in the crust as nuclear recoils off free silicon atoms.) The dotted line in Fig. 4.4 indicates where the mean free path is 1 km. Numerically, we find this to be where $\sigma_n \gtrsim 5 \times 10^{-28}\ \mathrm{cm}^2 \times (\mathrm{MeV}/m_{DM})$.

4.4 Other channels

4.4.1 Diphonon excitations involving optical branches

As discussed in the introduction, the rate for scattering that excites a single optical phonon is suppressed when the DM coupling is proportional to the mass of the atom. Nevertheless, as seen in the previous section, processes involving optical phonons are still important, particularly for higher experimental thresholds. A discussion of the single (longitudinal) optical phonon in Chapter 3 led to the LO structure factor given by (3.20). We therefore move onto a description of two-phonon processes involving optical phonons.

There are two kinds of two-phonon processes involving optical phonons to consider: optical-acoustic, and optical-optical. We begin with the former, since they are the most relevant for light DM. Optical-acoustic scattering also has both contact and anharmonic contributions. For all of the materials we consider, there is a suppression of the contact contribution at low q when DM couples proportional to atomic mass. This can be seen from the expressions for the structure factor and matrix element in eqs. (3.12) and (4.2). When $q = 0$, momentum conservation requires $k_1 = -k_2$ and the sum over the unit cell in (3.12) vanishes due to the orthogonality of the eigenvectors. Using the low-q approximation for the LO eigenvector (3.17), one can explicitly see that the leading term in the small q expansion of the structure factor vanishes; the contact term then scales as q^6 and is negligibly small. Note that this result does not hold for general lattices, since with more complicated unit cells there can be mixed longitudinal-transverse optical modes which may only be orthogonal to the acoustic modes after also contracting the Lorentz indices of the eigenvectors.

The anharmonic contribution is more difficult to reliably calculate. It could be obtained from a first principles calculation of the anharmonic corrections to the lattice potential using Density Functional Theory, however this goes beyond the scope of the present work. Here, we adopt a simpler method in order to obtain an estimate of the size of this contribution. We follow an approach that has been used in the literature to calculate the lifetime of LO phonons and

describe the anharmonic three-phonon interactions via the Hamiltonian [61],

$$\delta H = \frac{1}{3!}\frac{\gamma_G}{\bar{c}}\sqrt{\frac{1}{2Nm_p(A_1+A_2)}}\sum_{\nu,\nu',\nu''}\sum_{\mathbf{k},\mathbf{k}',\mathbf{k}''}\sqrt{\omega_\nu\omega_{\nu'}\omega_{\nu''}}\,\delta_{\mathbf{k}+\mathbf{k}'+\mathbf{k}''} \times\left(a^\dagger_{\nu,\mathbf{k}}-a_{\nu,\mathbf{k}}\right)\left(a^\dagger_{\nu',\mathbf{k}'}-a_{\nu',\mathbf{k}'}\right)\left(a^\dagger_{\nu'',\mathbf{k}''}-a_{\nu'',\mathbf{k}''}\right), \quad (4.32)$$

where $\gamma_G \approx 1$ is the mode-averaged Grüneisen constant and $\bar{c}$ is the average of the LA and TA sound speeds. The above Hamiltonian can be obtained starting from eqs. (4.8)-(4.10) and then averaging over phonon modes and angles (see Ref. [61]). Since this model treats the lattice as an isotropic continuum it does not actually contain optical modes; nevertheless, eq. (4.32) has been used in the calculation of optical phonon lifetimes (e.g. [62, 63]).

The dominant anharmonic contribution is that mediated by an off-shell LA phonon, since the LO mediated process has the same suppression as single optical scattering. Using the Hamiltonian (4.32) in eq. (4.3) we obtain the structure factors,

$$S^{(anh)}_{LOLA}(q,\omega) = \frac{\gamma_G^2}{2\pi^2}\frac{\omega_{LO}(A_1+A_2)}{\bar{c}^2 c_{LA}\rho m_p}\frac{q^4(\omega-\omega_{LO})^3}{(\omega^2-(c_{LA}q)^2)^2}\theta(\omega-\omega_{LO}), \quad (4.33)$$

$$S^{(anh)}_{LOTA}(q,\omega) = \frac{\gamma_G^2}{\pi^2}\frac{\omega_{LO}(A_1+A_2)}{\bar{c}^2 c_{TA}\rho m_p}\frac{c_{LA}^2}{c_{TA}^2}\frac{q^4(\omega-\omega_{LO})^3}{(\omega^2-(c_{LA}q)^2)^2}\theta(\omega-\omega_{LO}), \quad (4.34)$$

where we have again assumed a flat dispersion relation for the optical mode. The expressions for the TO-LA and TO-TA processes can be obtained by the substitution $\omega_{LO} \to \omega_{TO}$ and multiplying by a factor of two. Integrating the structure factor to obtain the total rate we find that, for all the materials we consider, the LO-LA scattering rate is four to five orders of magnitude smaller than the single optical rate, where we again impose the q_{cut} values in Tab. 4.3 on the acoustic phonons (relaxing this cut increases the LO-LA rate, but it always remains negligible). The LO-TA process is enhanced by the smaller TA sound speed, but is still significantly suppressed compared to the single optical. A similar conclusion holds for optical-acoustic scattering involving TO phonons, although these processes could be relevant in a narrow range of DM masses that are

above the threshold to excite a TO phonon but below the LO threshold. While eqs. (4.33) and (4.34) should only be considered as an estimate of the two phonon optical-acoustic rate, we do not expect a detailed DFT calculation to change the qualitative conclusion that it is sub-leading compared to single optical scattering.

Next, we briefly discuss scattering into two optical phonons. This process only becomes kinematically accessible for heavier DM masses due to the higher energy threshold to excite two optical phonons. Unlike optical-acoustic scattering, there is no additional suppression of the contact contribution for DM that couples proportional to atomic mass. The LO-LO structure factor is then proportional to $q^4/(m_p\omega_{LO})^2$. On the other hand, the single optical structure factor scales as $q^4a^2\mu/(m_p^2\omega_{LO})$, where μ is the reduced mass of the primitive cell. The two optical phonon contact contribution is then expected to be significantly smaller than the single optical. The anharmonic contribution is again challenging to reliably estimate; however, based on our above estimate for optical-acoustic scattering, where it was found to be sub-leading, we do not expect it to give a significant contribution. In summary, two phonon scattering processes involving optical phonons are expected to give only a sub-leading contribution to the total scattering rate.

4.4.2 Diphonons in superfluid helium

Here we briefly compare our results with similar calculations of diphonon production in superfluid helium. While the symmetries of the systems are different, in both cases the structure factor scales as q^4 in the limit $q \ll \omega$. Crystals spontaneously break both translation and rotation invariance, but since the rotation operators are linearly dependent on the translation operators, there are only 3, rather than 6, Goldstone modes [64]. These are the 1 LA and 2 TA modes we have encountered throughout our discussion. Since translations are broken spontaneously, all amplitudes must vanish in the limit where one of the external (spatial) momenta go to zero. This symmetry principle explains the form of the amplitude in (4.10) and its scaling in the low q limit. Combined with the q-dependent DM-phonon coupling, the resulting matrix element goes as

$|\mathscr{M}|^2 \sim q^4$.

Superfluid helium on the other hand does not break translation and rotation invariance, though the Bose-Einstein condensate breaks boost invariance as well as a linear combination of the time translation and particle number operators. All four broken operators are linearly dependent, such that there only exists a single Goldstone mode [64], which is the phonon-roton branch. Here the same q^4 dependence of the structure factor can be argued from an effective field theory treatment [52, 53]. Although translation invariance is unbroken, the Ward identity associated with the $U(1)$ particle number symmetry still enforces that the two-phonon amplitude vanishes in the $\mathbf{q} \to 0$ limit [65]. Bose symmetry on the final state momenta then implies that in the low q limit, the amplitude must be proportional to

$$|\mathscr{M}_{\rm He}|^2 \;\sim\; |\mathbf{q}\cdot\mathbf{k}_1 + \mathbf{q}\cdot\mathbf{k}_2|^2 \sim q^4\,, \tag{4.35}$$

where the second $\sim$ follows from momentum conservation ($\mathbf{q} = \mathbf{k}_1 + \mathbf{k}_2$). Despite the differences in symmetries, the scaling of the dynamic structure factor for phonons in superfluid helium is the same as for longitudinal acoustic phonons in crystals. However, the multiphonon rate in helium exceeds that in the crystals we considered (see Fig. 4.4), due to the stronger phonon self-couplings in helium.

4.5 Conclusions and outlook

In this Chapter, we evaluated the rate for production of two acoustic phonons in crystals from scattering of sub-MeV DM. We considered cubic crystals such as GaAs, Ge, Si and diamond and worked in the isotropic and long wavelength approximations. In addition, we focused on DM which couples proportional to atomic mass, since in this case the rate for single optical phonon excitations is suppressed and two-phonon production is most relevant. However, for all four crystals, we found that the two-phonon rate is smaller than the single optical phonon rate whenever the optical mode is kinematically accessible. Similarly, the rate to excite a single

acoustic phonon dominates whenever that mode is kinematically accessible. In diamond and Si there is, however, a range of DM masses between 10 keV and 100 keV for which the diphonon process could be the only detectable channel, depending on the experimental threshold. We have also estimated the diphonon rate with optical phonons and expect it to be sub-leading. In idealized experimental conditions, the multiphonon rate in superfluid helium exceeds that in all the crystals we have considered.

For GaAs and Ge, our approach here in taking the long-wavelength approximation has a limited regime of validity, leading to appreciable uncertainties in the scattering rate. A more precise evaluation with Density Functional Theory methods would be desirable for these materials, which would additionally allow one to consider anisotropy's daily signal modulation. Another description is required for multiphonons in higher energy and momentum regimes, which we perform in the next Chapter by employing the incoherent approximation.

Acknowledgements

We thank Christian Bauer, Angelo Esposito, Marat Freytsis, Sinéad Griffin, Katherine Inzani, Aneesh Manohar, Harikrishnan Ramani, Nicholas Llewellyn Rodd, Tanner Trickle, James Wells, Zhengkang Zhang and Kathryn Zurek for helpful discussions, and Angelo Esposito for comments on a draft version of the manuscript. SK and TL thank the Munich Institute for Astro- and Particle Physics (MIAPP) and the Galileo Galilei Institute for Theoretical Physics for their hospitality and the INFN for partial support during the completion of this work. SK also thanks the Aspen Center for Physics, supported by National Science Foundation grant PHY-1607611. SK is supported by DOE grant DE-SC0009988 and the Paul Dirac fund at the Institute for Advanced Study. TL is supported by an Alfred P. Sloan Research Fellowship and Department of Energy (DOE) grant DE-SC0019195. PC is supported by the Australian Research Council. TM is supported by JSPS KAKENHI Grant Number JP18K13533 and JSPS KAKENHI Grant Number JP19H05810. PC and TM are supported by the World Premier International Research Center Initiative (WPI), MEXT, Japan.

This chapter, in full, is a reprint of the material as it appears in Brian Campbell-Deem, Peter Cox, Tom Melia, Simon Knapen, Tongyan Lin, Multiphonon excitations from dark matter scattering in crystals, Phys.Rev. D 101 (2020) no.3, 036006 and the Erratum: Phys.Rev. D 102 (2020) no.1, 019904. The dissertation author was one of the primary investigators and authors of this paper.

Table 4.2. For a number of cubic crystals, we give the calculated elasticity parameters in the isotropic approximation, the average sound speed for the LA and TA modes, and mass density. (See Appendix 4.B for details.)

	μ (GPa)	λ (GPa)	α (GPa)	β (GPa)	γ (GPa)	c_{LA} (km/s)	c_{TA} (km/s)	ρ (g/cm^3)
Si	61	53	-306	-10	-86	8.7	5.1	2.33
GaAs	51	45	-190	-47	-80	5.2	3.1	5.32
Ge	56	38	-124	-64	-72	5.3	3.2	5.32
Diamond	521	86	-178	-365	-1006	18.	12.2	3.51

Table 4.3. Upper bounds on q and ω used in the calculations, to ensure the validity of the long wavelength approximation. q_{cut} is roughly $2\pi/3a$ with a the lattice spacing, and the energy cuts are calculated by imposing the momentum cut on the final state phonons. We also consider cuts that are twice the values shown here.

	a (Å)	q_{cut} (keV)	$\omega_{\text{cut, TATA}}$ (meV)	$\omega_{\text{cut, LATA}}$ (meV)	$\omega_{\text{cut, LALA}}$ (meV)
Si	5.47	0.8	26	35	44
GaAs	5.65	0.7	15	20	25
Ge	5.66	0.7	16	21	26
Diamond	3.57	1.2	94	117	139

Appendices

4.A Derivation of scattering rates

In this appendix we show how the matrix elements in Sec. 4.1 are derived using time-dependent perturbation theory, including a resummation of the phonon width.

We begin by rewriting the Hamiltonian as

$$H = \frac{p_{DM}^2}{2m_{DM}} + \sum_{\nu,\mathbf{k}} \left(\omega_{\nu,\mathbf{k}} - \frac{i}{2}\Gamma_{\nu,\mathbf{k}} \right) a^\dagger_{\nu,\mathbf{k}} a_{\nu,\mathbf{k}} + H' \,, \tag{4.36}$$

with

$$H' = \mathscr{V}(\mathbf{r}) + \delta H + \sum_{\nu,\mathbf{k}} \frac{i}{2}\Gamma_{\nu,\mathbf{k}} a^\dagger_{\nu,\mathbf{k}} a_{\nu,\mathbf{k}} \,, \tag{4.37}$$

where $\mathscr{V}$ and δH are given in eqs. (3.1) and (4.9) respectively, and we have introduced the phonon width, $\Gamma_{\nu,\mathbf{k}} \sim \mathscr{O}(\delta H^2)$. In the following, H' will be treated as a perturbation. Introducing the phonon width in this way is purely a reorganisation of the perturbation series as the full Hamiltonian remains independent of $\Gamma_{\nu,\mathbf{k}}$. This approach is similar to the complex mass scheme in QFT [66] and allows for a systematic inclusion of the width at higher perturbative orders, although is not strictly necessary here since we consider only the leading corrections from δH.

Using the above Hamiltonian, we calculate the dark matter scattering rate using time-dependent perturbation theory. We assume that the system is initially described by the $H' = 0$ Hamiltonian at $t_0 \to -\infty$, and adiabatically turn on the perturbation by replacing $H' \to e^{\varepsilon t} H'$, where we eventually take the limit $\varepsilon \to 0$. Specifically, we take the initial state to be $|p_i; 0\rangle$, where p_i is the dark matter momentum and the phonons are in the ground state.

4.A.1 Single phonon

For scattering into a single phonon, the anharmonic correction is negligible and it is sufficient to consider only the leading order contribution. The transition probability to scatter and be in the state $|p_f;\nu,\mathbf{k}\rangle$ at some time t is

$$|\left\langle p_f;\nu,\mathbf{k}\right|U(t,-\infty)\left|p_i;0\right\rangle|^2 = \frac{\left|\left\langle p_f;\nu,\mathbf{k}\right|\mathscr{V}(\mathbf{r})\left|p_i;0\right\rangle\right|^2}{(\omega_{\nu,\mathbf{k}}-\omega)^2+(\Gamma_{\nu,\mathbf{k}}/2+\varepsilon)^2}\,e^{2\varepsilon t}\,, \tag{4.38}$$

where $U(t,-\infty)$ is the time evolution operator in the Schrödinger picture, and $|p_f;\nu,\mathbf{k}\rangle$ is an eigenstate of the $H'=0$ Hamiltonian. For scattering into stable final states ($\Gamma_{\nu,\mathbf{k}}=0$) the transition rate is just Fermi's Golden Rule:

$$w_{i\to f} \equiv \lim_{\varepsilon\to 0}\frac{d}{dt}|\left\langle p_f;\nu,\mathbf{k}\right|U(t,-\infty)\left|p_i;0\right\rangle|^2 = 2\pi\delta(\omega_{\nu,\mathbf{k}}-\omega)|\left\langle p_f;\nu,\mathbf{k}\right|\mathscr{V}(\mathbf{r})\left|p_i;0\right\rangle|^2\,. \tag{4.39}$$

Substituting in Eqs. (3.1) & (3.11) this becomes

$$w_{i\to f} = 2\pi\delta(\omega_{\nu,\mathbf{k}}-\omega)\left(\frac{2\pi b_n}{m_{DM}V}\right)^2\left|\tilde{F}(q)\right|^2\left|\sum_d^{\mathfrak{n}} A_d e^{-W_d(0)}\mathscr{M}^{(1-ph)}_{|\nu,\mathbf{k}\rangle,\mathbf{q},d}\right|^2, \tag{4.40}$$

where $\mathscr{M}^{(1-ph)}$ is defined in Eq. (3.14), and V is a volume factor from the normalisation of the DM momentum eigenstates. The transition rate is directly related to the structure factor in Eq. (3.12) up to overall factors.

Note that for unstable final states ($\Gamma_{\nu,\mathbf{k}}\neq 0$) $w_{i\to f}$ vanishes. In this case the transition probability in Eq. (4.38) does not grow with time (it is constant when $\varepsilon\to 0$), since due to the exponential decay of the state only the last $\Delta t\sim\Gamma^{-1}_{\nu,\mathbf{k}}$ contributes significantly.

4.A.2 Two phonon

Next, consider scattering into the two phonon state $|p_f;\nu_1,\mathbf{k}_1;\nu_2,\mathbf{k}_2\rangle$ (with $\Gamma_{\nu_1,\mathbf{k}_1}=\Gamma_{\nu_2,\mathbf{k}_2}=0$). In this case anharmonic effects enter at second (mixed) order in perturbation theory

and can have a significant impact on the scattering rate. The transition rate is

$$
\begin{aligned}
w_{i\to f} &= 2\pi\delta(\omega_{\nu_1,\mathbf{k}_1}+\omega_{\nu_2,\mathbf{k}_2}-\omega) \\
&\times\left|\left\langle p_f;\nu_1,\mathbf{k}_1;\nu_2,\mathbf{k}_2\right|\mathscr{V}(\mathbf{r})\left|p_i;0\right\rangle+\sum_{\nu,\mathbf{k}}\left(\frac{\left\langle p_f;\nu,\mathbf{k}\right|\mathscr{V}(\mathbf{r})\left|p_i;0\right\rangle\left\langle\nu_1,\mathbf{k}_1;\nu_2,\mathbf{k}_2\right|\delta H\left|\nu,\mathbf{k}\right\rangle}{\omega-\omega_{\nu,\mathbf{k}}+i\Gamma_{\nu,\mathbf{k}}/2}\right.\right. \\
&\left.\left.+\frac{\left\langle\nu,\mathbf{k};\nu_1,\mathbf{k}_1;\nu_2,\mathbf{k}_2\right|\delta H\left|0\right\rangle\left\langle p_f;0\right|\mathscr{V}(\mathbf{r})\left|p_i;\nu,\mathbf{k}\right\rangle}{-\omega-\omega_{\nu,\mathbf{k}}+i\Gamma_{\nu,\mathbf{k}}/2}\right)\right|^2 \qquad (4.41)\\
&= 2\pi\delta(\omega_{\nu_1,\mathbf{k}_1}+\omega_{\nu_2,\mathbf{k}_2}-\omega)\left(\frac{2\pi b_n}{m_{DM}V}\right)^2\left|\tilde{F}(q)\right|^2 \\
&\times\left|\sum_d^{\mathrm{n}}A_d e^{-W_d(0)}\left(\mathscr{M}^{(cont)}_{|\nu_1,\mathbf{k}_1;\nu_2,\mathbf{k}_2\rangle,\mathbf{q},d}+\mathscr{M}^{(anh)}_{|\nu_1,\mathbf{k}_1;\nu_2,\mathbf{k}_2\rangle,\mathbf{q},d}\right)\right|^2. \qquad (4.42)
\end{aligned}
$$

The contact and anharmonic contributions are shown diagrammatically in Fig. 4.1, with the matrix elements given in eqs. (4.2) & (4.3), and the δH matrix element discussed in Sec. 4.2.1. In the narrow width limit ($\Gamma_{\nu,\mathbf{k}}/\omega_{\nu,\mathbf{k}}\to 0$), and neglecting the interference terms, the anharmonic contribution reduces to the single phonon rate times the branching ratio to $|\nu_1,\mathbf{k_1};\nu_2,\mathbf{k_2}\rangle$. Similarly, while eq. (4.41) is strictly only valid for scattering into stable final states, the narrow width approximation applied to diphonon scattering justifies its use for final states with non-zero width.

4.B Elasticity theory

4.B.1 The three-phonon Hamiltonian

In this appendix we briefly review how the leading anharmonic correction to the phonon Hamiltonian can be written in terms of the elasticity parameters, following Refs. [67, 54]. In elasticity theory, the measure of the size of an infinitesimal deformation of an object is

$$
d\mathbf{x}^2-d\mathbf{a}^2=\left(\frac{\partial x_k}{\partial a_i}da_i\right)\left(\frac{\partial x_k}{\partial a_j}da_j\right)-da_i da_j=2\eta_{ij}da_i da_j\,, \qquad (4.43)
$$

with **x** and **a** the coordinates of a piece of the deformed and undeformed material respectively. We defined the *Green - St-Venant strain tensor*

$$\eta_{ij} \equiv \frac{1}{2}\left(\frac{\partial x_k}{\partial a_i}\frac{\partial x_k}{\partial a_j} - \delta_{ij}\right), \tag{4.44}$$

which measures how a material responds under stress. Since $x_i = u_i + a_i$ by definition, we can use

$$\frac{\partial x_i}{\partial a_j} = \frac{\partial u_i}{\partial a_j} + \delta_{ij} \tag{4.45}$$

to rewrite the strain tensor as

$$\eta_{ij} = \frac{1}{2}\left(\frac{\partial u_j}{\partial a_i} + \frac{\partial u_i}{\partial a_j} + \frac{\partial u_k}{\partial a_i}\frac{\partial u_k}{\partial a_j}\right) \tag{4.46}$$

$$= \frac{1}{2}\left(u_{ij} + u_{ji} + u_{ki}u_{kj}\right), \tag{4.47}$$

with $u_{ij} \equiv \partial_i u_j$. Note that η_{ij} is manifestly symmetric.

The generalization of Hooke's law is [67]

$$\sigma_{ij} = C_{ijk\ell}\eta_{k\ell}, \tag{4.48}$$

with $C_{ijk\ell}$ the elastic constants and σ_{ij} the stress tensor. This relation can be written in Hamiltonian form

$$H = \frac{1}{2}C_{ijk\ell}\eta_{ij}\eta_{k\ell} - \sigma_{ij}\eta_{ij}, \tag{4.49}$$

where the stress tensor σ_{ij} acts as a source for the η_{ij}. (4.48) is then just the equation of motion of η_{ij} given by this Hamiltonian. Dropping the source term, the Hamiltonian in (4.49) can be further generalized to include the cubic response

$$H = \frac{1}{2}C_{ijk\ell}\eta_{ij}\eta_{k\ell} + \frac{1}{3!}C_{ijk\ell mn}\eta_{ij}\eta_{k\ell}\eta_{mn}, \tag{4.50}$$

where the $C_{ijk\ell mn}$ are the third order elasticity constants. $C_{ijk\ell}$ is invariant under $i \leftrightarrow j$, $k \leftrightarrow \ell$ and $(ij) \leftrightarrow (k\ell)$, $C_{ijk\ell mn}$ is invariant under $i \leftrightarrow j$, $k \leftrightarrow \ell$, $m \leftrightarrow n$ and the permutations of the (ij), $(k\ell)$ and (mn) pairs. In the most general case, $C_{ijk\ell}$ and $C_{ijk\ell mn}$ have therefore respectively 21 and 56 independent components.

In the isotropic limit, both tensors simplify substantially: $C_{ijk\ell}$ has only 2 independent second order elastic constants, the *Lamé parameters* μ and λ, which can be related directly to the shear modulus and Young's modulus. The $C_{ijk\ell mn}$ has 3 independent components, parametrized by the third order elastic constants, α, β and γ. Concretely, we can write

$$C^{(iso)}_{ijk\ell} = \lambda\, \delta_{ij}\delta_{k\ell} + \mu \left(\delta_{ik}\delta_{j\ell} + \delta_{i\ell}\delta_{jk}\right), \tag{4.51}$$

$$\begin{aligned} C^{(iso)}_{ijk\ell mn} = {} & \alpha\, \delta_{ij}\delta_{k\ell}\delta_{mn} \\ & + \beta \Big[\delta_{ij} \left(\delta_{km}\delta_{\ell n} + \delta_{kn}\delta_{\ell m}\right) + \delta_{k\ell} \left(\delta_{im}\delta_{jn} + \delta_{in}\delta_{jm}\right) + \delta_{mn} \left(\delta_{ik}\delta_{j\ell} + \delta_{i\ell}\delta_{jk}\right) \Big] \\ & + \gamma \Big[\delta_{nj} \left(\delta_{ik}\delta_{\ell m} + \delta_{i\ell}\delta_{km}\right) + \delta_{ni} \left(\delta_{jk}\delta_{\ell m} + \delta_{j\ell}\delta_{km}\right) + \delta_{mj} \left(\delta_{ik}\delta_{\ell n} + \delta_{i\ell}\delta_{kn}\right) \\ & + \delta_{mi} \left(\delta_{jk}\delta_{\ell n} + \delta_{j\ell}\delta_{kn}\right) \Big], \end{aligned} \tag{4.52}$$

where the δ_{ij} etc. are Kronecker-δ symbols. Inserting (4.47), (4.51) and (4.52) back into (4.50) gives the Hamiltonian in (4.9).

4.B.2 The isotropic approximation

The cubic crystals we consider in this Chapter are not completely isotropic but instead are only invariant under permutations of the x, y and z axes and parity transformations such as $x \to -x$ etc. The latter imply that all components of $C^{(cub)}_{ijk\ell}$ and $C^{(cub)}_{ijk\ell mn}$ for which a value of an index occurs an odd number of times must vanish (e.g. $C^{(cub)}_{1222} = 0$ etc). One can show that imposing these symmetries reduces the general elasticity tensors to 3 independent second order elastic constants, and 6 independent third order elastic constants. In order to express the 5 isotropic elasticity parameters $\mu, \lambda, \alpha, \beta$ and γ in terms of these 9 measured elasticity parameters

for the cubic crystals of interest an averaging procedure is needed.

Given that a 6-tensor such $C^{(cub)}_{ijk\ell mn}$ can be rather unwieldy, much of the literature has chosen to adhere to the *Voigt convention*, where each pair of double indices (ij), $(k\ell)$ and (mn) is replaced with a single index running from 1 to 6 through the mapping

$$\eta_{11} \to \eta_1, \quad \eta_{22} \to \eta_2, \quad \eta_{33} \to \eta_3, \quad \eta_{23} \to \frac{1}{2}\eta_4, \quad \eta_{13} \to \frac{1}{2}\eta_5, \quad \eta_{12} \to \frac{1}{2}\eta_6. \tag{4.53}$$

This maps $C^{(cub)}_{ijk\ell}$ and $C^{(cub)}_{ijk\ell mn}$ to a 2-tensor ($c^{(cub)}_{ij}$) and a 3-tensor ($c^{(cub)}_{ijk}$) respectively, where we have used lowercase c for components of the elasticity tensors in Voigt notation. The independent elasticity parameters for a cubic crystal, as typically reported in the literature, are c_{11}, c_{12} and c_{44} for the second order elastic tensor and c_{111}, c_{112}, c_{123}, c_{144}, c_{166} and c_{456} for the third order elastic tensor[5], where we have dropped the (cub) superscript going forward. All other components either vanish or can be obtained by applying one of the symmetries listed above. An explicit representation of c_{ij} and c_{ijk} can be found in e.g. [68].

To obtain the elasticity parameters in the isotropic approximation an averaging procedure must be performed, introducing a certain degree of arbitrariness. We follow the prescription in [55], and define the quantities

$$f_2 = \sum_{i,j,k,\ell} \left(C^{(cub)}_{ijk\ell} - C^{(iso)}_{ijk\ell} \right)^2, \tag{4.54}$$

$$f_3 = \sum_{i,j,k,\ell,m,n} \left(C^{(cub)}_{ijk\ell mn} - C^{(iso)}_{ijk\ell mn} \right)^2, \tag{4.55}$$

which provide a measure of the deviation of the isotropic approximation from the cubic case.

[5] In certain references c_{155} is reported instead of c_{166}; for cubic symmetry $c_{155} = c_{166}$.

Minimizing both f_2 and f_3 leads to the definitions

$$\mu \equiv \frac{1}{5}\left(c_{11} - c_{12} + 3c_{44}\right), \tag{4.56}$$

$$\lambda \equiv \frac{1}{5}\left(c_{11} + 4c_{12} - 2c_{44}\right), \tag{4.57}$$

$$\alpha \equiv \frac{1}{35}\left(c_{111} + 18c_{112} + 16c_{123} - 30c_{144} - 12c_{166} + 16c_{456}\right), \tag{4.58}$$

$$\beta \equiv \frac{1}{35}\left(c_{111} + 4c_{112} - 5c_{123} + 19c_{144} + 2c_{166} - 12c_{456}\right), \tag{4.59}$$

$$\gamma \equiv \frac{1}{35}\left(c_{111} - 3c_{112} + 2c_{123} - 9c_{144} + 9c_{166} + 9c_{456}\right), \tag{4.60}$$

in agreement with [55]. In the isotropic approximation, the averaged sound speeds of the acoustic phonon modes may also be expressed in terms of λ, μ, and the mass density ρ as

$$c_{LA} = \sqrt{\frac{\lambda + 2\mu}{\rho}} \qquad \text{and} \qquad c_{TA} = \sqrt{\frac{\mu}{\rho}}. \tag{4.61}$$

Both measurements and *ab initio* calculations of the third-order elastic constants are considered rather challenging, and no complete set of experimental results is currently available at close-to-zero temperature. The temperature dependence is mild between room temperature and liquid Nitrogen temperature, but can be large for lower temperatures. For instance, for Ge the combination of $c_{123} + 6c_{144} + 8c_{456}$ shows a $\mathcal{O}(100\%)$ variation between 77K and 3K and even changes sign [69]. Similarly, the discrepancy between experiment and theory for diamond is also large for c_{123}, c_{144} and c_{456} [70], presumably due to this temperature dependence. We therefore choose to use the values calculated with Density Functional Theory methods, which are inherently at zero temperature. The values that were used to compute the parameters in Tab. 4.2 are listed in Tab. 4.B.1.

Table 4.B.1. Elasticity parameters at $T = 0K$, in units of GPa.

	Si[6]	GaAs[7]	Ge[8]	Diamond[9]
c_{11}	153	126	129.86	1051
c_{12}	65	55	47.39	125
c_{44}	73	61	65.73	560
c_{111}	-698	-600	-708	-7611
c_{112}	-451	-401	-346	-1637
c_{123}	-112	-94	-26	604
c_{144}	74	10	-10	-199
c_{166}	-253	-305	-279	-2799
c_{456}	-57	-43	-40	-1148

4.C Exact expressions for long-wavelength structure factors

4.C.1 Anharmonic contributions

All expressions below are valid on the domain $0 < x < 1$, as specified by the Heaviside functions in (4.12), (4.13), (4.14) and (4.15). We further defined $\delta \equiv c_{LA}/c_{TA}$. The full expression for the phase space integral for the LA-LA contribution in (4.12) of Sec. 4.2.1 is then

$$g^{(anh)}_{LALA}(x) \equiv (2\beta+4\gamma+\lambda+3\mu)^2 \frac{\left(x^2-1\right)^3}{2x^5}\left(x^6+3x^4+7x^2+5\right)\left(\tanh^{-1}(x)-\frac{x^3}{3}-x\right)$$
$$+ a_{10}x^{10}+a_8x^8+a_6x^6+a_4x^4+a_2x^2+a_0\,, \tag{4.62}$$

with

$$a_{10} \equiv \frac{1}{6}(2\beta+4\gamma+\lambda+3\mu)^2\,, \tag{4.63}$$
$$a_8 \equiv \frac{1}{2}(2\beta+4\gamma+\lambda+3\mu)^2\,, \tag{4.64}$$
$$a_6 \equiv -\frac{1}{3}(2\beta+4\gamma+\lambda+3\mu)^2\,, \tag{4.65}$$
$$a_4 \equiv \frac{1}{240}\Big(3\alpha^2+2\alpha(106\beta+200\gamma+53\lambda+150\mu)+332\beta^2+4\beta(120\gamma+83\lambda+90\mu)$$
$$-320\gamma^2+240\gamma\lambda-480\gamma\mu+83\lambda^2+180\lambda\mu-180\mu^2\Big)\,, \tag{4.66}$$

$$a_2 \equiv -\frac{1}{120}\Big(5\alpha^2+2\alpha(54\beta+88\gamma+27\lambda+66\mu)+516\beta^2+12\beta(136\gamma+43\lambda+102\mu)$$
$$+1280\gamma^2+816\gamma\lambda+1920\gamma\mu+129\lambda^2+612\lambda\mu+720\mu^2\Big), \tag{4.67}$$
$$a_0 \equiv \frac{1}{240}\Big(15\alpha^2+10\alpha(10\beta+8\gamma+5\lambda+6\mu)+668\beta^2+4\beta(568\gamma+167\lambda+426\mu)$$
$$+2112\gamma^2+1136\gamma\lambda+3168\gamma\mu+167\lambda^2+852\lambda\mu+1188\mu^2\Big). \tag{4.68}$$

The out-of-plane TA-TA contribution in (4.13) is given by

$$g^{(anh)}_{TATAout}(x) \equiv b_4x^4+b_2x^2+b_0, \tag{4.69}$$

with

$$b_4 \equiv \frac{43\beta^2+2\beta(50\gamma+43\lambda+50\mu)+60\gamma^2+20\gamma(5\lambda+6\mu)+43\lambda^2+100\lambda\mu+60\mu^2}{240}, \tag{4.70}$$
$$b_2 \equiv -\frac{25\beta^2+44\beta\gamma+50\beta\lambda+44\beta\mu+20\gamma^2+44\gamma\lambda+40\gamma\mu+25\lambda^2+44\lambda\mu+20\mu^2}{120}, \tag{4.71}$$
$$b_0 \equiv \frac{15\beta^2+10\beta(2\gamma+3\lambda+2\mu)+12\gamma^2+4\gamma(5\lambda+6\mu)+15\lambda^2+20\lambda\mu+12\mu^2}{240}. \tag{4.72}$$

The in-plane TA-TA contribution in (4.14) is

$$g^{(anh)}_{TATAin}(x) \equiv \frac{1}{2}(2\beta+4\gamma+\lambda+3\mu)^2\frac{\left(x^2-1\right)^3\left(x^2+3\right)}{x}\left(\tanh^{-1}(x)-\frac{x^3}{3}-x\right)$$
$$+c_{10}x^{10}+c_8x^8+c_6x^6+c_4x^4+c_2x^2+c_0, \tag{4.73}$$

with

$$c_{10} \equiv \frac{1}{6}(2\beta+4\gamma+\lambda+3\mu)^2, \tag{4.74}$$

$$c_8 \equiv \frac{1}{2}(2\beta+4\gamma+\lambda+3\mu)^2\,, \tag{4.75}$$

$$c_6 \equiv -\frac{3}{2}(2\beta+4\gamma+\lambda+3\mu)^2\,, \tag{4.76}$$

$$c_4 \equiv \frac{1}{240}\big(963\beta^2+3852\beta\gamma+1046\beta\lambda+2972\beta\mu+3852\gamma^2+2092\gamma\lambda + 5944\gamma\mu+283\lambda^2+1612\lambda\mu+2292\mu^2\big)\,, \tag{4.77}$$

$$c_2 \equiv -\frac{1}{24}\big(17\beta^2+68\beta\gamma+26\beta\lambda+60\beta\mu+68\gamma^2+52\gamma\lambda + 120\gamma\mu+9\lambda^2+44\lambda\mu+52\mu^2\big)\,, \tag{4.78}$$

$$c_0 \equiv \frac{1}{16}(\beta+2\gamma+\lambda+2\mu)^2\,. \tag{4.79}$$

Finally, the LA-TA contribution is given by the piecewise function

$$g^{(anh)}_{LATA}(x) \equiv \begin{cases} g^{(anh)}_{LATA,1}(x) & \text{if } 0<x<\frac{1}{\delta}\,, \\ g^{(anh)}_{LATA,2}(x) & \text{if } \frac{1}{\delta}<x<1\,, \end{cases} \tag{4.80}$$

where

$$\begin{aligned} g^{(anh)}_{LATA,1}(x) \equiv \frac{(2\beta+4\gamma+\lambda+3\mu)^2}{2(\delta+1)^5}\Bigg[&-(\delta+1)^5\frac{\left(x^2-1\right)^3\left(x^2+3\right)}{x}\left(\tanh^{-1}(x)-\frac{x^3}{3}-x\right) \\ &-\frac{(\delta+1)^5}{\delta^{12}}\frac{\left(\delta^2x^2-1\right)^3\left(\delta^6x^6+3\delta^4x^4+7\delta^2x^2+5\right)}{x^5}\left(\tanh^{-1}(\delta x)-\frac{1}{3}\delta^3x^3-\delta x\right) \\ &+d_{10}x^{10}+d_8x^8+d_6x^6+d_4x^4+d_2x^2+d_0\Bigg]\,, \end{aligned} \tag{4.81}$$

with

$$d_{10} \equiv -\frac{1}{3}(\delta+1)^6\left(\delta^2-\delta+1\right)\,, \tag{4.82}$$

$$d_8 \equiv -(\delta+1)^6\,, \tag{4.83}$$

$$d_6 \equiv \frac{1}{3\delta}(\delta+1)^5(9\delta+2)\,, \tag{4.84}$$

$$d_4 \equiv -\frac{1}{315\delta^3}\big(189\delta^8+945\delta^7+2706\delta^6+5340\delta^5+5779\delta^4 + 1505\delta^3-2460\delta^2-1870\delta-374\big), \tag{4.85}$$

$$d_2 \equiv \frac{1}{105\delta^5}\big(-32\delta^6+365\delta^5+1057\delta^4+930\delta^3+930\delta^2+465\delta+93\big), \tag{4.86}$$

$$d_0 \equiv -\frac{1}{15\delta^7}\big(-16\delta^6+15\delta^5+75\delta^4+150\delta^3+150\delta^2+75\delta+15\big), \tag{4.87}$$

and

$$g^{(anh)}_{LATA,2}(x) \equiv \frac{(2\beta+4\gamma+\lambda+3\mu)^2}{2\delta^{12}\left(\delta^2-1\right)^5 x^5}\Bigg[-\left(\delta^2-1\right)^5\left(\delta^2x^2-1\right)^3\left(\delta^6x^6+3\delta^4x^4+7\delta^2x^2+5\right) \times\coth^{-1}(\delta x)+\left(\delta^2-1\right)^5\left[\left(6\delta^{12}+\delta^8\right)x^8-8(\delta^{12}+\delta^6)x^6+3\left(\delta^{12}+\delta^4\right)x^4 + 8\delta^2x^2-5\right]\coth^{-1}(\delta)+\sum_{i=1}^{11}e_ix^i\Bigg], \tag{4.88}$$

with

$$e_{11} \equiv \delta^{11}\left(\delta^2-1\right)^5, \tag{4.89}$$

$$e_{10} \equiv 0, \tag{4.90}$$

$$e_9 \equiv \frac{\delta^9}{315}\left(105\delta^{10}-861\delta^8+3066\delta^6-4266\delta^4+525\delta^2+151\right), \tag{4.91}$$

$$e_8 \equiv \frac{\delta^9}{3}\left(-18\delta^{12}+84\delta^{10}-147\delta^8+74\delta^6+82\delta^4-14\delta^2+3\right), \tag{4.92}$$

$$e_7 \equiv -\frac{2\delta^7}{105}\left(105\delta^{10}-1645\delta^8+5474\delta^6-2914\delta^4+1605\delta^2-321\right), \tag{4.93}$$

$$e_6 \equiv \frac{8\delta^7}{3}\left(3\delta^{14}-14\delta^{12}+26\delta^{10}-29\delta^8+43\delta^6-24\delta^4+14\delta^2-3\right), \tag{4.94}$$

$$e_5 \equiv -\frac{2\delta^5}{15}\left(5\delta^{10}+255\delta^8-342\delta^6+350\delta^4-175\delta^2+35\right), \tag{4.95}$$

$$e_4 \equiv \frac{\delta^5}{15}\big(-45\delta^{16}+210\delta^{14}-384\delta^{12}+334\delta^{10}+16\delta^8-350\delta^6 + 384\delta^4-210\delta^2+45\big), \tag{4.96}$$

$$e_3 \equiv \frac{19\delta^3}{3}\left(\delta^2-1\right)^5, \tag{4.97}$$

$$e_2 \equiv -\frac{8\delta^3}{105}\left(34\delta^{10} - 329\delta^8 + 790\delta^6 - 896\delta^4 + 490\delta^2 - 105\right), \tag{4.98}$$

$$e_1 \equiv -5\delta\left(\delta^2 - 1\right)^5, \tag{4.99}$$

$$e_0 \equiv \frac{64\delta^{11}}{35} - \frac{965\delta^9}{63} + \frac{790\delta^7}{21} - \frac{128\delta^5}{3} + \frac{70\delta^3}{3} - 5\delta. \tag{4.100}$$

From the matrix element in Eq. (4.10), the widths for each anharmonic channel may be calculated explicitly, giving

$$\Gamma_{\mathrm{LA}\to\mathrm{LALA}}(q) = \frac{q^5}{960\pi {c_{LA}}^4\rho^3}\left(\alpha + 6\beta + 8\gamma + 3\lambda + 6\mu\right)^2, \tag{4.101}$$

and

$$\Gamma_{\mathrm{LA}\to\mathrm{TATAin}}(q) = \frac{q^5}{7680\pi {c_{LA}}^4\rho^3}\left(f_1\left(\delta^2-1\right)^3\left(1+3\delta^2\right)\coth^{-1}(\delta) + \sum_{i=1}^{i=4} f_i\delta^{2i-1}\right), \tag{4.102}$$

with

$$\begin{aligned} f_4 \equiv\ & 15(97\beta^2 + 388\beta\gamma + 388\gamma^2 + 98\beta\gamma + 196\gamma\lambda + 25\lambda^2 \\ & + 4\mu\left(73\left(\beta + 2\gamma\right) + 37\lambda\right) + 220\mu^2), \end{aligned} \tag{4.103}$$

$$\begin{aligned} f_3 \equiv\ & -10(353\beta^2 + 1412\gamma^2 + 724\gamma\lambda + 93\lambda^2 + 2136\gamma\mu + 548\lambda\mu \\ & + 808\mu^2 + 2\beta\left(706\gamma + 181\lambda + 534\mu\right)), \end{aligned} \tag{4.104}$$

$$\begin{aligned} f_2 \equiv\ & 2563\beta^2 + 10252\gamma^2 + 5292\gamma\lambda + 683\lambda^2 + 15544\gamma\mu + 4012\lambda\mu \\ & + 5892\mu^2 + 2\beta\left(5126\gamma + 1323\lambda + 3886\mu\right), \end{aligned} \tag{4.105}$$

$$f_1 \equiv -120\left(2\beta + 4\gamma + \lambda + 3\mu\right)^2, \tag{4.106}$$

and

$$\Gamma_{\mathrm{LA}\to\mathrm{TATAout}}(q) = \frac{q^5}{7680\pi {c_{LA}}^4 \rho^3} \sum_{i=1}^{i=4} g_i \delta^{2i-1}, \tag{4.107}$$

with

$$\begin{aligned} g_4 &\equiv 15\beta^2 + 20\beta\gamma + 12\gamma^2 + 30\beta\lambda + 20\gamma\lambda + 15\lambda^2 \\ &\quad + 4\mu(5\beta + 6\gamma + 5\lambda) + 12\mu^2, \end{aligned} \tag{4.108}$$

$$\begin{aligned} g_3 &\equiv -2(25\beta^2 + 20\gamma^2 + 44\gamma\lambda + 25\lambda^2 + 40\gamma\mu + 44\lambda\mu \\ &\quad + 20\mu^2 + \beta(44\gamma + 50\lambda + 44\mu)), \end{aligned} \tag{4.109}$$

$$\begin{aligned} g_2 &\equiv 43\beta^2 + 100\beta\gamma + 60\gamma^2 + 86\beta\lambda + 100\gamma\lambda + 43\lambda^2 \\ &\quad + 20\mu(5\beta + 6\gamma + 5\lambda) + 60\mu^2, \end{aligned} \tag{4.110}$$

$$g_1 \equiv 0, \tag{4.111}$$

and finally

$$\Gamma_{\mathrm{LA}\to\mathrm{LATA}}(q) = \frac{h_{12} q^5}{64\pi {c_{LA}}^4 \rho^3} \left(\left(\delta^2 - 1\right)^3 \left(1 + 3\delta^2\right) \coth^{-1}(\delta) + \frac{(1-\delta)}{315\,(1+\delta)^5} \sum_{i=0}^{i=11} h_i \delta^i \right), \tag{4.112}$$

with

$$h_{12} \equiv (2\beta + 4\gamma + \lambda + 3\mu)^2, \tag{4.113}$$

$$h_{11} \equiv 945, \tag{4.114}$$

$$h_{10} \equiv 5670, \tag{4.115}$$

$$h_9 \equiv 12915, \tag{4.116}$$

$$h_8 \equiv 11340, \tag{4.117}$$

$$h_7 \equiv -4746\,, \tag{4.118}$$

$$h_6 \equiv -19656\,, \tag{4.119}$$

$$h_5 \equiv -18030\,, \tag{4.120}$$

$$h_4 \equiv -6540\,, \tag{4.121}$$

$$h_3 \equiv 793\,, \tag{4.122}$$

$$h_2 \equiv 2658\,, \tag{4.123}$$

$$h_1 \equiv 1083\,, \tag{4.124}$$

$$h_0 \equiv 128\,. \tag{4.125}$$

4.C.2 Contact contributions

The functions parametrizing the phase space integrals in Sec. 4.2.2 can be expressed as

$$g^{(cont)}_{LALA}(x) \equiv \frac{-x(x^6+x^4-x^2-3)+(x^8+2x^4-3)\tanh^{-1}(x)}{x^5}\,, \tag{4.126}$$

$$g^{(cont)}_{TATA}(x) \equiv \frac{(1-x^2)^2}{x^5}\left(x(3-x^2)+(x^4+2x^2-3)\tanh^{-1}(x)\right)\,. \tag{4.127}$$

The LA-TA mode is given by the piecewise function

$$g^{(cont)}_{LATA}(x) \equiv \begin{cases} g^{(cont)}_{LATA,1}(x) & \text{if } 0<x<\frac{1}{\delta}\,, \\ g^{(cont)}_{LATA,2}(x) & \text{if } \frac{1}{\delta}<x<1\,, \end{cases} \tag{4.128}$$

with

$$\begin{aligned} g^{(cont)}_{LATA,1}(x) \equiv & -\frac{\delta(\delta+1)}{x^5}\left[\left(x^2+3\right)\left(x^2-1\right)^3\tanh^{-1}(x)+\left(x^8+\frac{2x^4}{\delta^4}-\frac{3}{\delta^8}\right)\tanh^{-1}(\delta x)\right] \\ & +\frac{1}{15\delta^6x^4}\left[15(\delta+1)^2\delta^6x^6+\left(-59\delta^4-59\delta^3+16\delta^2+21\delta+21\right)\delta^4x^4\right. \\ & \left.+15\left(7\delta^6+7\delta^5-\delta-1\right)\delta^2x^2-45\left(\delta^8+\delta^7+\delta+1\right)\right]\,, \end{aligned} \tag{4.129}$$

$$
\begin{aligned}
g^{(cont)}_{LATA,2}(x) \equiv & -\frac{\delta(\delta+1)}{x^5}\left[\left(8x^2-\left(\frac{2}{\delta^4}+6\right)x^4-3+\frac{3}{\delta^8}\right)\coth^{-1}(\delta)\right. \\
& \left.+\left(x^8+\frac{2x^4}{\delta^4}-\frac{3}{\delta^8}\right)\coth^{-1}(\delta x)\right]+\frac{1}{15\delta^7(\delta-1)x^5}\left[15\delta^7\left(\delta^2-1\right)x^7\right. \\
& +\delta^5\left(5\delta^2-21\right)x^5+30\delta^5\left(-3\delta^4+2\delta^2+1\right)x^4-15\delta^3\left(\delta^2-1\right)x^3 \\
& \left.+40\delta^7\left(3\delta^2-2\right)x^2-45\delta\left(\delta^2-1\right)x-45\delta^9+30\delta^7+6\delta^5+30\delta^3-45\delta\right].
\end{aligned}
\tag{4.130}
$$

All functions are only to be evaluated for $0 < x < 1$, as enforced by the Heaviside functions in (4.21), (4.22) and (4.23).

Chapter 5

Many Phonons and the Incoherent Approximation

5.1 Introduction

In this Chapter, we follow a generalization of the previous Chapter from the excitation of two phonons to n phonons in order to complete the multiphonon description. We employ the *incoherent approximation*, along with the harmonic approximation, to arrive at an analytic form of the coherent structure factor in terms of the simpler incoherent structure factor, whose differences were discussed in Chapter 3. We utilize the result of the incoherent approximation for phase space regimes where q is large ($q > q_{\rm BZ}$) or when the energy deposition requires at least two phonons to be excited. We follow by showing a matching of the single phonon result to DFT calculations, and making a comparison of the two phonon result to those of Chapter 4 applied to a toy model. We also show a matching onto the known impulse approximation and nuclear recoil results whose descriptions are valid at even larger energies and masses. We conclude by incorporating the n phonon description from the incoherent approximation to calculate DM-nucleon cross sections across the entire keV $\lesssim m_\chi \lesssim$ GeV mass ranges for both scalar and dark photon mediators. This completes the description of DM scattering in cubic crystal targets.

The relevant approximations are set primarily by the momentum transfer q. For single phonon excitations and $q < 2\pi/a$, where a is typical atomic lattice spacing, we use a long-

wavelength approximation used earlier in the literature [48, 44, 47, 42][1]. For $q > 2\pi/a$, we employ the incoherent approximation, which neglects interference effects between the response of neighboring atoms. This allows us to organize the calculation as a systematic expansion in the number of final state phonons, where each additional phonon comes with a factor of $q/\sqrt{2m_d\bar{\omega}_d}$. Here, m_d and $\bar{\omega}_d$ are the mass and average oscillation frequency of the atom in the position indexed by d. For $q < \sqrt{2m_d\bar{\omega}_d}$ it is numerically practical to compute the rate order-by-order in terms of the phonon density of states of the material. For $q \gg \sqrt{2m_d\bar{\omega}_d}$, scattering into many phonons dominates and the perturbation series requires increasingly large orders in $q/\sqrt{2m_d\bar{\omega}_d}$ to converge. It can however be resummed by making use of the impulse approximation, which in turn smoothly matches onto the free nuclear recoil regime. A similar expansion in number of modes has been performed previously for the integrable toy model that is the harmonic oscillator [73]. Here we have generalized the approach to a harmonic *crystal*, analogous to the procedure followed in [74] and [75], in calculations of the Migdal effect and X-ray backgrounds, respectively. Fig. 5.1.1 illustrates our results from applying these approximations. All of our calculations are implemented as part of the `DarkELF` public code [76].[2]

In analogue to the normalization used in the literature for DM-electron discussions, we normalize the structure factor slightly differently than in the previous Chapter. Using the unit cell volume Ω_c introduced in Chapter 3, we extract a factor in the differential cross section such that (2.9) instead reads

$$\frac{d\sigma}{d^3\mathbf{q}\,d\omega} = \frac{b_p^2}{\mu_\chi^2}\frac{1}{v}\frac{\Omega_c}{2\pi}|\tilde{F}(\mathbf{q})|^2 S(\mathbf{q},\omega)\,\delta\left(\omega-\omega_{\mathbf{q}}\right) \tag{5.1}$$

which likewise propagates through to multiplying the base normalization of $S(q,\omega)$ inversely by the factor $2\pi/\Omega_c$. This is only a difference in convention and has no effect on the predicted scattering rates or conclusions, as the two factors cancel.

[1] The bulk of Reference [42] is included in this Thesis in Chapter 4, however we leave the citations to the full paper when appropriate.

[2] https://github.com/tongylin/DarkELF

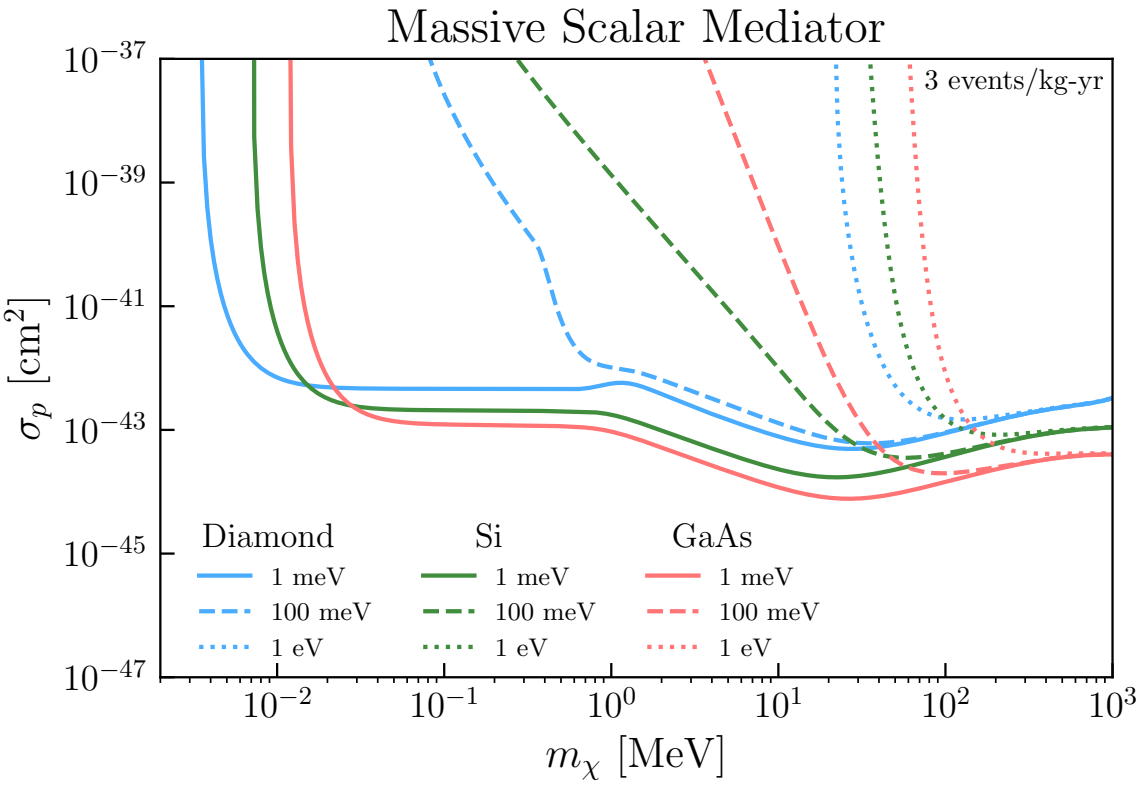

Figure 5.1.1. Cross sections needed for 3 events/kg-year for various target materials and threshold energies. A massive hadrophilic mediator is assumed.

5.2 Incoherent approximation

The incoherent approximation amounts to dropping the cross terms in ($\ell \neq \ell'$ or $d \neq d'$) from the sum in (3.9), thus neglecting the interference between non-identical atoms. In other words, one approximates the coherent structure factor by

$$S^{(\mathrm{coh})}(\mathbf{q},\omega) \approx \sum_{\ell}^{N} \sum_{d}^{\mathfrak{n}} (\overline{f_d})^2 \mathscr{C}_{\ell d}. \tag{5.2}$$

This is a good approximation when the momentum transfer is larger than $2\pi/a$ with a the inter-particle spacing. Then the phase factors associated with the interference terms are expected to add up to a small correction compared to the $\ell = \ell', d = d'$ terms in the sum. For an argument justifying (5.2) we refer to [40, 77].

For momentum transfers within the first Brillouin zone, single phonon scattering always dominates the inclusive scattering rate. It is however possible that the detector threshold is such that single phonon processes cannot be accessed but the double or multiphonon processes can. In this case the incoherent approximation cannot a priori be taken for granted. We nevertheless use it, but verify the results against our earlier two-phonon calculations [42] whenever possible (Sec. 5.3.2), finding satisfactory agreement. The accuracy of the calculations in this part of phase space is however less well understood and further work is needed.

To evaluate the auto-correlation function, we first replace the atomic positions $\mathbf{r}_{\ell d}$ in (3.10) with their displacement operator decomposition, noting that the $\ell + \mathbf{r}_d^0$ constant cancels, amounting to a simple substitution of $\mathbf{r}_{\ell d} \to \mathbf{u}_{\ell d}$:

$$\mathscr{C}_{\ell d} = \frac{1}{V} \int_{-\infty}^{\infty} dt \, \langle e^{-i\mathbf{q}\cdot\mathbf{u}_{\ell d}(0)} e^{i\mathbf{q}\cdot\mathbf{u}_{\ell d}(t)} \rangle e^{-i\omega t} \tag{5.3}$$

The expectation value may be rewritten with an application of the Baker–Campbell–Hausdorff

formula, Bloch's identity $\langle e^{\hat{A}} \rangle = e^{\frac{1}{2}\langle \hat{A}^2 \rangle}$, and some matrix algebra [44] giving:

$$\mathscr{C}_{\ell d} = \frac{1}{V} \int_{-\infty}^{\infty} dt\, e^{-2W_d(\mathbf{q})} e^{\langle \mathbf{q}\cdot\mathbf{u}_{\ell d}(0)\, \mathbf{q}\cdot\mathbf{u}_{\ell d}(t)\rangle} e^{-i\omega t}. \tag{5.4}$$

When we deployed Bloch's identity, we implicitly used the harmonic approximation, by only considering displacement operators of the form in (3.11). The correlator $\langle \mathbf{q}\cdot\mathbf{u}_{\ell d}(0)\, \mathbf{q}\cdot\mathbf{u}_{\ell d}(t)\rangle$ may be evaluated with the form of the displacement operator in (3.11), wherein the ℓ dependence cancels. This gives

$$\langle \mathbf{q}\cdot\mathbf{u}_d(0)\, \mathbf{q}\cdot\mathbf{u}_d(t)\rangle = \sum_{\nu}\sum_{\mathbf{k}} \frac{\left|\mathbf{q}\cdot\mathbf{e}_{\nu,\mathbf{k},d}\right|^2}{2Nm_d\omega_{\nu,\mathbf{k}}} e^{i\omega_{\nu,\mathbf{k}}t} \tag{5.5}$$

which can be simplified further by averaging over the direction of momentum vector $\mathbf{q}$

$$\langle \mathbf{q}\cdot\mathbf{u}_d(0)\, \mathbf{q}\cdot\mathbf{u}_d(t)\rangle \approx \frac{q^2}{3}\sum_{\nu}\sum_{\mathbf{k}} \frac{|\mathbf{e}_{\nu,\mathbf{k},d}|^2}{2Nm_d\omega_{\nu,\mathbf{k}}} e^{i\omega_{\nu,\mathbf{k}}t} \tag{5.6}$$

$$= \frac{q^2}{2m_d}\int_{-\infty}^{+\infty} d\omega' \frac{D_d(\omega')}{\omega'} e^{i\omega' t} \tag{5.7}$$

where we defined the *partial density of states* for each atom in the primitive cell as

$$D_d(\omega) \equiv \frac{1}{3N}\sum_{\nu}\sum_{\mathbf{k}} |\mathbf{e}_{\nu,\mathbf{k},d}|^2 \delta(\omega - \omega_{\nu,\mathbf{k}}). \tag{5.8}$$

The partial density of states was normalized to satisfy $\int_{-\infty}^{+\infty} d\omega D_d(\omega) = 1$. This can be shown by using the eigenvector completeness condition, which imposes $\sum_{\nu} e^*_{\nu,\mathbf{k},d,i} e_{\nu,\mathbf{k},d,j} = \delta_{ij}$ for fixed $\mathbf{k}, d$, where i, j are spatial indices. In addition, the total density of states of the material is defined by

$$D(\omega) \equiv \sum_d D_d(\omega) = \frac{1}{3N}\sum_{\nu}\sum_{\mathbf{k}} \delta(\omega - \omega_{\nu,\mathbf{k}}), \tag{5.9}$$

which satisfies $\int_{-\infty}^{+\infty} d\omega D(\omega) = \mathfrak{n}$ with $\mathfrak{n}$ the number of atoms in the unit cell.[3] In materials such as Ge, Si, or GaAs all atoms in the primitive cell have the same or similar mass and as such contribute roughly equally to the density of states, see Fig. 5.2.1. One could therefore approximate $D_d(\omega) \approx D(\omega)/\mathfrak{n}$ in (5.7) for these materials. We however choose to keep track of the partial density of states, to keep the calculations as general as possible.

For mono-atomic lattices, the density of states can be extracted directly from neutron scattering data through the incoherent structure factor. This is not always possible for multi-atomic lattices, since the scattering is only sensitive to the combination $\sum_d |\overline{f_d}|^2 D_d(\omega)/m_d$. To infer the individual $D_d(\omega)$ as well as $D(\omega)$, one therefore needs a set of scattering techniques which allows one to effectively vary the $\overline{f_d}$. This is not available for all materials, and it is therefore often most convenient to extract the $D_d(\omega)$ from DFT calculations. A comprehensive library of results has been made available by the materials project [6].

Returning now to the calculation of the autocorrelation function, we can expand the exponential term in (5.4) using the form of the correlator in (5.7). This yields an explicit representation of the incoherent correlator as an expansion in number of phonons n being excited:

$$\mathscr{C}_{\ell d} = \frac{2\pi}{V} e^{-2W_d(\mathbf{q})} \sum_n \frac{1}{n!} \left(\frac{q^2}{2m_d} \right)^n \left(\prod_{i=1}^{n} \int d\omega_i \frac{D_d(\omega_i)}{\omega_i} \right) \delta \left(\sum_j \omega_j - \omega \right) \tag{5.10}$$

where the delta function arises from the time integral $\frac{1}{2\pi} \int dt\, e^{i(\sum \omega_i)t} e^{-i\omega t}$ and ensures energy conservation. Here, by using (5.7), the Debye-Waller function takes the form of

$$W_d(\mathbf{q}) = \frac{q^2}{4m_d} \int d\omega' \frac{D_d(\omega')}{\omega'}. \tag{5.11}$$

Thus, in comparison to the difficulties discussed surrounding (3.12), inputting this form of the correlator into (5.2) gives an analytic approximation for all phonon terms in the appropriate

[3] In the literature, the density of states is also sometimes normalized to $3n_a$, where n_a is the atomic density.

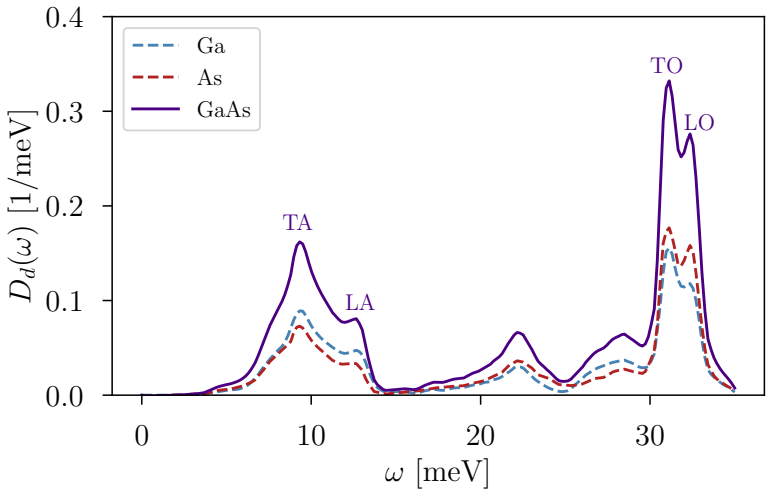

Figure 5.2.1. Partial and total density of states for GaAs [6]. Labels indicate the regions in which a particular phonon branch dominates.

regime of validity.

In this Chapter, we utilize the incoherent approximation to calculate the contributions from higher-order phonon terms to an arbitrary degree in a simple and fast manner. This allow us to make rate predictions for the entire relevant mass range, going from the low-mass ($m_\chi \gtrsim$ keV) single phonon regime to the high-mass ($m_\chi \gtrsim 50$ MeV) nuclear recoil regime.

5.3 Processes

Using the autocorrelation function, (5.10), for the coherent structure factor, we can estimate the scale at which a generic n-phonon term starts becoming a relevant contribution to scattering. To organize the multiphonon expansion, it is useful to define an average phonon energy

$$\overline{\omega}_d \equiv \int d\omega' \omega' D_d(\omega'). \tag{5.12}$$

While $\overline{\omega}_d$ technically depends on the atom d, this just gives an $\mathcal{O}(1)$ dependence in the phonon scale. Since $n! \propto n^n$ at large n, we see that the nth term of the series (5.10) will roughly begin

giving an $\mathcal{O}(1)$ contribution when

$$\frac{q^2}{2m_d\overline{\omega}_d} \sim n. \tag{5.13}$$

This means that for a given q (or consequently, m_χ) one can determine the dominant scattering processes. When $\frac{q^2}{2m_d\overline{\omega}_d} \lesssim 1$, single phonon excitations will be the primary channel; for $m_d \sim 30$ GeV and $\overline{\omega}_d \sim 30$ meV, this corresponds to $q \lesssim 30$ keV. Conversely, when $\frac{q^2}{2m_d\overline{\omega}_d} \gg 1$, phonons are no longer a suitable description and the scattering is instead well modeled by the recoil of a single nucleus. This transition occurs roughly at $q \gtrsim 2\sqrt{2m_d\bar{\omega}_d}$. In between these two extremes, we have $n \sim$ few, indicating multiphonon excitations as the primary process. The precise nature of the dominant process for a given m_χ will vary based on the mediator mass and experimental threshold.

In this section, we describe analytic approaches for characterizing the structure factor in crystal targets, broken into subsections corresponding to the previously mentioned processes. Secs. 5.3.1 and 5.3.2 deal with single phonon and two phonon excitations. Here we can also compare calculations of the full coherent structure factor with the incoherent approximation. Sec. 5.3.3 deals with many phonon excitations, and Sec. 5.3.4 describes the impulse approximation, which gives a good approximation to the structure factor for momenta approaching the nuclear recoil limit. For all numerical results in this section, we will assume a coupling to nucleons (replacing the generic average interaction strength $\overline{f_d}$ with the nucleon number A_d) for both massive and massless mediators, and take a GaAs target as a typical example of a cubic crystal of interest.

5.3.1 Single phonon production

As discussed in Sec. 3.1, DFT-based calculations for both single acoustic and single optical phonon excitations have been performed across a large dark matter mass range (∼keV to GeV) [44, 45, 46]. Meanwhile analytic calculations so far have been limited $q \lesssim 1$ keV, which

corresponds to $m_\chi \lesssim$ MeV [42, 48]. Although the DFT-based calculations span the entire mass range of interest and can provide information such as directional dependence, the numerics are more intensive; the phonon band structure, eigenvectors and structure factors must be calculated from first principles for each material. For high q, the sum over the reciprocal lattice must also be accounted for [49, 78]. Here we extend the analytic calculations to the high q regime by using the incoherent approximation. The comparison with the DFT results of [44] will also serve as a validation of the incoherent approximation.

To organize the calculations, it is useful to define a momentum scale ($q_{\rm BZ}$) which approximately reflects the size of the first Brillouin zone. We take $q_{\rm BZ} = \frac{2\pi}{a} \approx 2$ keV, where a is the lattice constant. We first review the single phonon response for $q < q_{\rm BZ}$. In this regime, we compute the structure factors in the isotropic approximation and in the limit $q \ll q_{\rm BZ}$. For this purpose we assume linear dispersions $\omega = c_s q$ for the longitudinal acoustic (LA) and transverse accoustic (TA) modes, with c_s replaced by $c_{\rm LA}$ and $c_{\rm TA}$ for the longitudinal and transverse sound speeds, respectively. The optical modes are assumed to have flat (constant) dispersions for the longitudinal optical (LO) and transverse optical (TO) phonon energies $\omega_{\rm LO}$ and $\omega_{\rm TO}$. The sound speeds and optical phonon energies are taken to be their long-wavelength values ($q = 0$). We will refer to this set of assumptions as the *long-wavelength approximation*.

The matrix element is given by the leading non-trivial term in the small q expansion of (3.13). The only relevant contributions for $q \ll q_{\rm BZ}$ are those of the single LA and LO phonons. Following the derivation of the single LA and LO phonon structure factors in (3.19)-(3.20), the total structure factor for $q < q_{\rm BZ}$ (following the normalization convention of this Chapter) is then

$$S_{n=1}^{(q<q_{\rm BZ})}(q,\omega) = \frac{2\pi}{\Omega_c} S_{n=1,\rm LA}(q,\omega) + \frac{2\pi}{\Omega_c} S_{n=1,\rm LO}(q,\omega) \tag{5.14}$$

with $\Omega_c = V/N$ the volume of the primitive cell.

For dark matter with a standard velocity dispersion $v \sim 10^{-3}$, the typical momentum transfer begins to fall outside the first Brillouin zone for $m_\chi \gtrsim 1$ MeV. Physically, this corresponds

to the wavelength becoming smaller than the interatomic spacing, and the long-wave length formulas from (3.16) to (3.20) are no longer valid. We can however utilize the incoherent approximation in (5.2) and (5.10), which yields

$$S_{n=1}^{(q>q_{\rm BZ})}(q,\omega) \approx \frac{2\pi}{\Omega_c}\sum_d^{\rm n} e^{-2W_d(q)}(\overline{f_d})^2\,\frac{q^2}{2m_d}\frac{D_d(\omega)}{\omega}. \tag{5.15}$$

The forms of the structure factor are qualitatively quite different in the two q regimes. In the coherent regime $q < q_{\rm BZ}$, summing over the response of multiple atoms with constructive interference leads to a resonant response in (5.14). The impact of the interference is greatly reduced for $q > q_{\rm BZ}$, such that the incoherent approximation becomes a viable description.

While the sharp transition in the structure factor is an artifact of our approximations, (5.14)-(5.15) can accurately describe the integrated structure factor above or below $q_{\rm BZ}$. Fig. 5.3.1 compares our combined analytic single phonon description with numerical DFT calculations. For the DFT result we follow [44], computing the dynamical matrix and phonon dispersions with respectively VASP [79] and phonopy [43] (see also [45]), and take the angular average of $S(\mathbf{q},\omega)$ over all $\mathbf{q}$ directions for comparison with the isotropic approximation. The top panels show the structure factors in (5.14) as a function of q, integrated over ω. The top left panel shows $S(q,\omega)$ integrated over $\omega \in [1\,\text{meV}, 27\,\text{meV}]$ to select the acoustic phonon branches only and the top right panel shows the integral over $\omega \in [27\,\text{meV}, 40\,\text{meV}]$ for optical phonon branches. The analytic approximations are in good agreement with the DFT result in their respective regimes of validity. For $q < q_{\rm BZ}$, integrating (5.14) leads to respectively $\sim q$ and $\sim q^4$ scaling, while the incoherent approximation in (5.15) always scales as $\sim q^2$. As discussed above, the ω-dependence of the analytic structure factors is quite different in the two regimes, with the coherent structure factor giving a resonant response around the single-phonon dispersion while the incoherent approximation is continuous in ω. However, the integrated result matches the full DFT calculation of the coherent structure factor well, indicating that the analytic approach will be useful in calculating integrated quantities such as rates. Furthermore, the analytic approach

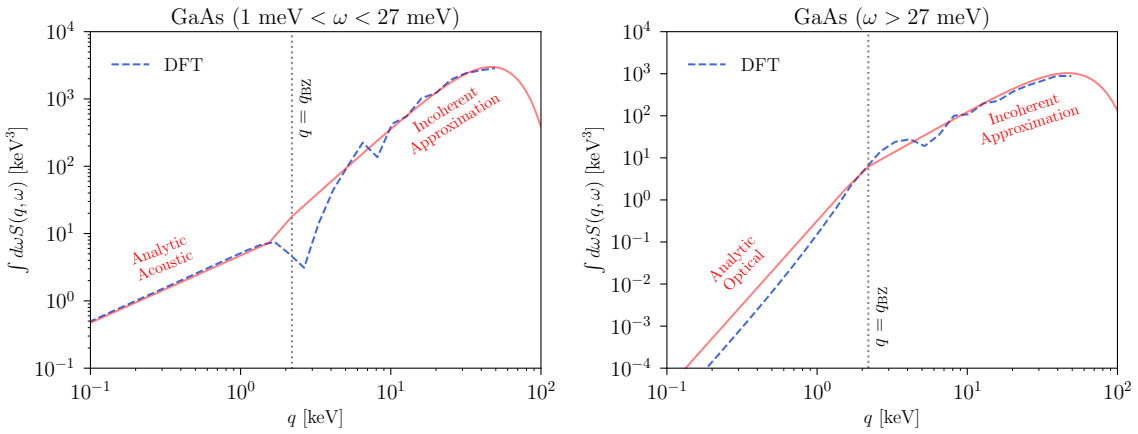

(a) Comparison of the integrated single phonon structure factor for GaAs. The left panel shows the structure factor integrated over $\omega = 1 - 27$ meV for acoustic phonon branches only and the right panel has $\omega = 27 - 40$ meV for optical phonon branches only. The dashed line shows the DFT result, averaged over all $\mathbf{q}$ directions, while the solid line shows our analytic approximation based on joining (5.14) (valid for $q < q_{\rm BZ}$) with the incoherent approximation (5.15) (valid for $q > q_{\rm BZ}$).

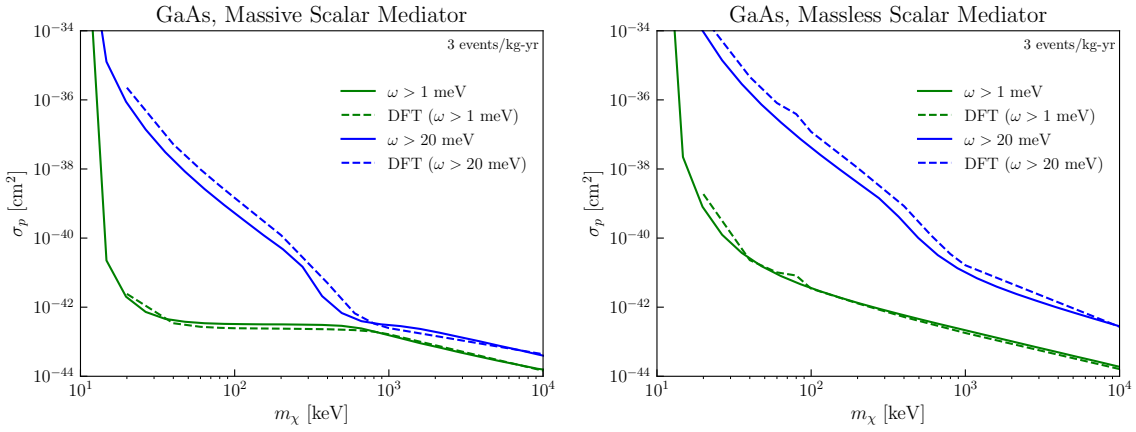

(b) Cross sections giving a rate of 3 events/kg-year, assuming $\overline{f_d} = A_d$.

Figure 5.3.1. Single phonon production.

provides physical insight into the change in the q-scaling of the structure factor in Fig. 5.3.1a.

The plots in Fig. 5.3.1b show single phonon integrated rates for both massive and massless scalar mediators. For the massless mediator, scattering into the acoustic phonon specifically favors small q due to the $\propto q^{-4}$ contribution of the mediator form factor. The analytic result of (3.19) therefore applies across the entire DM mass range, as the large q contributions are negligible. For all other cases the structure factor scales with a positive power of q so that large q contributions are the most important. We therefore see a change in slope of the σ_p reach around $m_\chi \sim$ MeV, when $q \gtrsim q_{\rm BZ}$ becomes kinematically accessible. These features are captured by the $q > q_{\rm BZ}$ analytic description from the incoherent approximation, and again agree with the DFT results.

5.3.2 Two-phonon production ($q < q_{\rm BZ}$)

We next turn to the use and accuracy of the incoherent approximation for two-phonon production, in particular for $q < q_{\rm BZ}$. Single phonon production always dominates in this regime if above threshold [42]. It is however expected that there will be a phase in the experimental program for which the energy threshold will still be too high to access single optical and accoustic phonons, such that the formally subleading double phonon production can be relevant.

While the incoherent approximation is expected to be the least accurate for $q < q_{\rm BZ}$, it is still useful to compare it with existing analytical results for the structure factor. The analytic results are obtained in the long-wavelength approximation, as defined in Sec. 5.3.1. In this limit, the Wilson coefficients of the self-interaction operators for the acoustic modes can be extracted from the measured or calculated elasticity parameters. With these assumptions, one can explicitly evaluate (3.12) to second order in $q/\sqrt{m_d \omega}$ [42].

In this Section, we will extend the long-wavelength calculations to all possible final states (see Appendix 5.A) and compare them with the incoherent approximation. For this purpose we extrapolate the results of Ref. [42] to higher q values and make a number of additional assumptions to model the self-interactions of the optical modes, thus giving the complete

structure factor. For these reasons the calculations in this section should however be considered only a toy model of a GaAs-like crystal. We will show below that for this toy model and in the limit of small momentum transfer, the incoherent and long-wavelength approximations give qualitatively similar DM scattering rates.

As described in the previous Chapter, the two-phonon structure factor can be written as

$$S(\mathbf{q},\omega) = S^{(\mathrm{harm})}(\mathbf{q},\omega) + S^{(\mathrm{anh})}(\mathbf{q},\omega) \tag{5.16}$$

in the long-wavelength limit. The first term is the structure factor in the harmonic limit (also referred to as the contact piece in [42]), where anharmonic corrections to the atomic potentials are neglected. It can be obtained by expanding (3.13) to second order, and evaluated analytically in the long-wavelength limit. The second term contains contributions to the structure factor from anharmonic interactions. In order to evaluate this, one needs to include a phonon self-interaction Hamiltonian in computing (3.13), as described in detail in [42]. The interactions of acoustic phonons are based on an effective three-phonon Hamiltonian valid in the long-wavelength limit, but to obtain a more complete picture we include a highly approximate three-phonon Hamiltonian for interactions involving optical phonons. These calculations are summarized in Appendix 5.A.

To perform the most meaningful comparison between the incoherent and long-wavelength approximations, we assume the following Debye model for the partial density of states for a diatomic crystal

$$\begin{aligned} D_{1,2}(\omega) = \frac{1}{q_{\mathrm{BZ}}^3}\frac{1}{A_1+A_2}\Bigg(& A_{1,2}\frac{\omega^2}{c_{\mathrm{LA}}^3}\Theta(c_{\mathrm{LA}}q_{\mathrm{BZ}}-\omega)\Theta(\omega) + A_{1,2}\frac{2\omega^2}{c_{\mathrm{TA}}^3}\Theta(c_{\mathrm{TA}}q_{\mathrm{BZ}}-\omega)\Theta(\omega) \\ & + A_{2,1}\frac{q_{\mathrm{BZ}}^3}{3}\delta(\omega-\omega_{\mathrm{LO}}) + A_{2,1}\frac{2q_{\mathrm{BZ}}^3}{3}\delta(\omega-\omega_{\mathrm{TO}})\Bigg). \end{aligned} \tag{5.17}$$

which is derived from the long-wavelength approximation as described in Sec. 5.3.1.[4] The

[4]Here the maximum momentum of the modes is determined by requiring that the sum over all momentum modes is equal to the total number of degrees of freedom. For the GaAs crystal structure and making an isotropic approximation, the momentum cutoff is strictly speaking about 2% different from $q_{\mathrm{BZ}} = 2\pi/a$. This error is

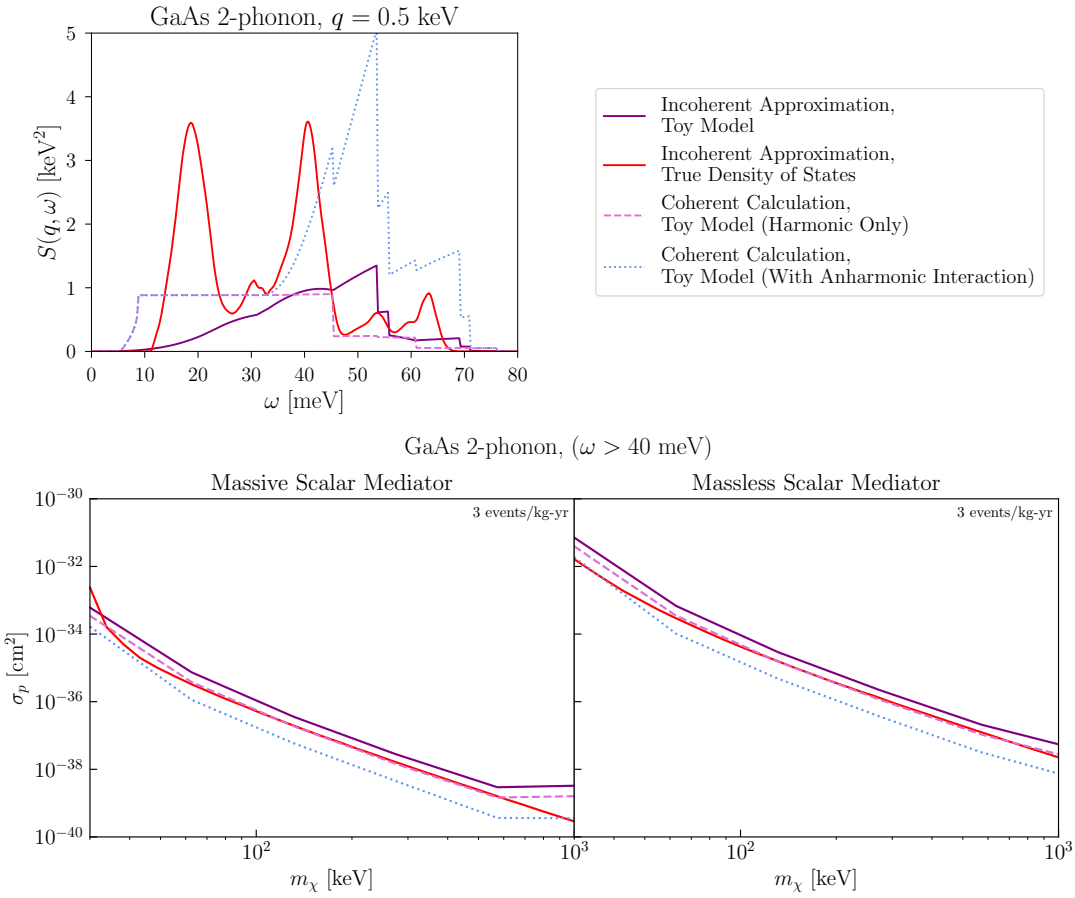

Figure 5.3.2. Two phonon production. *Top*: Comparison of the two-phonon structure factor calculated with various approximations, where the toy model assumes the long-wavelength approximation. Optical-optical channels give a δ-function and are not plotted. *Bottom*: Cross sections for producing two phonons at a rate of 3 events/kg-year using the same approximations as above. We restrict the mass range to $m_\chi \lesssim 1$ MeV so that typical q values are below $q_{\rm BZ}$, where our long-wavelength approximations are valid. The energy threshold is taken to be 40 meV, above the single phonon energies.

explicit structure factor from using this toy density of states in (5.10) is given in Appendix 5.A, which for simplicity we evaluate with $A_1 = A_2$ for GaAs.

The top panel of Fig. 5.3.2 compares the calculations of the two-phonon structure factor in the incoherent and long-wavelength approximations. For the incoherent approximation, we show the result with the toy density of states in (5.17) as well as with the true density of states from Fig. 5.2.1. The dashed line shows the harmonic limit, meaning that $S^{(\mathrm{anh})}$ is neglected. This is the case that is most directly comparable to the incoherent approximation, which assumes the harmonic mode expansion in (3.11). For the dotted line, the leading phonon self-interactions were included.

In the harmonic limit, all modes scale as $\sim q^4$ except for optical-acoustic final state, which scales as $\sim q^6$. The incoherent approximation naturally misses these more subtle destructive interference effects, but still captures the correct q^4 scaling for most of the modes. We see in Fig. 5.3.2 that the incoherent approximation is within a factor of ~ 5 of the long-wavelength approximation for all $\omega > \omega_{\mathrm{LO}}$, for both the toy model and true density of states. The difference at smaller ω is not experimentally relevant, as the single phonon rate will completely dominate in this region. There are also delta-function terms from the optical-optical branches which do not appear in the plot; their contributions to the overall scattering rate are comparable for the incoherent and long-wavelength approximations as well. See Appendix 5.A for details. These terms dominate the scattering rate at higher energies, and overall we see in Fig. 5.3.2 that the incoherent approximation reproduces the structure factor in the harmonic limit to within a factor of few.

When anharmonic interactions are included, the difference becomes larger and the incoherent approximation may under-predict the rate by up to an order of magnitude in our estimate. However, as discussed above, the anharmonic Hamiltonian used is itself also only valid at the order of magnitude level, particularly for optical modes. We expect that our approach can model the rate in this regime at the order-of-magnitude level, but a proper DFT calculation is

negligible compared to the uncertainties on the other assumptions we have made in this section.

needed for it to be rigorously validated.

Finally, we show in the bottom panel of Fig. 5.3.2 a comparison of the cross sections corresponding to a rate of 3 events/kg year, with the different approximations for the two-phonon structure factor. We assume $\omega > 40$ meV, since for lower thresholds the rate is dominated by single-phonon production [42]. We emphasize that here we are only illustrating that the incoherent approximation is within a factor of few of the full structure factor, as long as the same assumptions are made for the phonon dispersion relations. Therefore, we restrict our comparison to $m_\chi <$ MeV such that we can restrict to $q < q_{\rm BZ}$. The incoherent approximation underestimates the rate by a factor of few in the harmonic limit, and up to an order of magnitude when anharmonic interactions are included. Using the true density of states slightly improves the agreement. Though this comparison only applies to a limited q range, our result suggests that the incoherent approximation should give a reasonable, order-of-magnitude estimate for multiphonon production even at low q. We expect this uncertainty to decrease for larger q where the incoherent approximation is most justified, and in particular we will see that the incoherent approximation reproduces the expected rate in the free nuclear recoil limit, as discussed in the next sections.

5.3.3 Multiphonon production

In the previous section, where we dealt with $q < q_{\rm BZ}$, the incoherent approximation should be viewed as an order-of-magnitude estimate only. For $q > q_{\rm BZ}$, it is however on firm ground [40, 77] and is used routinely to measure the density of states from neutron scattering data [40]. Moreover, in the $q \gg q_{\rm BZ}$ regime multiphonon processes become important. This follows from the form of the structure factor, obtained by inserting (5.10) into the incoherent approximation (5.2):

$$S(\mathbf{q},\omega) \approx \frac{2\pi}{\Omega_c}\sum_d^{\rm n} (\overline{f_d})^2 e^{-2W_d(\mathbf{q})} \sum_n \left(\frac{q^2}{2m_d}\right)^n \frac{1}{n!}\left(\prod_{i=1}^n \int d\omega_i \frac{D_d(\omega_i)}{\omega_i}\right)\delta\left(\sum_j \omega_j - \omega\right). \quad (5.18)$$

From the discussion around (5.13), the typical number of phonons is $n \sim \frac{q^2}{2m_d\overline{\omega}_d}$. With $\overline{\omega}_d \gtrsim 30$ meV and $m_d \gtrsim 30$ GeV for most crystals, the self-consistency condition for the incoherent approximation ($q \gtrsim q_{\rm BZ}$) is therefore always satisfied for $n > 2$ processes. The evolution of (5.18) for increasingly large q is shown in Fig. 5.3.3a.

We can obtain an approximate scaling for (5.18) by separating each term in the sum over n into q-dependent and ω-dependent parts. The ω-dependent part is given by the second line of the equation, which is only non-zero at $\omega \lesssim n\,\omega_{\rm LO}$ in order to satisfy the delta function. This part of the structure factor can be estimated to have at most the value of $1/(n!\,\bar{\omega}_d^{n+1})$; this is illustrated in Fig. 5.C.1 of Appendix 5.C, where we plot the numerical result. For $q \lesssim \sqrt{2m_d\overline{\omega}_d}$ (left and center panels of Fig. 5.3.3a), the Debye-Waller factor can be neglected and the structure factor then scales as $S(q,\omega) \propto \sum_n \frac{1}{n!}\left(\frac{q^2}{2m_d\overline{\omega}_d}\right)^n$. For $q^2/(2m_d\overline{\omega}_d) \lesssim 1$, the structure factor therefore scales as $S(q,\omega) \sim q^{2m}$, with m the lowest number of phonons that is kinematically allowed. This scaling will be useful in Sec. 5.4, where we use it to extract the approximate scaling behavior of the DM cross section curves. It no longer holds for $q \gtrsim \sqrt{2m_d\overline{\omega}_d}$ (right-hand panel of Fig. 5.3.3a), where many modes contribute equally. This regime however can be understood in the impulse approximation, which is the subject of the next section.

5.3.4 The impulse approximation ($q \gg q_{\rm BZ}$)

For $q \gg q_{\rm BZ}$ the sum of the multiphonon terms asymptotes to an approximately Gaussian envelope, as can be seen most clearly from the rightmost panel in Fig. 5.3.3a. This asymptotic form can be derived directly with a steepest descent approximation, also known as the *impulse approximation*. It is valid whenever the interaction with the probe particle happens on a time scale short compared to that of the phonon modes.

To derive this, it is most insightful to take a step back from (5.18) and return to using

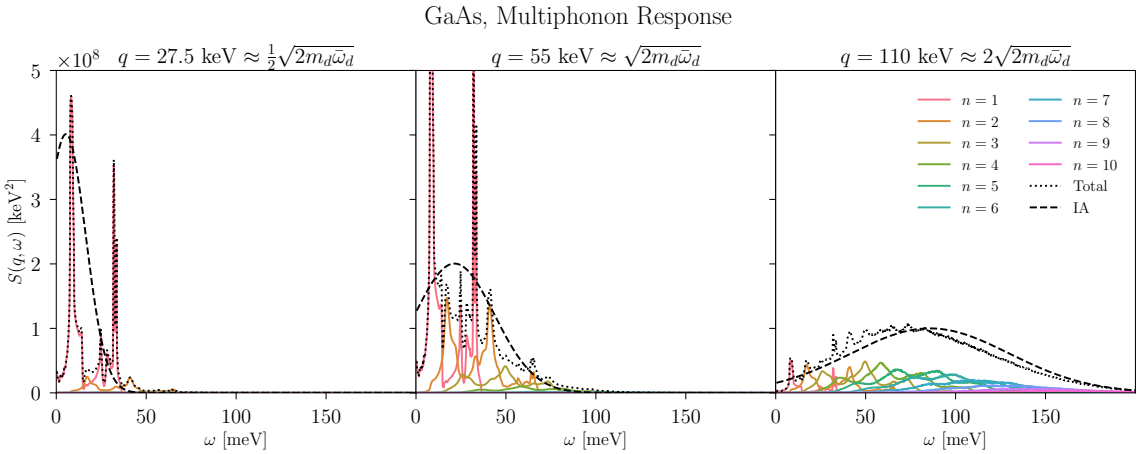

(a) The first ten phonon structure factors in the incoherent approximation for GaAs, plotted for various fixed q. At sufficiently large $q > \sqrt{2m_d\bar{\omega}_d}$, the total structure factor converges to the impulse approximation (IA, dashed line).

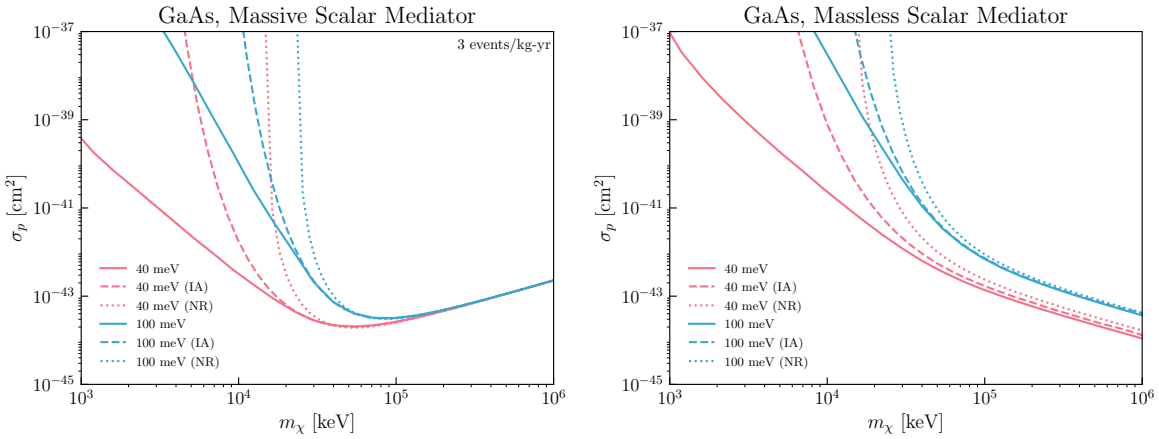

(b) Cross sections for 3 events/kg-yr in GaAs for a hadrophilic mediator. Rates are computed with the $n \leq 10$ phonon terms in the incoherent approximation (solid lines), the impulse approximation (IA; dashed), and the analytic free nuclear recoil result (NR; dotted). We see that at sufficiently high masses–and hence momentum transfers–the impulse approximation sufficiently recovers the result of summing the phonon terms. Likewise, for yet larger momenta the impulse approximation merges onto the free nuclear recoil result, as discussed in Sec. 5.3.4.

Figure 5.3.3. Multiphonon transition into the nuclear recoil regime.

(5.7) in (5.4). The auto-correlation function is then

$$\mathscr{C}_{\ell d} = \frac{1}{V} e^{-2W_d(\mathbf{q})} \int_{-\infty}^{\infty} dt\, e^{\frac{q^2}{2m_d}\int d\omega' \frac{D_d(\omega')}{\omega'} e^{i\omega' t}} e^{-i\omega t}. \tag{5.19}$$

When $q \gg \sqrt{2m_d\bar{\omega}_d}$, the exponent involving the density of states integral will be highly oscillatory in t, and the integral may be approximated by expanding about $t = 0$ through a steepest descent method. (See Appendix 5.B). Doing so gives

$$\mathscr{C}_{\ell d} \approx \frac{1}{V}\sqrt{\frac{2\pi}{\Delta_d^2}} \exp\left(-\frac{\left(\omega - \frac{q^2}{2m_d}\right)^2}{2\Delta_d^2}\right) \tag{5.20}$$

where $\Delta_d^2 \equiv \frac{q^2\bar{\omega}_d}{2m_d}$. This approximation is referred to as the impulse approximation since the saddle-point around $t = 0$ dominates the rate.

From (5.20), we see that the structure factor in the impulse approximation is

$$S^{\mathrm{IA}}(q,\omega) = \sum_d^{\mathrm{n}} \frac{(\overline{f_d})^2}{\Omega_c}\sqrt{\frac{2\pi}{\Delta_d^2}} \exp\left(-\frac{\left(\omega - \frac{q^2}{2m_d}\right)^2}{2\Delta_d^2}\right) \tag{5.21}$$

which is a sum of Gaussians peaked around $q = \sqrt{2m_d\omega}$, one for each atom in the unit cell. In Fig. 5.3.3a we see that (5.21) is a reasonable approximation for $q \approx \sqrt{2m_d\overline{\omega}_d}$ and converges rapidly to the full result in (5.18) for $q \gtrsim 2\sqrt{2m_d\overline{\omega}_d}$. As expected, it does not capture the features in the structure factor for $q \lesssim \sqrt{2m_d\overline{\omega}_d}$. In our final results, we use (5.21) for $q > 2\sqrt{2m_d\bar{\omega}_d}$, as it is numerically much faster than (5.18). For crystals composed of multiple inequivalent atoms, we define the boundary as $\max_d\left[2\sqrt{2m_d\bar{\omega}_d}\right]$. At this scale, the average number of phonons is about four, and it is sufficient to truncate the sum at $n = 10$ for all smaller q.

As we consider larger DM masses which access larger q and ω, the Gaussian becomes more sharply peaked. This can be seen by comparing the width Δ_d to the peak value $\omega = q^2/2m_d$.

In the large-q limit, we have

$$\lim_{q\to\infty} \frac{\Delta_d}{\omega} \approx \sqrt{\frac{\bar{\omega}_d}{\omega}} \tag{5.22}$$

so the Gaussian becomes narrow for ω well above the typical phonon energy. Then the narrow width limit exactly reproduces the expected free nuclear recoil delta function response:

$$\lim_{q,\,\omega\to\infty} \mathscr{C}_{\ell d} = \frac{2\pi}{V}\delta\left(\omega - \frac{q^2}{2m_d}\right) \tag{5.23}$$

$$S^{\mathrm{FR}}(q,\omega) = \sum_d \frac{2\pi}{\Omega_c}(\overline{f_d})^2\,\delta\left(\omega - \frac{q^2}{2m_d}\right). \tag{5.24}$$

We therefore recover the familiar free nuclear recoil response for each individual atom in the unit cell.

In Fig. 5.3.3b we show cross section curves with a GaAs target, for both massive and massless scalar mediators. We compare the reach obtained with the full structure factor (in the incoherent approximation), the impulse approximation, and the free nuclear recoil limit. For $m_\chi \lesssim 20-40$ MeV, the full structure factor must be used to capture the rate, depending on the mediator mass and threshold. For $m_\chi \gtrsim 20-40$ MeV, the q values compatible with the impulse approximation start to dominate, and we see that it reproduces the full result very closely. At even higher masses, the free nuclear recoil response becomes an excellent approximation, as expected.

A particular feature to notice from Fig. 5.3.3b is that the free nuclear recoil rate agrees with the impulse approximation result even in regions of the q, ω phase space where the Gaussian is not narrow. For example, for the massive mediator and $m_\chi = 50$ MeV, the rate will be dominated by momentum transfers $q \sim 2m_\chi v \sim 100$ keV, corresponding most closely to the rightmost panel of Fig. 5.3.3a. From (5.22) this gives $\Delta_d/\omega \approx 0.5$ which is not particularly small. The nuclear recoil approximation nevertheless works remarkably well. The reason is that phase space integral in (2.9) has a trivial ω dependence aside from the $S(\mathbf{q},\omega)$ factor, since the delta function in ω just determines the region of phase space that is integrated over. Therefore, as long

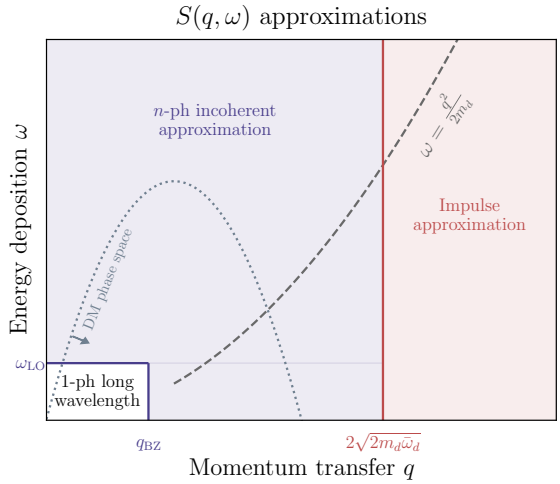

Figure 5.3.4. Schematic figure depicting the relevant regions of phase space and the corresponding approximation used to calculate the structure factors. The "1-ph long wavelength" regime is discussed in Sec. 5.3.1, the "n-ph incoherent approximation" regime in Sec. 5.3.2 and 5.3.3 and the "Impulse approximation" region in Sec. 5.3.4.

as the energy threshold is small compared to the peak in ω, the phase space integral over (5.21) and (5.24) yields similar answers.

5.3.5 Summary

Fig. 5.3.4 schematically illustrates the various approximations for the structure factor discussed in this section. The dotted gray parabola represents the phase space boundary for a given m_χ and v (see Sec. 5.4). This parabola extends upwards and rightwards as m_χ is increased, such that multiple different regimes are sampled for high enough m_χ.

For the single phonon excitations ($n = 1$) described in Sec. 5.3.1, we use the long-wavelength and incoherent approximations for $q < q_{\rm BZ}$ and $q > q_{\rm BZ}$, respectively. This combination gives good agreement with a full DFT calculation of the scattering rate, at least for a cubic crystal such as GaAs. For multiphonon excitations ($n \geq 2$), we use the incoherent approximation for the structure factor for all q below $\max_d[2\sqrt{2m_d\bar{\omega}_d}]$. This is motivated by Sec. 5.3.2, where we argued that the incoherent approximation can serve as an order-of-magnitude estimate even for $q \ll q_{\rm BZ}$. Given the limitations of the long-wavelength approximation, a dedicated DFT

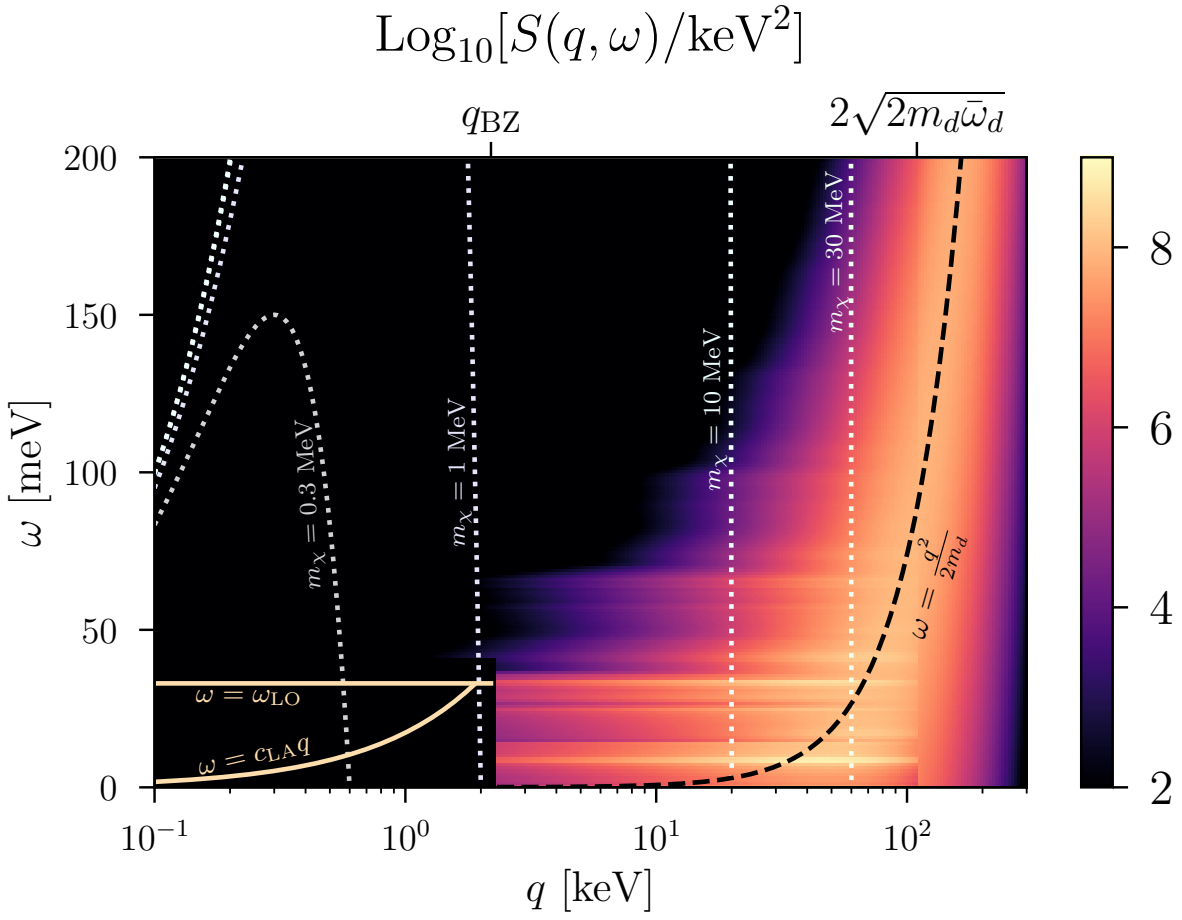

Figure 5.3.5. GaAs structure factor. Density plot of the structure factor in the same regimes of (q, ω) as shown in Fig. 5.3.4. Dotted lines are the phase space boundaries for various dark matter masses with a typical initial velocity $v = 10^{-3}$. At low momentum and energy transfers, the solid yellow lines are the dispersion relations of the single LA and LO phonons. At large q, the black dashed line is the free nuclear recoil dispersion relation; in general, there are separate lines for Ga and As but for clarity we show only one line corresponding to the average mass of Ga and As.

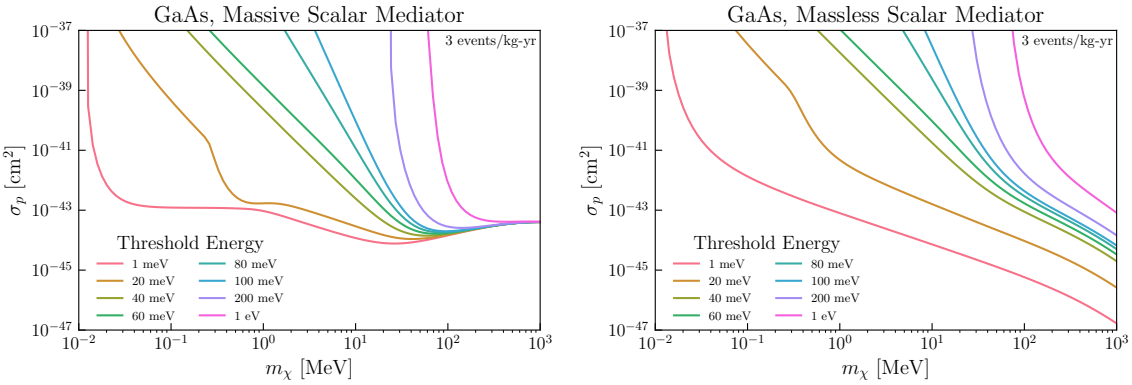

Figure 5.3.6. Cross section plots corresponding to a rate of 3 events/kg-yr for massive and massless scalar mediators in GaAs for various thresholds. The structure factors used are the analytic results demarcated in Fig. 5.3.4 for each corresponding regime in the (q, ω) phase space. For the massive mediator, we see the dominance of the single acoustic phonon at low masses and low thresholds, and of the optical phonon for intermediate thresholds. Eventually, for sufficiently high masses the process becomes dominated by the free nuclear recoil response. For the massless mediator, the q^{-4} form factor favors small momenta, and the rate is dominated by the lowest accessible mode for a given threshold.

calculation is needed in this regime. For multiphonon excitations, we sum terms in (5.18) until we achieve convergence, as explained in Sec. 5.3.3. Finally, for $q \geq \max_d[2\sqrt{2m_d\overline{\omega}_d}]$ we make use of the impulse approximation, which ultimately transitions into the well-known free nuclear recoil regime. This was explained in Sec. 5.3.4.

Fig. 5.3.5 shows our full calculation of the structure factor for GaAs, overlaid with the phase space boundaries for a few representative DM masses. In the low q, single phonon regime, the response is given by a set of δ-functions on the LO and LA phonon dispersions, represented by the orange curves. At intermediate and high q, the structure function is modeled by a continuous function, where the layered structure for $\omega \lesssim 50$ meV reflects the various single and multiphonon contributions. At higher q and ω the individual resonances cease to be visible and one transitions into the smooth $S(\mathbf{q}, \omega)$ predicted by the impulse approximation. At very high ω the structure function converges towards its free nuclear recoil form, which is represented by the black dashed line.

5.4 Results

In this section we convert our newly-gained understanding of the structure factor into concrete predictions for the DM scattering rate in a crystal target. The event rate per unit of target mass is

$$R = \frac{1}{\sum_d m_d} \frac{\rho_\chi}{m_\chi} \int d^3\mathbf{v}\, v f(\mathbf{v}) \int d^3\mathbf{q}\, d\omega \frac{d\sigma}{d\mathbf{q} d\omega} \tag{5.25}$$

where the experimental energy threshold is implicit in the boundary of the ω integral. $f(\mathbf{v})$ is the DM velocity distribution, which we take to be

$$\begin{aligned} f(\mathbf{v}) &= \frac{1}{N_0} \exp\left[-\frac{(\mathbf{v}+\mathbf{v}_e)^2}{v_0^2}\right] \Theta\left(v_{esc} - |\mathbf{v}+\mathbf{v}_e|\right), \\ N_0 &= \pi^{3/2} v_0^3 \left[\mathrm{erf}\left(\frac{v_{esc}}{v_0}\right) - 2\frac{v_{esc}}{v_0} \exp\left(-\frac{v_{esc}^2}{v_0^2}\right)\right], \end{aligned} \tag{5.26}$$

with $v_0 = 220$ km/s, the Earth's average velocity $v_e = 240$ km/s, and $v_{\rm esc} = 500$ km/s the approximate local escape velocity of the Milky Way. The scattering rate can be further simplified in the isotropic limit; using (2.9),

$$R = \frac{1}{4\pi\rho_T} \frac{\rho_\chi}{m_\chi} \frac{\sigma_p}{\mu_\chi^2} \int d^3\mathbf{v} \frac{f(\mathbf{v})}{v} \int_{q_-}^{q_+} dq \int_{\omega_{\rm th}}^{\omega_+} d\omega\, q |\tilde{F}(q)|^2 S(q,\omega) \tag{5.27}$$

where $\omega_{\rm th}$ is the energy threshold of the experiment, and the other integration limits[5] are

$$q_\pm \equiv m_\chi v \left(1 \pm \sqrt{1 - \frac{2\omega_{\rm th}}{m_\chi v^2}}\right) \tag{5.28}$$

$$\omega_+ \equiv qv - \frac{q^2}{2m_\chi}. \tag{5.29}$$

[5] In numerical implementations of (5.27), as done in `DarkELF`, it is beneficial to change the order of integrating by first carrying out the v integral, followed by the q integral and finally the ω integral.

Note (5.29) defines the phase space boundary shown in Fig. 5.3.4 for a given m_χ and v. Finally, ρ_T is the mass density of the target material and we have recast the rate in terms of the DM-proton scattering cross section $\sigma_p \equiv 4\pi b_p^2$.

5.4.1 Massive hadrophilic mediator

In the case of a massive mediator coupling to baryon number, we calculate the scattering rate by taking $\overline{f_d} = A_d$ and $\tilde{F}(q) = 1$. The cross sections corresponding to a rate of 3 events/kg-year exposure are shown in the left panel of Fig. 5.3.6, assuming a GaAs target and for different energy thresholds. The same figures for Si, Ge and diamond can be found in Appendix 5.D.

We can understand the numerical results in Fig. 5.3.6 analytically using the scaling of the structure factor discussed in Secs. 5.3.1–5.3.4. First, from (5.27), the m_χ dependence of the rate is contained in

$$R \propto \frac{\sigma_p}{m_\chi \mu_\chi^2} \int_{q-}^{q+} dq \int_{\omega_{\rm th}}^{\omega_+} d\omega\, q\, S(q,\omega). \tag{5.30}$$

The structure factor only contains positive powers of q across the entire phase space, so for a massive mediator, the integral (5.30) will be dominated by the largest kinematically accessible momentum transfers.

For $m_\chi \gg 30$ MeV, the kinematically allowed phase space is extended to q and ω where the free nuclear recoil approximation can be used. The rate therefore approximately scales as $R \sim 1/m_\chi$ for $m_p \gtrsim m_\chi \gg 30$ MeV. For low enough thresholds, this scaling holds even as the dark matter mass comes within $O(\text{few})$ of 30 MeV, where the structure factor is relatively broad in ω. The reason is that the kinematically allowed phase space is wide enough in ω that the integral over the Gaussian in the impulse approximation gives within a factor of few of the integral over the delta function in (5.24), as discussed earlier in Sec. 5.3.4.

For dark matter masses of 1 to 30 MeV, the allowed phase space is restricted to values of $q < \sqrt{2m_d\bar{\omega}}$. Here the structure factor can be expanded in powers of $q/\sqrt{2m_d\bar{\omega}}$ and favors small ω. As noted in Sec. 5.3.3 the structure factor scales as $\sim q^{2m}$, with m the smallest number of

phonons whose total energy is above the energy threshold. We see there is significant threshold dependence: the single phonon final state strongly dominates the rate if it is above the energy threshold, while for higher thresholds only multiphonons contribute. The rate integral now scales as

$$R \propto \frac{\sigma_p}{m_\chi^3} \int^{2m_\chi v} dq\, q^{2m+1} \int_{\omega_{\rm th}} d\omega \propto \sigma_p\, m_\chi^{2m-1}, \tag{5.31}$$

where q was evaluated at its maximum $q \sim 2m_\chi v$. The ω integral does not contribute to the m_χ scaling of the rate, since the integrand is peaked in ω somewhere near the energy threshold $\omega_{\rm th}$. This expression then gives the approximate scaling $R \propto m_\chi^{2m-1}$. Since m is dependent on the energy threshold, this explains why different thresholds in Fig. 5.3.6 result in a different scaling as a function of m_χ.

At even lower dark matter masses ($m_\chi < 1$ MeV), the phase space is restricted to q values within the first Brillouin zone, which is dominated by single phonon production in the long wavelength regime. If the threshold is low enough to access a single phonon, the scaling further depends on whether the threshold captures an appreciable part of the LA branch. If so, the leading contribution comes from the acoustic mode (3.19), which gives

$$R \propto \frac{\sigma_p}{m_\chi^3} \int^{2m_\chi v} dq\, q^2 \int d\omega\, \delta(\omega - c_{\rm LA} q) \propto \sigma_p, \tag{5.32}$$

approximately independent of m_χ. This behavior is clearly reproduced in Fig. 5.3.6 for the 1 meV threshold, for which the acoustic branch is always accessible. If the threshold is too high to access the acoustic branch, but can detect the optical branch, the structure factor has an extra q^3 scaling and we find $R \propto m_\chi^3$. This case occurs for $m_\chi \lesssim 0.3$ MeV on the 20 meV curve in Fig. 5.3.6. For $m_\chi \gtrsim 0.3$ MeV the DM can excite the acoustic branch, resulting in a sharp enhancement of the rate.

5.4.2 Massless hadrophilic mediator

If we instead have a massless mediator that couples to baryon number, then by convention, the mediator form factor is taken to be $|\tilde{F}(q)|^2 = \left(\frac{m_\chi v_0}{q}\right)^4$ with $v_0 = 220$ km/s. The cross section curves for this scenario are given in the right panel of Fig. 5.3.6 again for different thresholds.

As in Sec. 5.4.1, we can analytically explain the scaling of the different curves across the DM mass range. The main difference with the massive mediator case is that for a massless mediator, there is a $1/q^4$ scaling in the form factor, which leads to a scattering rate that generally favors low q and ω. The main contribution to the rate will therefore be much more threshold dependent across all DM masses. If the threshold is small enough to access single acoustic phonon excitations, then this will be the dominant contribution to the rate at all masses. Again from (5.27) and using the analytic acoustic structure factor, the rate for thresholds that are sensitive to a single acoustic phonon scales as

$$R \propto \sigma_p m_\chi \int_{\omega_{\rm th}/c_{\rm LA}} dq \frac{1}{q^2} \int d\omega\, \delta(\omega - c_{\rm LA} q). \tag{5.33}$$

The integrand is largest at the smallest q, so we estimate the q integral by evaluating the integrand at $q \approx \omega_{\rm th}/c_{\rm LA}$ in (5.28). The integrand therefore has no m_χ dependence and gives the scaling $R \propto m_\chi$ for the $\omega > 1$ meV curve in Fig. 5.3.6. Note however that this scaling behavior is sensitive to our convention for the reference momentum in $\tilde{F}(q)$. For example, in models with both electron and nucleon couplings one often chooses to normalize the form factor with the reference momentum $q_0 = \alpha m_e$, which would yield $R \propto m_\chi^{-3}$.

If the LA branch is not accessible but the LO branch is, the production of a single LO mode will generally dominate. This introduces a different m_χ dependence, which can be seen in Fig. 5.3.6 by comparing the 1 meV and 20 meV curves in the region with $m_\chi \lesssim 30$ MeV. If

$m_\chi < 1$ MeV, using the expression in (3.20) gives

$$R \propto \sigma_p m_\chi \int^{2m_\chi v} dq\, q \int d\omega\, \delta(\omega - \omega_{LO}). \tag{5.34}$$

Unlike for the acoustic phonon, the structure factor favors high q so that the largest contribution is near $q \sim 2m_\chi v$, giving $R \propto m_\chi^3$. If $m_\chi > 1$ MeV, the rate integrand is dominated by momentum transfers $q \sim q_{\rm BZ}$. This is because when $q > q_{\rm BZ}$ and $\omega \leq \omega_{\rm LO}$ we are using the incoherent approximation for single phonon production, where the q integrand drops as q^{-1}. Thus, we estimate the rate by integrating up to $q_{\rm BZ}$ only:

$$R \propto \sigma_p m_\chi \int^{q_{\rm BZ}} dq\, q \int d\omega\, \delta(\omega - \omega_{LO}), \tag{5.35}$$

and find that $R \propto m_\chi$. This is the reason why the 20 meV curve in Fig. 5.3.6 changes slope around $m_\chi \sim 1$ MeV.

We next turn to the intermediate mass range ($1 - 30$ MeV) with $\omega_{\rm th} > \omega_{\rm LO}$, such that $n \geq 2$ phonons. In Fig. 5.3.6 this corresponds to the curves with thresholds of 40 meV and above. As in Sec. 5.4.1, we again notice that the leading contribution to the structure factor will be given by the smallest number of phonons, m, that can exceed the threshold energy. In this regime, the integrand $\propto S(q,\omega)/q^3$ scales with positive powers of q for $m \geq 2$ phonons, since (5.10) grows faster than q^3. The analysis for multiphonons then follows exactly the same logic as the discussion in the previous section and we find that $R \propto m_\chi^{2m-1}$.

For large dark matter masses ($\gg 30$ MeV), again if the threshold is well above the single phonon energy, we can apply the free nuclear recoil approximation to obtain the scaling. Using the free nuclear structure factor gives

$$R \propto \frac{\sigma_p}{m_\chi^3} \int_{\sqrt{2m_d\omega_{\rm th}}} dq\, q \Big(\frac{m_\chi v_0}{q}\Big)^4 \int d\omega\, \delta\big(\omega - \frac{q^2}{2m_d}\big). \tag{5.36}$$

The q-integral is dominated by low-momentum transfers along the free nuclear recoil dispersion, so we evaluate the integral at the intersection of $\omega = \omega_{\rm th}$ and $\omega = \frac{q^2}{2m_d}$, or $q = \sqrt{2m_d\omega_{\rm th}}$. Then, the approximate scaling in this regime is $R \propto m_\chi/\omega_{\rm th}$, which we verify numerically in Fig. 5.3.6.

5.4.3 Dark photon mediators

The defining feature of a dark photon mediator is that it couples to the electric charge of the SM particles. In the regime where phonons are the relevant degrees of freedom, the charge of the nucleus is (partially) screened by the electrons. This means that we need a notion of an *effective charge*, as seen by the DM, which is momentum dependent. For individual atoms, this effective charge interpolates between zero in the low momentum, fully screened regime and the nuclear charge in the high momentum regime. We use the calculations from Brown et. al. [7] of the effective charge for individual atoms, as shown in Fig. 5.4.1. We expect this approximation to hold only for $q \gtrsim q_{\rm BZ}$, since additional many-body effects should be relevant for $q < q_{\rm BZ}$. This is particularly true for a polar material such as GaAs, where the Born effective charge of the Ga and As atoms is non-zero in the $q \to 0$ limit. In this regime a full DFT calculation of the momentum dependence of the effective charge is needed, which we do not attempt here. In this Section, we will therefore focus on the momentum regime $q \gtrsim q_{\rm BZ}$, which corresponds to $m_\chi \gtrsim$ MeV. In this case we can use the incoherent approximation and take $\bar{f}_d = Z_d(q)$, with $Z_d(q)$ the atomic effective charges in Fig. 5.4.1. This allows us to compute scattering rates with dark photon mediators for the production of two or more phonons, which is dominated by the highest kinematically accessible momentum transfers.

The regime $q < q_{\rm BZ}$ is relevant primarily for massless dark photon mediators. (For massive dark photon mediators, there are strong BBN constraints that severely limit the scattering rate for sub-MeV dark matter, see e.g. [58].) In this regime, there are substantial deviations from the atomic effective charges due to the delocalized nature of the valence electrons. For instance, a polar material such as GaAs, SiC and sapphire can have a residual dipole moment associated with atomic displacements even for $q \to 0$. The effective couplings $\bar{f}_d$ in this limit

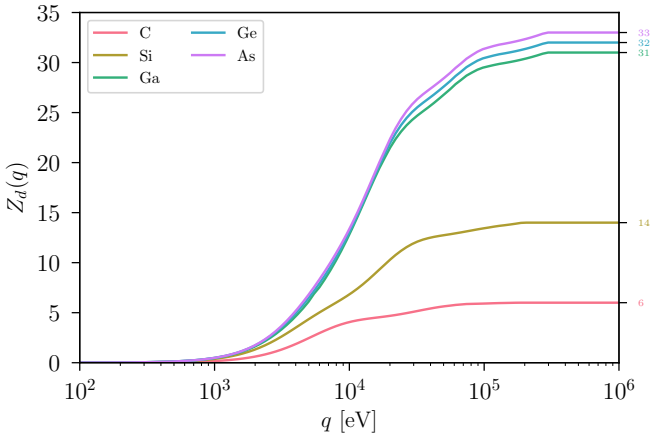

Figure 5.4.1. Momentum dependence of the effective ion charge for atomic elements, as computed in [7].

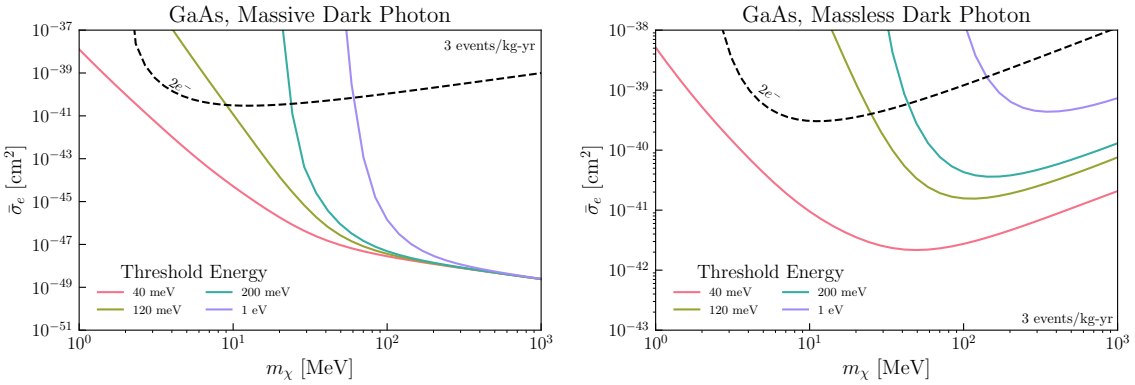

Figure 5.4.2. Cross section plots for a rate of 3 events/kg-year in GaAs, for massive and massless dark photon mediators. For comparison, the dashed black lines represent the cross sections required for DM-electron scattering with a $2e^-$ ionization threshold with the same exposure, as computed using `DarkELF` [76].

are given by Z_d^*/ε_∞, where Z_d^* is the Born effective charge and ε_∞ is a screening due to valence electrons; the Born effective charges can be calculated with DFT methods [44, 45, 78]. This was treated in previous studies of single-phonon production through a massless dark photon mediator [48, 44, 49, 47, 45, 80, 78, 46]. For non-polar materials such as Si, Ge and diamond, the Born effective charges vanish and instead multiphonon production is expected to dominate. This can be estimated with the energy loss function [76], at least for sub-MeV dark matter. Since this $q < q_{\rm BZ}$ regime is already included in `DarkELF` [76], we restrict our results here to multiphonon processes with $q > q_{\rm BZ}$ and $\omega > \omega_{\rm LO}$.

Our results are shown in Fig. 5.4.2 for GaAs; the results for Ge, Si and diamond are deferred to Appendix 5.D. As is conventional for dark photon mediators, we choose the reference momentum for the massless mediator to be $q_0 = \alpha m_e$ and present the results in terms of the effective DM-electron cross section $\bar{\sigma}_e$ [81], with

$$\bar{\sigma}_e = \frac{\mu_{\chi e}^2}{\mu_\chi^2}\sigma_p \tag{5.37}$$

and $\mu_{\chi e}$ the DM-electron reduced mass. In our calculations using the atomic effective charges, we impose $q > q_{\rm BZ}$ to ensure we are not sampling the area of phase space for which these charges are clearly invalid. This means that our rate calculations for $m_\chi \lesssim 10$ MeV are a slight underestimate of the true result.

5.5 Conclusions and outlook

It is well-known that DM scattering in crystals can lead to one or more phonons being produced if DM has MeV-scale mass, as well as a recoiling nucleus if DM has GeV or higher mass. These processes are two sides of the same coin, depending on whether the momentum transfer is comparable to the inverse of the interparticle spacing and whether the energy deposition is comparable to the typical phonon energy $\sim \bar{\omega}$. When both momentum and energy scales are small, single phonon production dominates, and when both are large, nuclear recoils dominate.

Here we studied the intermediate regime which is dominated by many phonons, which allows us to smoothly interpolate between single phonon production and nuclear recoils (see Fig. 5.3.6).

To make the multiphonon calculation tractable, we relied on the isotropic, incoherent, and harmonic crystal approximations. This allowed us to obtain analytic results for the scattering rate in terms of the phonon density of states in the crystal. These approximations are expected to be very good for $q \gg q_{\rm BZ}$ ($m_\chi \gg 1$ MeV), as they explicitly reproduce the nuclear recoil limit when $q \gg \sqrt{2 m_N \bar{\omega}}$. For $q \lesssim q_{\rm BZ}$ ($m_\chi \lesssim 1$ MeV) the experimental threshold determines which theoretical treatment is most appropriate: for single phonon production, one can obtain analytic formulas by instead using a long wavelength, isotropic approximation. These results are currently only valid for cubic crystals such GaAs, Si, Ge and diamond. For strongly anisotropic materials such as sapphire, one must find a way to generalize them further or rely on DFT calculations. For multiphonon production and $q \lesssim q_{\rm BZ}$, the situation is more complicated: in this case it cannot be taken for granted that anharmonic corrections to the various multiphonon channels can be neglected. The anharmonic multiphonon contributions involving optical modes are particularly difficult to model analytically, and at the moment we perform a simple estimate in a toy model to justify extrapolating the incoherent and harmonic approximations to $q \lesssim q_{\rm BZ}$. A dedicated DFT calculation is needed to improve their accuracy.

Our approach provides a smooth description of sub-GeV dark matter scattering down to keV masses for hadrophilic mediators. For dark photon mediators, a DFT calculation of the momentum-dependent couplings in the $q \sim q_{\rm BZ}$ regime is needed to complete the interpolation. For both mediators, we have provided results for multiple direct detection materials of interest, and also included our calculation as part of the `DarkELF` public code package. These will be essential to interpret direct detection results as experimental thresholds for calorimetric detectors reach the eV scale and lower.

Acknowledgements

We are grateful to So Chigusa, Sinéad Griffin, Bashi Mandava and Mukul Sholapurkar for useful discussions. BCD, TL, and EV were supported with Department of Energy grants DE-SC0019195 and DE-SC0022104, as well as a UC Hellman fellowship. SK was supported by the Office of High Energy Physics of the U.S. Department of Energy under contract DE-AC02-05CH11231. EV is supported by a Sloan Scholar Fellowship.

This chapter, in full, is a reprint of the material as it appears in Brian Campbell-Deem, Simon Knapen, Tongyan Lin, and Ethan Villarama, Dark matter direct detection from the single phonon to the nuclear recoil regime, Phys.Rev. D **106** (2022) no.6, 036019. The dissertation author was one of the primary investigators and authors of this paper.

Appendices

5.A Two phonon analytic structure factors

In Sec. 5.3.2 we compared the long-wavelength and incoherent approximations for the two-phonon final states, for q within the first BZ. In this appendix we provide the analytic expressions for both approximations.

5.A.1 Long-wavelength approximation

Here we discuss how we extend the analytic calculations from [42] for the coherent two-phonon structure factor to additional combinations of final state phonon pairs. As in Sec. 5.3.2, we assume a hadrophilic mediator with $\overline{f_d} = A_d$ throughout this appendix. It was shown in [42] that the structure factor separates into harmonic and anharmonic contributions

$$S(\mathbf{q},\omega) = S^{(\mathrm{harm})}(\mathbf{q},\omega) + S^{(\mathrm{anh})}(\mathbf{q},\omega) \tag{5.38}$$

which do not interfere at leading order in the long wavelength limit. The first term involves expanding (3.12) to second order; note that it was referred to as the contact term in [42]. The anharmonic term is computed using an anharmonic phonon interaction Hamiltonian to first order. The specific matrix elements to be used are given in equations (12) and (13) of [42]. We take the long-wavelength approximation for the phonon modes, as described in Sec. 5.3.1. For a crystal

with two atoms in the unit cell, the longitudinal eigenvectors can be approximated by

$$\mathbf{e}_{\mathrm{LA},\mathbf{k},1} \approx \frac{\sqrt{A_1}}{\sqrt{A_1+A_2}}\hat{\mathbf{k}}, \tag{5.39}$$

$$\mathbf{e}_{\mathrm{LA},\mathbf{k},2} \approx \frac{\sqrt{A_2}}{\sqrt{A_1+A_2}}e^{-i\mathbf{k}\cdot\mathbf{r}_2^0}\hat{\mathbf{k}} \tag{5.40}$$

$$\mathbf{e}_{\mathrm{LO},\mathbf{k},1} \approx \frac{\sqrt{A_2}}{\sqrt{A_1+A_2}}\hat{\mathbf{k}}, \tag{5.41}$$

$$\mathbf{e}_{\mathrm{LO},\mathbf{k},2} \approx -\frac{\sqrt{A_1}}{\sqrt{A_1+A_2}}e^{-i\mathbf{k}\cdot\mathbf{r}_2^0}\hat{\mathbf{k}}. \tag{5.42}$$

with $\hat{\mathbf{k}}$ the unit vector along the phonon propagation direction. Note that the $\mathbf{r}_2^0$ dependence was neglected in the LA eigenvector in (3.16) and in [42]; here we have kept this additional phase so that the acoustic and optical eigenvectors are explicitly orthogonal across a unit cell. This additional phase factor will only be relevant in cases where there is a destructive interference in the leading coupling to acoustic phonons, which occurs for some final states [47]. The transverse eigenvectors lay in the plane perpendicular to $\hat{\mathbf{k}}$ and have analogous normalizations.

Analytic expressions for the harmonic structure factor were provided in Ref. [42] for acoustic-acoustic final states only. We require expressions for the optical-optical and optical-acoustic final states as well to perform the comparison with the incoherent approximation. A straightforward application of (16) in [42] to the lowest order in q gives

$$\begin{aligned}
S^{(\mathrm{harm})}_{\mathrm{LOLO}} &= \frac{2\pi}{\Omega_c}\frac{\pi q^4}{120 m_p^2 \omega_{\mathrm{LO}}^2}\delta(\omega - 2\omega_{\mathrm{LO}}) \\
S^{(\mathrm{harm})}_{\mathrm{LOTO}} &= \frac{2\pi}{\Omega_c}\frac{\pi q^4}{90 m_p^2 \omega_{\mathrm{LO}}\omega_{\mathrm{TO}}}\delta(\omega - (\omega_{\mathrm{LO}} + \omega_{\mathrm{TO}})) \\
S^{(\mathrm{harm})}_{\mathrm{TOTO}} &= \frac{2\pi}{\Omega_c}\frac{\pi q^4}{45 m_p^2 \omega_{\mathrm{TO}}^2}\delta(\omega - 2\omega_{\mathrm{TO}})
\end{aligned} \tag{5.43}$$

for the optical-optical modes.

For the optical-acoustic modes, the harmonic structure factors are of the form

$$S^{(\text{harm})}_{\text{LOLA}} = \frac{2\pi}{\Omega_c} \frac{a^5}{2304\pi^2 c_{\text{LA}}^2 m_p^2 \omega_{\text{LO}}} \frac{A_1 A_2}{(A_1+A_2)^2} \left(\frac{\omega - \omega_{\text{LO}}}{c_{\text{LA}}} \right)^7 g^{(\text{harm})}_{\text{LOLA}}(x)\, \Theta(c_{\text{LA}} q_{\text{BZ}} - (\omega - \omega_{\text{LO}})),$$

where $x \equiv \frac{c_{\text{LA}} q}{\omega - \omega_{\text{LO}}}$. The other structure factors for optical-acoustic final states are given by relabelings LO $\to$ TO, LA $\to$ TA, where the expressions g expanded at small q are

$$\begin{aligned}
g^{(\text{harm})}_{\text{LOLA}}(x \ll 1) &\approx \frac{3}{10}x^6 - \frac{1}{7}x^8 + \frac{1}{15}x^{10} \\
g^{(\text{harm})}_{\text{LOTA}}(x \ll 1) &\approx \frac{1}{5}x^6 + \frac{12}{35}x^8 - \frac{4}{105}x^{10} \\
g^{(\text{harm})}_{\text{TOLA}}(x \ll 1) &\approx \frac{1}{5}x^6 + \frac{1}{7}x^8 - \frac{1}{15}x^{10} \\
g^{(\text{harm})}_{\text{TOTA}}(x \ll 1) &\approx \frac{4}{5}x^6 - \frac{12}{35}x^8 + \frac{4}{105}x^{10}.
\end{aligned} \tag{5.44}$$

We see that at leading order in small q, the optical-acoustic structure factors are all suppressed by an additional factor of q^2 relative to the optical-optical modes, which is due to destructive interference. Since we will be comparing with the incoherent approximation at small q, we can effectively neglect these final states.

We would also like to compute the anharmonic contributions to the 2-phonon structure factor, which we do with the inclusion of an anharmonic interaction Hamiltonian. For acoustic phonons in the long-wavelength limit, we have an effective Hamiltonian for acoustic phonons where the interactions are given in terms of macroscopic properties of the crystal through the Lamé parameters, as described in [42]. For the interactions of optical phonons, however, it is more difficult to write down a reliable analytic Hamiltonian. In this case we use (45) of Ref. [42], which comes from [82]. This Hamiltonian should be taken only at the order-of-magnitude level. We restrict the use of both effective Hamiltonians to the first BZ. The analytic expressions for the acoustic-acoustic and acoustic-optical final states are given already, so we complete this by

calculating the optical-optical terms. At leading order in q, this gives

$$\begin{aligned}
S^{(\mathrm{anh})}_{\mathrm{LOLO}} =& \frac{2\pi}{\Omega_c}\frac{\pi}{6m_p^2}\frac{c_{\mathrm{LA}}^2}{\bar{c}^2}\frac{\omega_{\mathrm{LO}}^2 q^4}{((2\omega_{\mathrm{LO}})^2-(c_{\mathrm{LA}}q)^2)^2} \\
&\times \delta(\omega - 2\omega_{\mathrm{LO}}) \\
S^{(\mathrm{anh})}_{\mathrm{LOTO}} =& \frac{2\pi}{\Omega_c}\frac{2\pi}{3m_p^2}\frac{c_{\mathrm{LA}}^2}{\bar{c}^2}\frac{\omega_{\mathrm{LO}}\omega_{\mathrm{TO}} q^4}{((\omega_{\mathrm{LO}}+\omega_{\mathrm{TO}})^2-(c_{\mathrm{LA}}q)^2)^2} \\
&\times \delta(\omega - \omega_{\mathrm{LO}} - \omega_{\mathrm{TO}}) \\
S^{(\mathrm{anh})}_{\mathrm{TOTO}} =& \frac{2\pi}{\Omega_c}\frac{2\pi}{3m_p^2}\frac{c_{\mathrm{LA}}^2}{\bar{c}^2}\frac{\omega_{\mathrm{TO}}^2 q^4}{((2\omega_{\mathrm{TO}})^2-(c_{\mathrm{LA}}q)^2)^2} \\
&\times \delta(\omega - 2\omega_{\mathrm{TO}}),
\end{aligned} \tag{5.45}$$

where $\bar{c} \equiv (c_{\mathrm{LA}} + c_{\mathrm{TA}})/2$. We have also assumed that the Grüneisen constant $\gamma_{\mathrm{G}} \approx 1$.

5.A.2 Incoherent approximation

The second result needed for the comparison in Sec. 5.3.2 is the two-phonon structure factor for GaAs in the incoherent approximation. To calculate this, we use the simplified density of states in (5.17) corresponding to the long-wavelength limit. Performing the $n = 2$ integral in (5.10) gives

$$S_{n=2}(q,\omega) = \mathscr{S}_{\mathrm{LALA}} + \mathscr{S}_{\mathrm{LATA}} + \ldots \tag{5.46}$$

where each $\mathscr{S}$ is a contribution to the $n = 2$ structure factor from the part of the density of states associated with the subscripted modes, and the ellipsis indicates we sum over all combinations

of modes. The first term of the sum in (5.46) is

$$\begin{aligned}\mathscr{S}_{\mathrm{LALA}} =& \frac{2\pi}{\Omega_c}\frac{q^4}{96c_{\mathrm{LA}}^6 q_{\mathrm{BZ}}^6 m_p^2}\Bigg(\omega^3\Theta(c_{\mathrm{LA}}q_{\mathrm{BZ}}-\omega)\\ &-\left(4c_{\mathrm{LA}}^3q_{\mathrm{BZ}}^3-6c_{\mathrm{LA}}^2q_{\mathrm{BZ}}^2\omega+\omega^3\right)\\ &\times\Theta(\omega-c_{\mathrm{LA}}q_{\mathrm{BZ}})\Theta(2c_{\mathrm{LA}}q_{\mathrm{BZ}}-\omega)\Bigg),\end{aligned} \tag{5.47}$$

and $\mathscr{S}_{\mathrm{TATA}}$ is given by $\mathscr{S}_{\mathrm{LALA}}$ with the replacement LA $\rightarrow$ TA and an additional overal factor of 4. The same procedure gives the LATA term as

$$\begin{aligned}\mathscr{S}_{\mathrm{LATA}} =& \frac{2\pi}{\Omega_c}\frac{q^4}{24c_{\mathrm{LA}}^3q_{\mathrm{BZ}}^6m_p^2}\Bigg(\frac{\omega^3}{c_{\mathrm{TA}}^3}\Theta(c_{\mathrm{TA}}q_{\mathrm{BZ}}-\omega)\\ &+\frac{-2c_{\mathrm{TA}}q_{\mathrm{BZ}}^3+3\omega q_{\mathrm{BZ}}^2}{c_{\mathrm{TA}}}\Theta(\omega-c_{\mathrm{TA}}q_{\mathrm{BZ}})\Theta(c_{\mathrm{LA}}q_{\mathrm{BZ}}-\omega)\\ &+\frac{-2(c_{\mathrm{LA}}^3+c_{\mathrm{TA}}^3)q_{\mathrm{BZ}}^3+3(c_{\mathrm{LA}}^2+c_{\mathrm{TA}}^2)q_{\mathrm{BZ}}^2\omega-\omega^3}{c_{\mathrm{TA}}^3}\\ &\times\Theta(\omega-c_{\mathrm{LA}}q_{\mathrm{BZ}})\Theta((c_{\mathrm{LA}}+c_{\mathrm{TA}})q_{\mathrm{BZ}}-\omega)\Bigg).\end{aligned} \tag{5.48}$$

as well as the LOLA term,

$$\begin{aligned}\mathscr{S}_{\mathrm{LOLA}} =& \frac{2\pi}{\Omega_c}\frac{a^5\left(q_{\mathrm{BZ}}^2q^4\right)}{768\pi^5c_{\mathrm{LA}}^3m_p^2\omega_{\mathrm{LO}}}(\omega-\omega_{\mathrm{LO}})\\ &\times\Theta(\omega-\omega_{\mathrm{LO}})\Theta((c_{\mathrm{LA}}q_{\mathrm{BZ}}+\omega_{\mathrm{LO}})-\omega).\end{aligned} \tag{5.49}$$

Again we may find $\mathscr{S}_{\mathrm{LOTA}}$, $\mathscr{S}_{\mathrm{TOLA}}$, and $\mathscr{S}_{\mathrm{TOTA}}$ by relabelings and inserting relevant factors of two for polarizations. Note that, since the incoherent approximation does not recover the q^6 scaling resulting from interference, we have written the structure factor here using $q_{\mathrm{BZ}} = 2\pi/a$ to make the comparison more explicit. At lowest order in x and for $A_1 \approx A_2$, such a comparison of (5.44) and (5.49) shows a relative factor of $40/\pi^3 \approx 1$ for the LOLA channel. Lastly, for the

remaining optical-optical channels we find

$$\begin{aligned}
\mathscr{S}_{\mathrm{LOLO}} &= \frac{2\pi}{\Omega_c}\frac{q^4}{144m_p^2\omega_{\mathrm{LO}}^2}\delta(\omega-2\omega_{\mathrm{LO}}) \\
\mathscr{S}_{\mathrm{LOTO}} &= \frac{2\pi}{\Omega_c}\frac{q^4}{36m_p^2\omega_{\mathrm{LO}}\omega_{\mathrm{TO}}}\delta(\omega-(\omega_{\mathrm{LO}}+\omega_{\mathrm{TO}})) \\
\mathscr{S}_{\mathrm{TOTO}} &= \frac{2\pi}{\Omega_c}\frac{q^4}{36m_p^2\omega_{\mathrm{TO}}^2}\delta(\omega-2\omega_{\mathrm{TO}}).
\end{aligned} \tag{5.50}$$

A comparison now of (5.43) and (5.50) shows the incoherent approximation gives a smaller structure factor by factors of $2\pi/5$ – $6\pi/5 \approx 2-4$.

5.B Impulse approximation

In this section we discuss how to obtain the impulse approximation form of the structure factor, (5.21) in Sec. 5.3.4. To achieve this we must approximate the t integral in (5.19) for large q. The expression in (5.19) can be written as

$$\mathscr{C}_{\ell d} = \frac{1}{V}e^{-2W_d(\mathbf{q})}\int_{-\infty}^{\infty}dt\, e^{f(t)}. \tag{5.51}$$

with

$$\begin{aligned}
\mathrm{Re}[f(t)] &\equiv \frac{q^2}{2m_d}\int d\omega'\frac{D_d(\omega')}{\omega'}\cos\big(\omega' t\big) \\
\mathrm{Im}[f(t)] &\equiv \frac{q^2}{2m_d}\int d\omega'\frac{D_d(\omega')}{\omega'}\sin\big(\omega' t\big) - \omega t.
\end{aligned} \tag{5.52}$$

From this, we see there is a global maximum in the real part and a global minimum in the modulus of the imaginary part at $t=0$. This allows us to perform a steepest-descent expansion about $t=0$, giving

$$\mathscr{C}_{\ell d} \approx \frac{1}{V}\int_{-\infty}^{\infty}dt\, e^{it\left(\frac{q^2}{2m_d}-\omega\right)-\frac{t^2}{2}\frac{q^2\bar{\omega}_d}{2m_d}}, \tag{5.53}$$

where again $\bar{\omega}_d = \int d\omega' \omega' D_d(\omega')$. Note that the leading term in the expansion about $t = 0$ cancelled the Debye Waller factor, assuming the form given in (5.11). Evaluating the above gives

$$\mathscr{C}_{\ell d} \approx \frac{1}{V}\sqrt{\frac{2\pi}{\Delta_d^2}} e^{-\frac{\left(\omega - \frac{q^2}{2m_d}\right)^2}{2\Delta_d^2}}, \tag{5.54}$$

which is the impulse approximation result.

In obtaining this form, we have assumed that any other local maxima in t gives a subdominant contribution to the $t = 0$ maximum. In particular, aside from the $t = 0$ point, which is a global maximum in $\mathrm{Re}[f(t)]$, there are local maxima in the real part which will generally be near integer multiples of $2\pi/\bar{\omega}_d$. The leading order contribution from each additional maxima t_{max} is given by evaluating the real part in the exponential at the location of the maxima.

This must necessarily be smaller than the $t = 0$ contribution since the following inequality is always satisfied

$$\int d\omega' \frac{D_d(\omega')}{\omega'} \cos\left(\omega' t_{\mathrm{max}}\right) < \int d\omega' \frac{D_d(\omega')}{\omega'}. \tag{5.55}$$

Since $t_{\mathrm{max}} \sim 2\pi/\bar{\omega}_d$, the left hand side will be suppressed by an $O(1)$ amount due to presence of the $\cos(\omega' t_{\mathrm{max}})$. Then, the contribution from the local maxima will be exponentially suppressed:

$$e^{\frac{q^2}{2m_d}\int d\omega' \frac{D_d(\omega')}{\omega'} \cos(\omega' t_{\mathrm{max}})} \ll e^{\frac{q^2}{2m_d}\int d\omega' \frac{D_d(\omega')}{\omega'}} \tag{5.56}$$

as long as the following condition is satisfied

$$\frac{q^2}{2m_d} \gg \frac{1}{\int d\omega' \frac{D_d(\omega')}{\omega'}} \sim \bar{\omega}_d. \tag{5.57}$$

Here we have taken $\int d\omega' \frac{D_d(\omega')}{\omega'} \sim 1/\bar{\omega}_d$ as a typical scale for this integral, although it will differ by an $O(1)$ factor. Therefore, as long as the free nuclear recoil energy $\omega = q^2/(2m_d)$ is well above the typical phonon energy $\bar{\omega}_d$ for a scattering off of atom d, the $t = 0$ maximum is dominant and the impulse approximation should be accurate.

In the regime where $q^2/2m_d$ is comparable to $\bar{\omega}_d$, the contributions from the additional maxima in t can become important.

Nevertheless, the impulse approximation is still accurate at large ω even in this case because of cancellations from the rapidly changing phase in $\mathrm{Im}[f(t)]$. When $\omega \gg \bar{\omega}_d$, then $\mathrm{Im}[f(t)] \approx -\omega t$ for t around $t_{\max} \sim 2\pi/\bar{\omega}_d$. This implies large oscillations of $f(t)$ around $t_{\max}$, which suppresses the contribution from these local maxima. On the other hand, if $\omega \lesssim \bar{\omega}_d$, there may be large corrections to the impulse approximation due to these additional maxima.

These effects were shown in Fig. 5.3.3a when comparing the multiphonon expansion result to the impulse approximation. The middle panel showed the result if $q = \sqrt{2m_d\bar{\omega}_d}$, in the $m_{\mathrm{Ga}} \approx m_{\mathrm{As}}$ approximation. For $\omega \gtrsim \bar{\omega}_d$ the structure factor falls smoothly and can be reasonably captured by the impulse approximation, while for $\omega \lesssim \bar{\omega}_d \approx 22$ meV or at the optical phonon energies 31 and 33 meV there are sharp peaks in the multiphonon response that are not captured by the impulse approximation. For $q = 2\sqrt{2m_d\bar{\omega}_d}$ the many multiphonon peaks merge and add up to a shape similar to the impulse approximation over the whole ω range. Practically, for our calculations, we use the impulse approximation for the structure factor at $q > 2\sqrt{2m_d\bar{\omega}_d}$. Though the approximation has small differences with the exact result when $q \sim 2\sqrt{2m_d\bar{\omega}_d}$, integrating over the allowed phase space for the rate largely washes out these differences.

5.C Implementation in `DarkELF`

In the main text, we presented the formulas in the manner which is most clear from the point of view of the various approximations and their regimes of validity. These formulas were not always suitable however for an efficient numerical implementation, which we address in this section. We also provide details on their implementation in the `DarkELF` package [76].

In the main text we gave the rate in the isotropic limit, (5.27). In order to calculate the rate for any mediator and to obtain the differential rate $dR/d\omega$, it is convenient to perform the

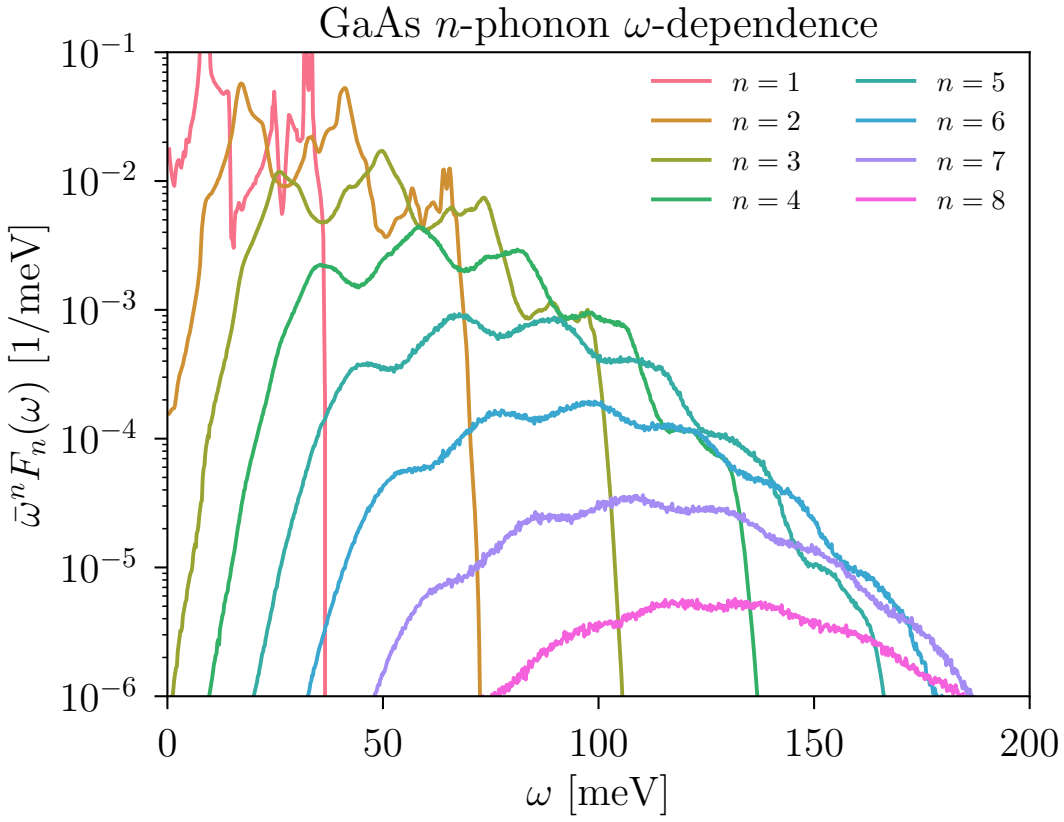

Figure 5.C.1. Here we have plotted $\bar{\omega}^n F_n(\omega)$, where $F_n(\omega)$ is the ω-dependent part of the structure factor in the incoherent approximation and given explicitly in (5.62). At fixed q, the structure factor decreases quickly with increasing ω.

v-integral first and rewrite the rate as:

$$R = \frac{1}{4\pi\rho_T}\frac{\rho_\chi}{m_\chi}\frac{\sigma_p}{\mu_\chi^2}\int_{\omega_{\rm th}}^{\omega_+} d\omega \int_{q_-}^{q_+} dq\, q\, |\tilde{F}(q)|^2 S(q,\omega)\, \eta(v_{\rm min}(q,\omega)) \tag{5.58}$$

where now the integration limits are given by

$$q_\pm = m_\chi \left(v_{\rm max} \pm \sqrt{v_{\rm max}^2 - \frac{2\omega}{m_\chi}}\right) \tag{5.59}$$

$$\omega_+ = \frac{1}{2} m_\chi v_{\rm max}^2 \tag{5.60}$$

with $v_{\rm max} = v_{\rm esc} + v_e$ the maximum DM speed in the lab frame. The η function is given by

$$\eta(v_{\rm min}) = \int d^3\mathbf{v} \frac{f(\mathbf{v})}{v} \Theta(v - v_{\rm min}) \tag{5.61}$$

with $v_{\rm min}(q,\omega) = \frac{q}{2m_\chi} + \frac{\omega}{q}$.

To evaluate the rate using incoherent approximation, we provide look-up tables for the structure factor. At each n for the sum in (5.18), the q and ω parts of the integral are separable, so we can capture the ω-dependent part with the family of functions

$$F_{n,d}(\omega) \equiv \frac{1}{n!}\left(\prod_{i=1}^{n} \int d\omega_i \frac{D_d(\omega_i)}{\omega_i}\right) \delta\left(\sum_i \omega_i - \omega\right), \tag{5.62}$$

and calculate the rate in terms of functions $F_{n,d}$. These functions are simple to calculate numerically up to $n \leq 10$, which we have tabulated and provided in `DarkELF` as look-up tables to speed up the calculation. The combination $\bar{\omega}^n F_n(\omega)$ is shown in Fig. 5.C.1 for GaAs in the $m_{\rm Ga} \approx m_{\rm As}$ approximation. For increasingly high n, the $F_{n,d}$ become increasingly smooth.

We have added several additional functions to `DarkELF` for the differential and integrated rate calculations from the single phonon to the nuclear recoil regime. Tab. 5.C.1 describes some of the new relevant functions. These functions currently work for materials with up to two atoms

per unit cell. We have included the necessary data files for the multiphonon calculation for GaN, Al, ZnS, GaAs, Si, and Ge from a combination of DFT and experimental sources. We also allow the user to input their own calculations or extractions of the (partial) density of states, as well as momentum-dependent dark matter-nucleon couplings. Before calculating multiphonon scattering rates in `DarkELF`, it is necessary to tabulate the auxiliary function (5.62) for each atom. This is done using the `DarkELF` function *create_Fn_omega*. This step is the most time consuming part of the calculation, so we provide these pre-tabulated for the aforementioned materials. For calculations with a user-supplied (partial) density of states, these tables must first be updated by running *create_Fn_omega*. `DarkELF` will save these new look-up tables for future computations, such that this step only need to be performed once. Next we describe the functions that return important results. All of the following straightforwardly apply equations (5.58-5.61).

R_single_phonon: This function takes the energy threshold and DM-nucleon cross sections and outputs the rate in the long-wavelength single phonon regime using the analytic functions (3.19-3.20).

R_multiphonons_no_single: This function takes the energy threshold and DM-nucleon cross section as inputs and calculates the total integrated rate, excluding the single phonon processes at long wavelengths $q < q_{\rm BZ}$. In other words, this calculation includes only the purple (multiphonon expansion) and red (impulse approximation) phase space regions in Fig. 5.3.4.

sigma_multiphonons: This takes the energy threshold as input and returns the necessary DM-nucleon cross section to produce three events per kg-year for any number of phonons. In order to return this cross section, this function first calculates the total rate by summing the outputs of *R_single_phonon* and *R_multiphonons_no_single*, so it includes the entire calculation scheme depicted in Fig. 5.3.4.

_dR_domega_multiphonons_no_single: This function takes the energy transfer ω and DM-nucleon cross section and returns the differential rate $\frac{dR}{d\omega}$ at that energy excluding single phonons in the long wavelength regime. This comes from equation (5.58) without evaluating the ω integral. We exclude the single coherent phonon here since the long-wavelength approximation

has delta functions in energy in the differential rate.

5.D Additional results

Here, we provide additional results for Ge, Si, and diamond. Concretely, Fig. 5.D.1 shows the density of states for these three materials, as extracted from [6]. Fig. 5.D.2 shows the differential scattering rate via a massive scalar mediator for two example DM masses in GaAs, Ge and Si targets. Finally, Figs. 5.D.3, 5.D.4, and 5.D.5 are the cross section plots corresponding to an integrated rate of 3 events/kg-year for Ge, Si, and diamond, respectively.

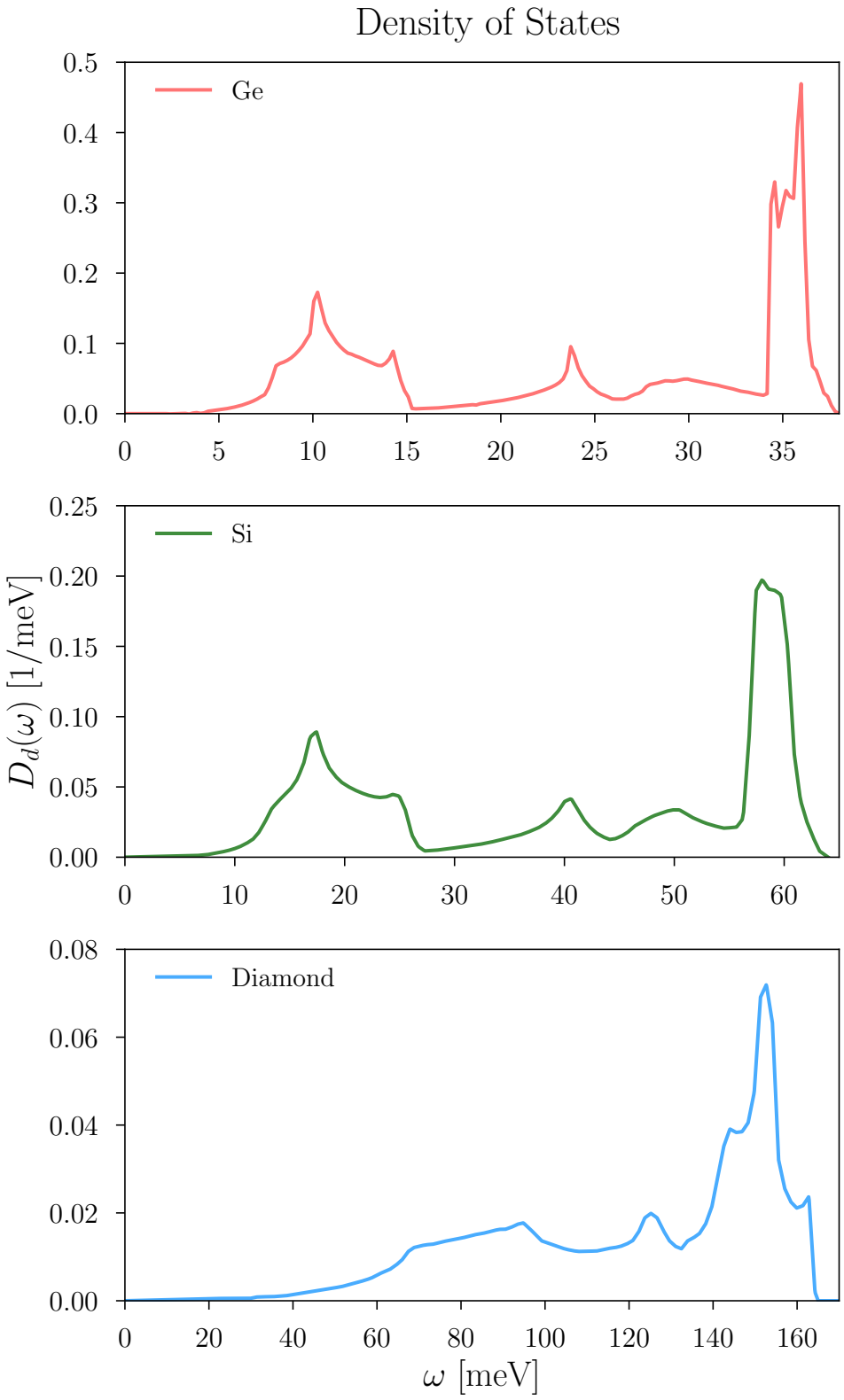

Figure 5.D.1. Densities of states for germanium, silicon, and diamond [6].

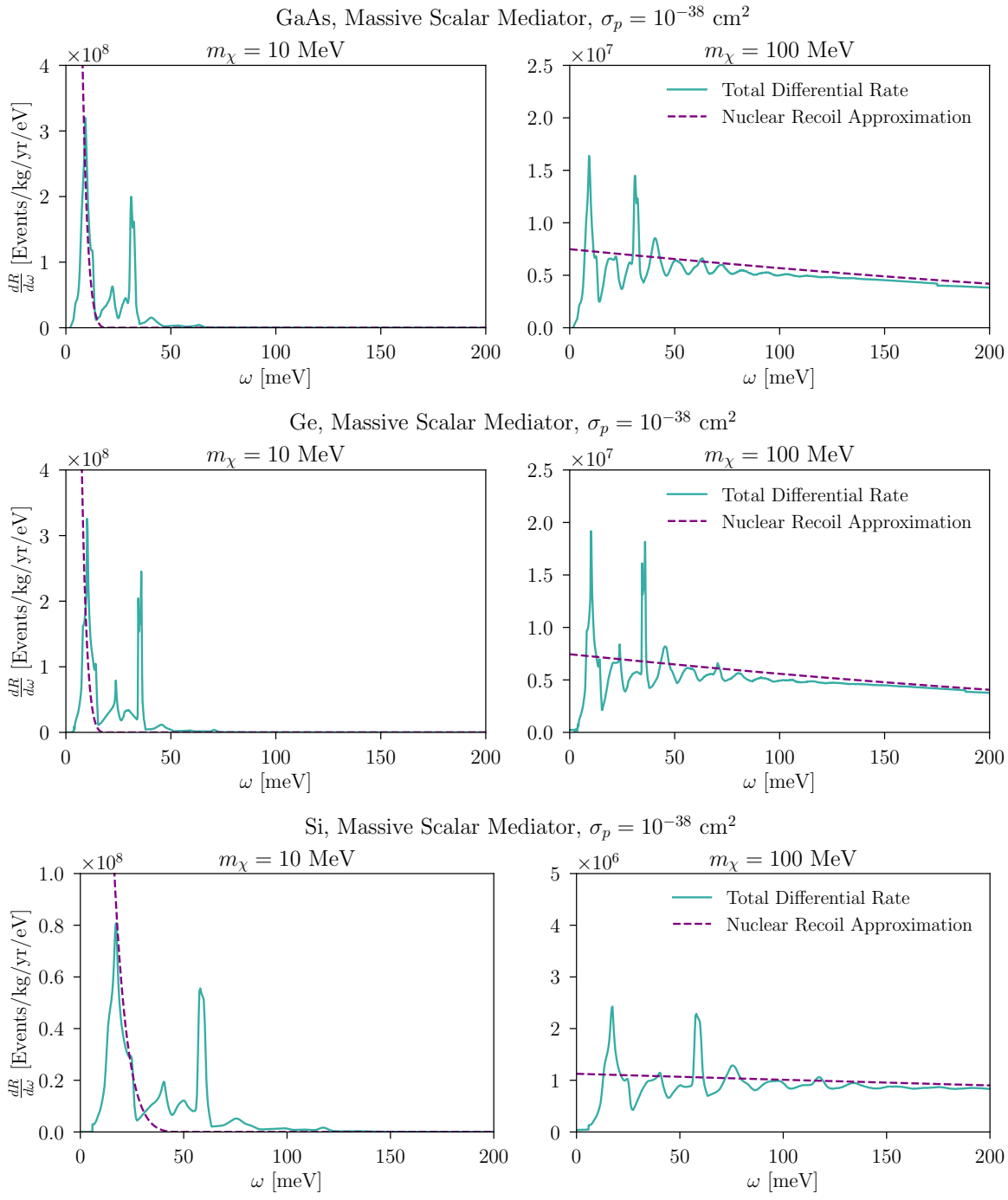

Figure 5.D.2. Differential rate for various materials and a massive scalar mediator, compared with the nuclear recoil approximation. The single phonon contribution from the long wavelength regime is not shown, since it gives a delta function contribution.

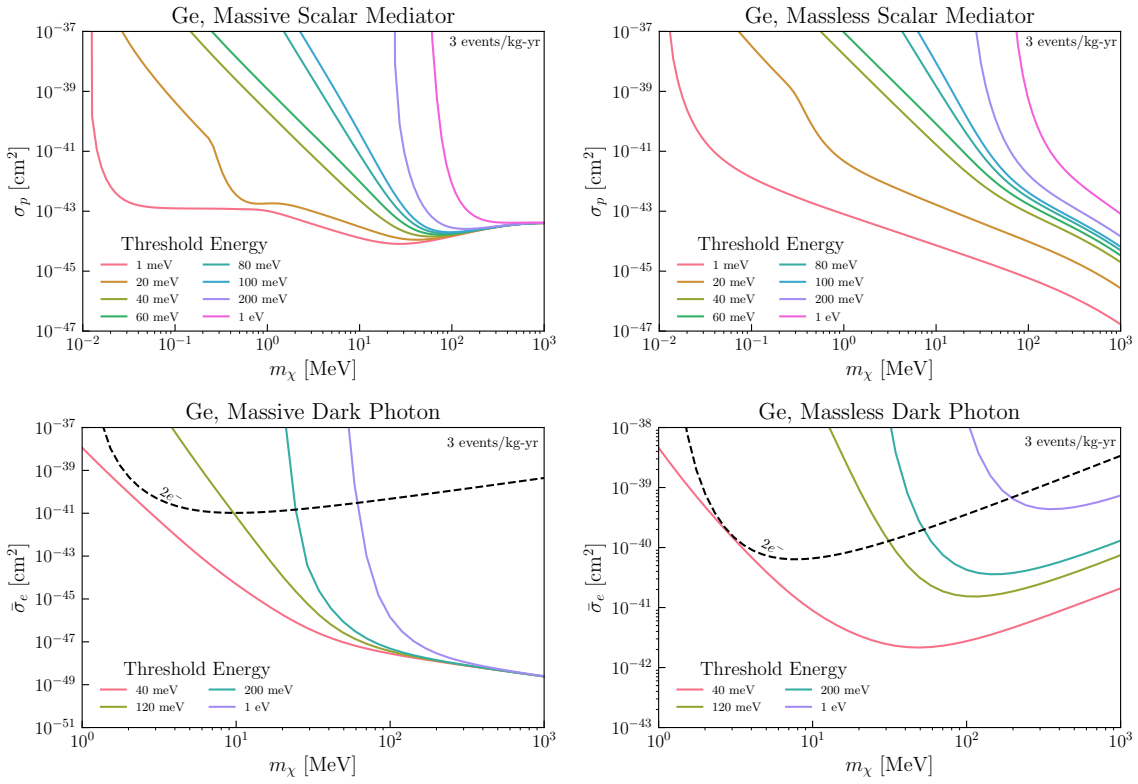

Figure 5.D.3. Cross section plots for a rate of 3 events/kg-year exposure for different thresholds in Ge.

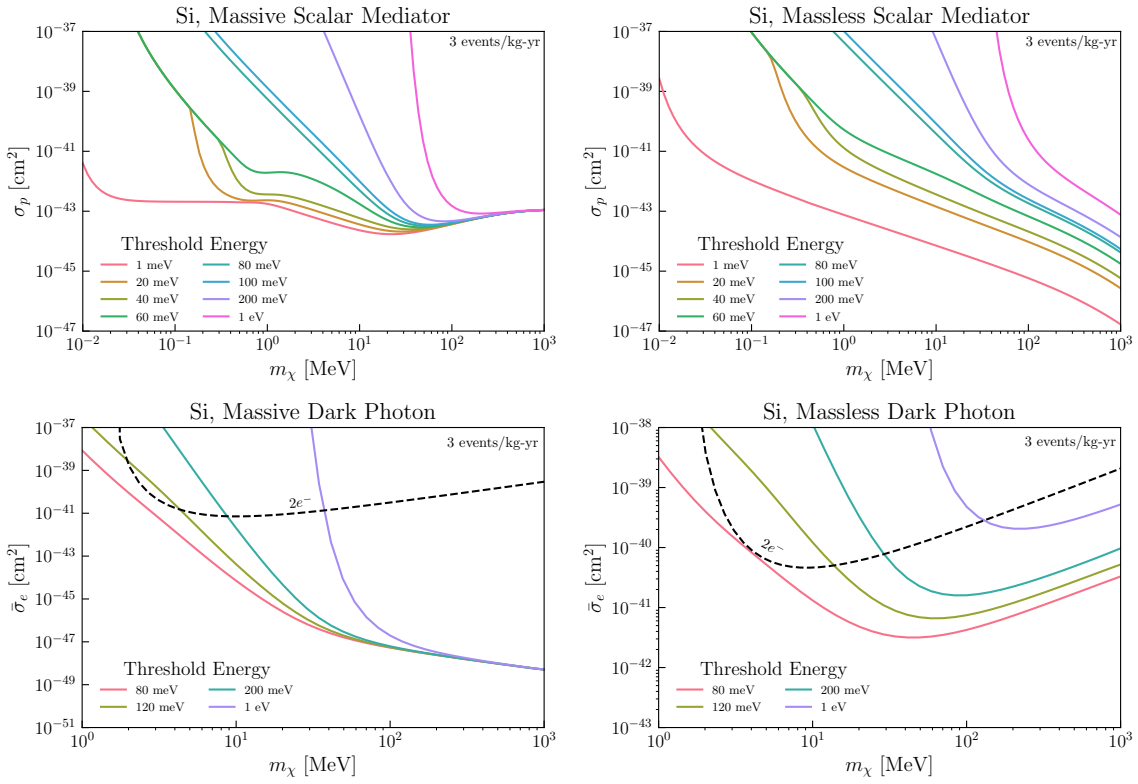

Figure 5.D.4. Cross section plots for a rate of 3 events/kg-year exposure for different thresholds in Si.

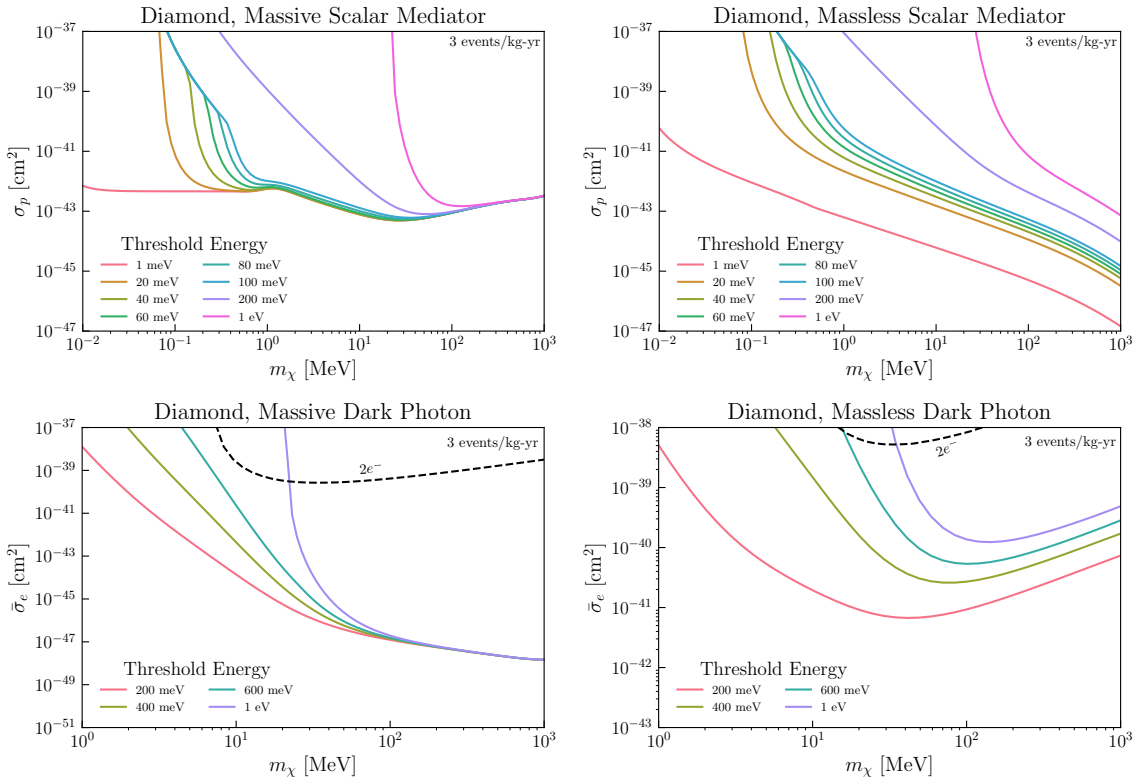

Figure 5.D.5. Cross section plots for a rate of 3 events/kg-year exposure for different thresholds in diamond.

Table 5.C.1. List of public functions in `DarkELF` related to multiphonon excitations from DM scattering. Only mandatory arguments are shown; for optional arguments and flags, see text and the documentation in repository. Some functions are only available for select materials, as indicated in the righthand column.

DM-multiphonon scattering

function	description	available for
`dRdomega_multiphonons_no_single(omega)`	Differential rate $dR/d\omega$ in 1/kg/yr/eV excluding long-wavelength single phonons	all except SiO_2, Al_2O_3
`R_multiphonons_no_single(omega)`	Total phonon rate in 1/kg-yr excluding long-wavelength single phonons	all except SiO_2, Al_2O_3
`sigma_multiphonons(omega)`	Nucleon cross section to produce 3 events/kg-yr	all except SiO_2, Al_2O_3

Chapter 6

Wrap-up and Outlook

DM candidates in the keV $\lesssim m_\chi \lesssim$ GeV mass regime have historically been underexplored, however experiments are in development to begin probing this parameter space through e.g. the phonon excitation described in this Thesis. With the diphonon results of Chapter 4 and the generic n phonon results of Chapter 5, we have a full, analytic description of the multiphonon response in cubic crystal targets. Given the prior known results for single phonon excitations at low energies, and nuclear recoil at high energies, these altogether provide a description across the entire phase space depicted in Fig. 2.4. The theoretical work for sub-GeV thermal candidates is not yet complete, however. For example, the isotropic approximation and crystal structures assumed do not apply for anisotropic crystal targets, like sapphire. Additionally, further numerical investigation of the validity of the incoherent and harmonic approximations is required. Our results nevertheless provide the first estimate of scattering rates up to $\mathcal{O}(1)$ theoretical uncertainties in the intermediate mass regime, informing experimental development. With the community turning toward other motivated candidates and searches amidst the WIMP parameter squeeze, our results provide an understanding of LDM signals which may be probed experimentally within the next decade. Continued experimental improvement to decrease energy thresholds may yet even foray into the single phonon regime, covering the entire mass range of sub-GeV thermal DM candidates.

Bibliography

[1] J. Aalbers, D. S. Akerib, C. W. Akerlof, A. K. Al Musalhi, F. Alder, A. Alqahtani, S. K. Alsum, C. S. Amarasinghe, A. Ames, T. J. Anderson, N. Angelides, H. M. Araújo, J. E. Armstrong, M. Arthurs, S. Azadi, A. J. Bailey, A. Baker, J. Balajthy, S. Balashov, J. Bang, J. W. Bargemann, M. J. Barry, J. Barthel, D. Bauer, A. Baxter, K. Beattie, J. Belle, P. Beltrame, J. Bensinger, T. Benson, E. P. Bernard, A. Bhatti, A. Biekert, T. P. Biesiadzinski, H. J. Birch, B. Birrittella, G. M. Blockinger, K. E. Boast, B. Boxer, R. Bramante, C. A. J. Brew, P. Brás, J. H. Buckley, V. V. Bugaev, S. Burdin, J. K. Busenitz, M. Buuck, R. Cabrita, C. Carels, D. L. Carlsmith, B. Carlson, M. C. Carmona-Benitez, M. Cascella, C. Chan, A. Chawla, H. Chen, J. J. Cherwinka, N. I. Chott, A. Cole, J. Coleman, M. V. Converse, A. Cottle, G. Cox, W. W. Craddock, O. Creaner, D. Curran, A. Currie, J. E. Cutter, C. E. Dahl, A. David, J. Davis, T. J. R. Davison, J. Delgaudio, S. Dey, L. de Viveiros, A. Dobi, J. E. Y. Dobson, E. Druszkiewicz, A. Dushkin, T. K. Edberg, W. R. Edwards, M. M. Elnimr, W. T. Emmet, S. R. Eriksen, C. H. Faham, A. Fan, S. Fayer, N. M. Fearon, S. Fiorucci, H. Flaecher, P. Ford, V. B. Francis, E. D. Fraser, T. Fruth, R. J. Gaitskell, N. J. Gantos, D. Garcia, A. Geffre, V. M. Gehman, J. Genovesi, C. Ghag, R. Gibbons, E. Gibson, M. G. D. Gilchriese, S. Gokhale, B. Gomber, J. Green, A. Greenall, S. Greenwood, M. G. D. van der Grinten, C. B. Gwilliam, C. R. Hall, S. Hans, K. Hanzel, A. Harrison, E. Hartigan-O'Connor, S. J. Haselschwardt, S. A. Hertel, G. Heuermann, C. Hjemfelt, M. D. Hoff, E. Holtom, J. Y-K. Hor, M. Horn, D. Q. Huang, D. Hunt, C. M. Ignarra, R. G. Jacobsen, O. Jahangir, R. S. James, S. N. Jeffery, W. Ji, J. Johnson, A. C. Kaboth, A. C. Kamaha, K. Kamdin, V. Kasey, K. Kazkaz, J. Keefner, D. Khaitan, M. Khaleeq, A. Khazov, I. Khurana, Y. D. Kim, C. D. Kocher, D. Kodroff, L. Korley, E. V. Korolkova, J. Kras, H. Kraus, S. Kravitz, H. J. Krebs, L. Kreczko, B. Krikler, V. A. Kudryavtsev, S. Kyre, B. Landerud, E. A. Leason, C. Lee, J. Lee, D. S. Leonard, R. Leonard, K. T. Lesko, C. Levy, J. Li, F. T. Liao, J. Liao, J. Lin, A. Lindote, R. Linehan, W. H. Lippincott, R. Liu, X. Liu, Y. Liu, C. Loniewski, M. I. Lopes, E. Lopez Asamar, B. López Paredes, W. Lorenzon, D. Lucero, S. Luitz, J. M. Lyle, P. A. Majewski, J. Makkinje, D. C. Malling, A. Manalaysay, L. Manenti, R. L. Mannino, N. Marangou, M. F. Marzioni, C. Maupin, M. E. McCarthy, C. T. McConnell, D. N. McKinsey, J. McLaughlin, Y. Meng, J. Migneault, E. H. Miller, E. Mizrachi, J. A. Mock, A. Monte, M. E. Monzani, J. A. Morad, J. D. Morales Mendoza, E. Morrison, B. J. Mount, M. Murdy, A. St. J. Murphy, D. Naim, A. Naylor, C. Nedlik, C. Nehrkorn, H. N. Nelson, F. Neves, A. Nguyen, J. A. Nikoleyczik, A. Nilima, J. O'Dell, F. G. O'Neill, K. O'Sullivan, I. Olcina, M. A. Olevitch, K. C. Oliver-Mallory, J. Orpwood, D. Pagenkopf, S. Pal, K. J. Palladino, J. Palmer, M. Pangilinan, N. Parveen, S. J. Patton, E. K. Pease, B. Penning,

C. Pereira, G. Pereira, E. Perry, T. Pershing, I. B. Peterson, A. Piepke, J. Podczerwinski, D. Porzio, S. Powell, R. M. Preece, K. Pushkin, Y. Qie, B. N. Ratcliff, J. Reichenbacher, L. Reichhart, C. A. Rhyne, A. Richards, Q. Riffard, G. R. C. Rischbieter, J. P. Rodrigues, A. Rodriguez, H. J. Rose, R. Rosero, P. Rossiter, T. Rushton, G. Rutherford, D. Rynders, J. S. Saba, D. Santone, A. B. M. R. Sazzad, R. W. Schnee, P. R. Scovell, D. Seymour, S. Shaw, T. Shutt, J. J. Silk, C. Silva, G. Sinev, K. Skarpaas, W. Skulski, R. Smith, M. Solmaz, V. N. Solovov, P. Sorensen, J. Soria, I. Stancu, M. R. Stark, A. Stevens, T. M. Stiegler, K. Stifter, R. Studley, B. Suerfu, T. J. Sumner, P. Sutcliffe, N. Swanson, M. Szydagis, M. Tan, D. J. Taylor, R. Taylor, W. C. Taylor, D. J. Temples, B. P. Tennyson, P. A. Terman, K. J. Thomas, D. R. Tiedt, M. Timalsina, W. H. To, A. Tomás, Z. Tong, D. R. Tovey, J. Tranter, M. Trask, M. Tripathi, D. R. Tronstad, C. E. Tull, W. Turner, L. Tvrznikova, U. Utku, J. Va'vra, A. Vacheret, A. C. Vaitkus, J. R. Verbus, E. Voirin, W. L. Waldron, A. Wang, B. Wang, J. J. Wang, W. Wang, Y. Wang, J. R. Watson, R. C. Webb, A. White, D. T. White, J. T. White, R. G. White, T. J. Whitis, M. Williams, W. J. Wisniewski, M. S. Witherell, F. L. H. Wolfs, J. D. Wolfs, S. Woodford, D. Woodward, S. D. Worm, C. J. Wright, Q. Xia, X. Xiang, Q. Xiao, J. Xu, M. Yeh, J. Yin, I. Young, P. Zarzhitsky, A. Zuckerman, and E. A. Zweig. First dark matter search results from the lux-zeplin (lz) experiment, 2022.

[2] Sinead Griffin, Simon Knapen, Tongyan Lin, and Kathryn M. Zurek. Directional detection of light dark matter with polar materials. *Phys. Rev. D*, 98:115034, Dec 2018.

[3] Yonatan Kahn and Tongyan Lin. Searches for light dark matter using condensed matter systems. *Reports on Progress in Physics*, 85(6):066901, May 2022.

[4] Snowmass2021-letter of interest the tesseract dark matter project. 2020.

[5] Simon Knapen, Tongyan Lin, Matt Pyle, and Kathryn M. Zurek. Detection of light dark matter with optical phonons in polar materials. *Physics Letters B*, 785:386–390, 2018.

[6] Anubhav Jain and et. al. The Materials Project: A materials genome approach to accelerating materials innovation. *APL Materials*, 1(1):011002, 2013.

[7] P. J. Brown, A. G. Fox, E. N. Maslen, M. A. O'Keefe, and B. T. M. Willis. *Intensity of diffracted intensities*, chapter 6.1, pages 554–595. American Cancer Society, 2006.

[8] F. Zwicky. Die Rotverschiebung von extragalaktischen Nebeln. *Helvetica Physica Acta*, 6:110–127, January 1933.

[9] Vera C. Rubin and Jr. Ford, W. Kent. Rotation of the Andromeda Nebula from a Spectroscopic Survey of Emission Regions. , 159:379, February 1970.

[10] V. C. Rubin, Jr. Ford, W. K., and N. Thonnard. Rotational properties of 21 SC galaxies with a large range of luminosities and radii, from NGC 4605 (R=4kpc) to UGC 2885 (R=122kpc). , 238:471–487, June 1980.

[11] M. Milgrom. A modification of the Newtonian dynamics as a possible alternative to the hidden mass hypothesis. , 270:365–370, July 1983.

[12] Jacob D. Bekenstein. Relativistic gravitation theory for the modified newtonian dynamics paradigm. *Phys. Rev. D*, 70:083509, Oct 2004.

[13] Planck Collaboration, Aghanim, N., Akrami, Y., Arroja, F., Ashdown, M., Aumont, J., Baccigalupi, C., Ballardini, M., Banday, A. J., Barreiro, R. B., Bartolo, N., Basak, S., Battye, R., Benabed, K., Bernard, J.-P., Bersanelli, M., Bielewicz, P., Bock, J. J., Bond, J. R., Borrill, J., Bouchet, F. R., Boulanger, F., Bucher, M., Burigana, C., Butler, R. C., Calabrese, E., Cardoso, J.-F., Carron, J., Casaponsa, B., Challinor, A., Chiang, H. C., Colombo, L. P. L., Combet, C., Contreras, D., Crill, B. P., Cuttaia, F., de Bernardis, P., de Zotti, G., Delabrouille, J., Delouis, J.-M., Désert, F.-X., Di Valentino, E., Dickinson, C., Diego, J. M., Donzelli, S., Doré, O., Douspis, M., Ducout, A., Dupac, X., Efstathiou, G., Elsner, F., Enßlin, T. A., Eriksen, H. K., Falgarone, E., Fantaye, Y., Fergusson, J., Fernandez-Cobos, R., Finelli, F., Forastieri, F., Frailis, M., Franceschi, E., Frolov, A., Galeotta, S., Galli, S., Ganga, K., Génova-Santos, R. T., Gerbino, M., Ghosh, T., González-Nuevo, J., Górski, K. M., Gratton, S., Gruppuso, A., Gudmundsson, J. E., Hamann, J., Handley, W., Hansen, F. K., Helou, G., Herranz, D., Hildebrandt, S. R., Hivon, E., Huang, Z., Jaffe, A. H., Jones, W. C., Karakci, A., Keihänen, E., Keskitalo, R., Kiiveri, K., Kim, J., Kisner, T. S., Knox, L., Krachmalnicoff, N., Kunz, M., Kurki-Suonio, H., Lagache, G., Lamarre, J.-M., Langer, M., Lasenby, A., Lattanzi, M., Lawrence, C. R., Le Jeune, M., Leahy, J. P., Lesgourgues, J., Levrier, F., Lewis, A., Liguori, M., Lilje, P. B., Lilley, M., Lindholm, V., López-Caniego, M., Lubin, P. M., Ma, Y.-Z., Macías-Pérez, J. F., Maggio, G., Maino, D., Mandolesi, N., Mangilli, A., Marcos-Caballero, A., Maris, M., Martin, P. G., Martinelli, M., Martínez-González, E., Matarrese, S., Mauri, N., McEwen, J. D., Meerburg, P. D., Meinhold, P. R., Melchiorri, A., Mennella, A., Migliaccio, M., Millea, M., Mitra, S., Miville-Deschênes, M.-A., Molinari, D., Moneti, A., Montier, L., Morgante, G., Moss, A., Mottet, S., Münchmeyer, M., Natoli, P., Nørgaard-Nielsen, H. U., Oxborrow, C. A., Pagano, L., Paoletti, D., Partridge, B., Patanchon, G., Pearson, T. J., Peel, M., Peiris, H. V., Perrotta, F., Pettorino, V., Piacentini, F., Polastri, L., Polenta, G., Puget, J.-L., Rachen, J. P., Reinecke, M., Remazeilles, M., Renault, C., Renzi, A., Rocha, G., Rosset, C., Roudier, G., Rubiño-Martín, J. A., Ruiz-Granados, B., Salvati, L., Sandri, M., Savelainen, M., Scott, D., Shellard, E. P. S., Shiraishi, M., Sirignano, C., Sirri, G., Spencer, L. D., Sunyaev, R., Suur-Uski, A.-S., Tauber, J. A., Tavagnacco, D., Tenti, M., Terenzi, L., Toffolatti, L., Tomasi, M., Trombetti, T., Valiviita, J., Van Tent, B., Vibert, L., Vielva, P., Villa, F., Vittorio, N., Wandelt, B. D., Wehus, I. K., White, M., White, S. D. M., Zacchei, A., and Zonca, A. Planck 2018 results - i. overview and the cosmological legacy of planck. *A&A*, 641:A1, 2020.

[14] E. Komatsu, K. M. Smith, J. Dunkley, C. L. Bennett, B. Gold, G. Hinshaw, N. Jarosik, D. Larson, M. R. Nolta, L. Page, D. N. Spergel, M. Halpern, R. S. Hill, A. Kogut, M. Limon, S. S. Meyer, N. Odegard, G. S. Tucker, J. L. Weiland, E. Wollack, and E. L. Wright. SEVEN-YEAR iWILKINSON MICROWAVE ANISOTROPY PROBE/i (iWMAP/i) OBSERVATIONS: COSMOLOGICAL INTERPRETATION. *The Astrophysical Journal Supplement Series*, 192(2):18, jan 2011.

[15] Richard Massey, Thomas Kitching, and Johan Richard. The dark matter of gravitational lensing. *Reports on Progress in Physics*, 73(8):086901, jul 2010.

[16] S. W. Allen, R. W. Schmidt, A. C. Fabian, and H. Ebeling. Cosmological constraints from the local X-ray luminosity function of the most X-ray-luminous galaxy clusters. *Monthly Notices of the Royal Astronomical Society*, 342(1):287–298, 06 2003.

[17] Raul E. Angulo and Oliver Hahn. Large-scale dark matter simulations. *Living Reviews in Computational Astrophysics*, 8(1):1, Feb 2022.

[18] Wayne Hu, Rennan Barkana, and Andrei Gruzinov. Fuzzy cold dark matter: The wave properties of ultralight particles. *Phys. Rev. Lett.*, 85:1158–1161, Aug 2000.

[19] Lam Hui. Wave dark matter. *Annual Review of Astronomy and Astrophysics*, 59(1):247–289, 2021.

[20] Kohei Hayashi, Elisa G. M. Ferreira, and Hei Yin Jowett Chan. Narrowing the mass range of fuzzy dark matter with ultrafaint dwarfs. *The Astrophysical Journal Letters*, 912(1):L3, apr 2021.

[21] Edward A. Baltz. Dark matter candidates, 2004.

[22] Jihn E. Kim and Gianpaolo Carosi. Axions and the strong cp problem. *Rev. Mod. Phys.*, 82:557–601, Mar 2010.

[23] Peter Svrcek and Edward Witten. Axions in string theory. *Journal of High Energy Physics*, 2006(06):051–051, jun 2006.

[24] Jonathan L. Feng. Dark matter candidates from particle physics and methods of detection. *Annual Review of Astronomy and Astrophysics*, 48(1):495–545, 2010.

[25] Tongyan Lin. TASI lectures on dark matter models and direct detection. 2019.

[26] Marco Cirelli, Nicolao Fornengo, and Alessandro Strumia. Minimal dark matter. *Nuclear Physics B*, 753(1):178–194, 2006.

[27] M. Beneke, A. Bharucha, A. Hryczuk, S. Recksiegel, and P. Ruiz-Femenía. The last refuge of mixed wino-higgsino dark matter. *Journal of High Energy Physics*, 2017(1):2, Jan 2017.

[28] Rebecca Krall and Matthew Reece. Last electroweak WIMP standing: pseudo-dirac higgsino status and compact stars as future probes. *Chinese Physics C*, 42(4):043105, apr 2018.

[29] E. Aprile, J. Aalbers, F. Agostini, M. Alfonsi, L. Althueser, F. D. Amaro, M. Anthony, F. Arneodo, L. Baudis, B. Bauermeister, M. L. Benabderrahmane, T. Berger, P. A. Breur, A. Brown, A. Brown, E. Brown, S. Bruenner, G. Bruno, R. Budnik, C. Capelli, J. M. R. Cardoso, D. Cichon, D. Coderre, A. P. Colijn, J. Conrad, J. P. Cussonneau, M. P. Decowski, P. de Perio, P. Di Gangi, A. Di Giovanni, S. Diglio, A. Elykov, G. Eurin, J. Fei, A. D.

Ferella, A. Fieguth, W. Fulgione, A. Gallo Rosso, M. Galloway, F. Gao, M. Garbini, C. Geis, L. Grandi, Z. Greene, H. Qiu, C. Hasterok, E. Hogenbirk, J. Howlett, R. Itay, F. Joerg, B. Kaminsky, S. Kazama, A. Kish, G. Koltman, H. Landsman, R. F. Lang, L. Levinson, Q. Lin, S. Lindemann, M. Lindner, F. Lombardi, J. A. M. Lopes, J. Mahlstedt, A. Manfredini, T. Marrodán Undagoitia, J. Masbou, D. Masson, M. Messina, K. Micheneau, K. Miller, A. Molinario, K. Morå, M. Murra, J. Naganoma, K. Ni, U. Oberlack, B. Pelssers, F. Piastra, J. Pienaar, V. Pizzella, G. Plante, R. Podviianiuk, N. Priel, D. Ramírez García, L. Rauch, S. Reichard, C. Reuter, B. Riedel, A. Rizzo, A. Rocchetti, N. Rupp, J. M. F. dos Santos, G. Sartorelli, M. Scheibelhut, S. Schindler, J. Schreiner, D. Schulte, M. Schumann, L. Scotto Lavina, M. Selvi, P. Shagin, E. Shockley, M. Silva, H. Simgen, D. Thers, F. Toschi, G. Trinchero, C. Tunnell, N. Upole, M. Vargas, O. Wack, H. Wang, Z. Wang, Y. Wei, C. Weinheimer, C. Wittweg, J. Wulf, J. Ye, Y. Zhang, and T. Zhu. Dark matter search results from a one ton-year exposure of xenon1t. *Phys. Rev. Lett.*, 121:111302, Sep 2018.

[30] Kim Griest and Marc Kamionkowski. Unitarity limits on the mass and radius of dark-matter particles. *Phys. Rev. Lett.*, 64:615–618, Feb 1990.

[31] Benjamin W. Lee and Steven Weinberg. Cosmological lower bound on heavy-neutrino masses. *Phys. Rev. Lett.*, 39:165–168, Jul 1977.

[32] Maxim Pospelov, Adam Ritz, and Mikhail Voloshin. Secluded wimp dark matter. *Physics Letters B*, 662(1):53–61, 2008.

[33] Jim Alexander, Marco Battaglieri, Bertrand Echenard, Rouven Essig, Matthew Graham, Eder Izaguirre, John Jaros, Gordan Krnjaic, Jeremy Mardon, David Morrissey, Tim Nelson, Maxim Perelstein, Matt Pyle, Adam Ritz, Philip Schuster, Brian Shuve, Natalia Toro, Richard G Van De Water, Daniel Akerib, Haipeng An, Konrad Aniol, Isaac J. Arnquist, David M. Asner, Henning O. Back, Keith Baker, Nathan Baltzell, Dipanwita Banerjee, Brian Batell, Daniel Bauer, James Beacham, Jay Benesch, James Bjorken, Nikita Blinov, Celine Boehm, Mariangela Bondí, Walter Bonivento, Fabio Bossi, Stanley J. Brodsky, Ran Budnik, Stephen Bueltmann, Masroor H. Bukhari, Raymond Bunker, Massimo Carpinelli, Concetta Cartaro, David Cassel, Gianluca Cavoto, Andrea Celentano, Animesh Chaterjee, Saptarshi Chaudhuri, Gabriele Chiodini, Hsiao-Mei Sherry Cho, Eric D. Church, D. A. Cooke, Jodi Cooley, Robert Cooper, Ross Corliss, Paolo Crivelli, Francesca Curciarello, Annalisa D'Angelo, Hooman Davoudiasl, Marzio De Napoli, Raffaella De Vita, Achim Denig, Patrick deNiverville, Abhay Deshpande, Ranjan Dharmapalan, Bogdan Dobrescu, Sergey Donskov, Raphael Dupre, Juan Estrada, Stuart Fegan, Torben Ferber, Clive Field, Enectali Figueroa-Feliciano, Alessandra Filippi, Bartosz Fornal, Arne Freyberger, Alexander Friedland, Iftach Galon, Susan Gardner, Francois-Xavier Girod, Sergei Gninenko, Andrey Golutvin, Stefania Gori, Christoph Grab, Enrico Graziani, Keith Griffioen, Andrew Haas, Keisuke Harigaya, Christopher Hearty, Scott Hertel, JoAnne Hewett, Andrew Hime, David Hitlin, Yonit Hochberg, Roy J. Holt, Maurik Holtrop, Eric W. Hoppe, Todd W. Hossbach, Lauren Hsu, Phil Ilten, Joe Incandela, Gianluca Inguglia, Kent Irwin, Igal Jaegle, Robert P. Johnson, Yonatan Kahn, Grzegorz Kalicy, Zhong-Bo Kang, Vardan Khachatryan,

Venelin Kozhuharov, N. V. Krasnikov, Valery Kubarovsky, Eric Kuflik, Noah Kurinsky, Ranjan Laha, Gaia Lanfranchi, Dale Li, Tongyan Lin, Mariangela Lisanti, Kun Liu, Ming Liu, Ben Loer, Dinesh Loomba, Valery E. Lyubovitskij, Aaron Manalaysay, Giuseppe Mandaglio, Jeremiah Mans, W. J. Marciano, Thomas Markiewicz, Luca Marsicano, Takashi Maruyama, Victor A. Matveev, David McKeen, Bryan McKinnon, Dan McKinsey, Harald Merkel, Jeremy Mock, Maria Elena Monzani, Omar Moreno, Corina Nantais, Sebouh Paul, Michael Peskin, Vladimir Poliakov, Antonio D Polosa, Maxim Pospelov, Igor Rachek, Balint Radics, Mauro Raggi, Nunzio Randazzo, Blair Ratcliff, Alessandro Rizzo, Thomas Rizzo, Alan Robinson, Andre Rubbia, David Rubin, Dylan Rueter, Tarek Saab, Elena Santopinto, Richard Schnee, Jessie Shelton, Gabriele Simi, Ani Simonyan, Valeria Sipala, Oren Slone, Elton Smith, Daniel Snowden-Ifft, Matthew Solt, Peter Sorensen, Yotam Soreq, Stefania Spagnolo, James Spencer, Stepan Stepanyan, Jan Strube, Michael Sullivan, Arun S. Tadepalli, Tim Tait, Mauro Taiuti, Philip Tanedo, Rex Tayloe, Jesse Thaler, Nhan V. Tran, Sean Tulin, Christopher G. Tully, Sho Uemura, Maurizio Ungaro, Paolo Valente, Holly Vance, Jerry Vavra, Tomer Volansky, Belina von Krosigk, Andrew Whitbeck, Mike Williams, Peter Wittich, Bogdan Wojtsekhowski, Wei Xue, Jong Min Yoon, Hai-Bo Yu, Jaehoon Yu, Tien-Tien Yu, Yue Zhang, Yue Zhao, Yiming Zhong, and Kathryn Zurek. Dark sectors 2016 workshop: Community report, 2016.

[34] Marc Schumann. Direct detection of WIMP dark matter: concepts and status. *Journal of Physics G: Nuclear and Particle Physics*, 46(10):103003, aug 2019.

[35] Q. Arnaud et al. First results from the NEWS-G direct dark matter search experiment at the LSM. *Astropart. Phys.*, 97:54–62, 2018.

[36] Wei Guo and Daniel N. McKinsey. Concept for a dark matter detector using liquid helium-4. *Phys. Rev.*, D87(11):115001, 2013.

[37] Yu-Sheng Liu, David McKeen, and Gerald A. Miller. Electrophobic Scalar Boson and Muonic Puzzles. *Phys. Rev. Lett.*, 117(10):101801, 2016.

[38] S. A. Hertel, A. Biekert, J. Lin, V. Velan, and D. N. McKinsey. A Path to the Direct Detection of sub-GeV Dark Matter Using Calorimetric Readout of a Superfluid ^{4}He Target. 2018.

[39] Noah Alexander Kurinsky, To Chin Yu, Yonit Hochberg, and Blas Cabrera. Diamond Detectors for Direct Detection of Sub-GeV Dark Matter. *Phys. Rev.*, D99(12):123005, 2019.

[40] Helmut Schober. An introduction to the theory of nuclear neutron scattering in condensed matter. *Journal of Neutron Research*, 17:109–357, 2014.

[41] G. L. Squires. *Introduction to the Theory of Thermal Neutron Scattering*. Dover Publications, Inc., Mineola, New York, 1996.

[42] Brian Campbell-Deem, Peter Cox, Simon Knapen, Tongyan Lin, and Tom Melia. Multi-phonon excitations from dark matter scattering in crystals. *Phys. Rev. D*, 101(3):036006, 2020. [Erratum: Phys.Rev.D 102, 019904 (2020)].

[43] A Togo and I Tanaka. First principles phonon calculations in materials science. *Scr. Mater.*, 108:1–5, Nov 2015.

[44] Sinead Griffin, Simon Knapen, Tongyan Lin, and Kathryn M. Zurek. Directional Detection of Light Dark Matter with Polar Materials. *Phys. Rev.*, D98(11):115034, 2018.

[45] Sinead M. Griffin, Katherine Inzani, Tanner Trickle, Zhengkang Zhang, and Kathryn M. Zurek. Multi-Channel Direct Detection of Light Dark Matter: Target Comparison. 2019.

[46] Ahmet Coskuner, Tanner Trickle, Zhengkang Zhang, and Kathryn M. Zurek. Directional detectability of dark matter with single phonon excitations: Target comparison. *Phys. Rev. D*, 105(1):015010, 2022.

[47] Peter Cox, Tom Melia, and Surjeet Rajendran. Dark matter phonon coupling. *Phys. Rev.*, D100(5):055011, 2019.

[48] Simon Knapen, Tongyan Lin, Matt Pyle, and Kathryn M. Zurek. Detection of Light Dark Matter With Optical Phonons in Polar Materials. *Phys. Lett.*, B785:386–390, 2018.

[49] Tanner Trickle, Zhengkang Zhang, Kathryn M. Zurek, Katherine Inzani, and Sinead Griffin. Multi-Channel Direct Detection of Light Dark Matter: Theoretical Framework. 2019.

[50] Katelin Schutz and Kathryn M. Zurek. Detectability of Light Dark Matter with Superfluid Helium. *Phys. Rev. Lett.*, 117(12):121302, 2016.

[51] Simon Knapen, Tongyan Lin, and Kathryn M. Zurek. Light Dark Matter in Superfluid Helium: Detection with Multi-excitation Production. *Phys. Rev.*, D95(5):056019, 2017.

[52] Francesca Acanfora, Angelo Esposito, and Antonio D. Polosa. Sub-GeV Dark Matter in Superfluid He-4: an Effective Theory Approach. *Eur. Phys. J.*, C79(7):549, 2019.

[53] Andrea Caputo, Angelo Esposito, and Antonio D. Polosa. Sub-MeV Dark Matter and the Goldstone Modes of Superfluid Helium. *Phys. Rev.*, D100(11):116007, 2019.

[54] S Tamura. Anomalously long lifetimes of high-energy surface acoustic phonons. *Phys. Rev. B*, 30:610–617, Jul 1984.

[55] S Tamura. Spontaneous decay rates of la phonons in quasi-isotropic solids. *Phys. Rev. B*, 31:2574–2577, Feb 1985.

[56] Yonit Hochberg, Matt Pyle, Yue Zhao, and Kathryn M. Zurek. Detecting Superlight Dark Matter with Fermi-Degenerate Materials. *JHEP*, 08:057, 2016.

[57] Daniel Green and Surjeet Rajendran. The Cosmology of Sub-MeV Dark Matter. *JHEP*, 10:013, 2017.

[58] Simon Knapen, Tongyan Lin, and Kathryn M. Zurek. Light Dark Matter: Models and Constraints. *Phys. Rev.*, D96(11):115021, 2017.

[59] Sacha Davidson, Steen Hannestad, and Georg Raffelt. Updated bounds on millicharged particles. *JHEP*, 05:003, 2000.

[60] Hendrik Vogel and Javier Redondo. Dark Radiation constraints on minicharged particles in models with a hidden photon. *JCAP*, 1402:029, 2014.

[61] G. P. Srivastava. Phonon conductivity of insulators and semiconductors. *J. Phys. Chem. Solids*, 41:357–368, 1980.

[62] B. K. Ridley and Rita Gupta. Nonelectronic scattering of longitudinal-optical phonons in bulk polar semiconductors. *Phys. Rev. B*, 43:4939–4944, Feb 1991.

[63] Saswati Barman and G. P. Srivastava. Long-wavelength nonequilibrium optical phonon dynamics in cubic and hexagonal semiconductors. *Phys. Rev. B*, 69:235208, Jun 2004.

[64] Haruki Watanabe and Hitoshi Murayama. Redundancies in Nambu-Goldstone Bosons. *Phys. Rev. Lett.*, 110(18):181601, 2013.

[65] Angelo Esposito. *Private Communication*. 2019.

[66] Ansgar Denner, S. Dittmaier, M. Roth, and D. Wackeroth. Predictions for all processes e+ e- —¿ 4 fermions + gamma. *Nucl. Phys.*, B560:33–65, 1999.

[67] Jacob Lubliner. *Plasticity Theory*. Dover Books on Engineering, 2006.

[68] Michał Łopuszyński and Jacek A. Majewski. Ab initio calculations of third-order elastic constants and related properties for selected semiconductors. *Phys. Rev. B*, 76:045202, Jul 2007.

[69] James A. Bains Jr and M A. Breazeale. Third-order elastic constants of germanium between 300 and 3°k. *Phys. Rev. B*, 13:3623–3630, 04 1976.

[70] A.V. Telichko, S.V. Erohin, and G.M. et al. Kvashnin. Ab initio calculations of third-order elastic constants and related properties for selected semiconductors. *J. Mater. Sci.*, 52, 2017.

[71] J. Sorgel and U. Scherz. Ab initio calculation of elastic constants and electronic properties of znse and znte under uniaxial strain. *Eur. Phys. J. B*, 5:45–52, 09 1998.

[72] Chenju Wang, Jianbing Gu, Xiaoyu Kuang, and Shikai Xiang. Equation of state, nonlinear elastic response, and anharmonic properties of diamond-cubic silicon and germanium: First-principles investigation. *Z. Naturforsch. A*, 70:403–412, 01 2015.

[73] Yonatan Kahn, Gordan Krnjaic, and Bashi Mandava. Dark Matter Detection with Bound Nuclear Targets: The Poisson Phonon Tail. *Phys. Rev. Lett.*, 127(8):081804, 2021.

[74] Simon Knapen, Jonathan Kozaczuk, and Tongyan Lin. Migdal Effect in Semiconductors. *Phys. Rev. Lett.*, 127(8):081805, 2021.

[75] Kim V. Berghaus, Rouven Essig, Yonit Hochberg, Yutaro Shoji, and Mukul Sholapurkar. The Phonon Background from Gamma Rays in Sub-GeV Dark Matter Detectors. 12 2021.

[76] Simon Knapen, Jonathan Kozaczuk, and Tongyan Lin. DarkELF: A python package for dark matter scattering in dielectric targets. *Phys. Rev. D*, 105(1):015014, 2022.

[77] G. Placzek, B. R. A. Nijboer, and L. Van Hove. Effect of short wavelength interference on neuteron scattering by dense systems of heavy nuclei. *Phys. Rev.*, 82:392–403, May 1951.

[78] Sinéad M. Griffin, Yonit Hochberg, Katherine Inzani, Noah Kurinsky, Tongyan Lin, and To Chin Yu. Silicon carbide detectors for sub-GeV dark matter. *Phys. Rev. D*, 103(7):075002, 2021.

[79] G. Kresse and J. Furthmüller. Efficient iterative schemes for ab initio total-energy calculations using a plane-wave basis set. *Phys. Rev. B*, 54:11169–11186, Oct 1996.

[80] Tanner Trickle, Zhengkang Zhang, and Kathryn M. Zurek. Effective field theory of dark matter direct detection with collective excitations. *Phys. Rev. D*, 105(1):015001, 2022.

[81] Rouven Essig, Marivi Fernandez-Serra, Jeremy Mardon, Adrian Soto, Tomer Volansky, and Tien-Tien Yu. Direct Detection of sub-GeV Dark Matter with Semiconductor Targets. *JHEP*, 05:046, 2016.

[82] G.P. Srivastava. Phonon conductivity of insulators and semiconductors. *Journal of Physics and Chemistry of Solids*, 41(4):357–368, 1980.